

A NEW UNRESOLVED RESONANCE REGION METHODOLOGY

A Dissertation
Presented to
The Academic Faculty

by

Andrew Michael Holcomb

In Partial Fulfillment
of the Requirements for the Degree
Doctor of Philosophy in Nuclear and Radiological Engineering

George W. Woodruff School of Mechanical Engineering
Georgia Institute of Technology
December 2015

Copyright © 2015 by Andrew M. Holcomb

A NEW UNRESOLVED RESONANCE REGION METHODOLOGY

Approved by:

Dr. Farzad Rahnema, Advisor
George W. Woodruff School
Georgia Institute of Technology

Dr. Bojan Petrovic
George W. Woodruff School
Georgia Institute of Technology

Dr. Tom Morley
School of Mathematics
Georgia Institute of Technology

Dr. Luiz Leal
Institut de Radioprotection et de Sûreté
Nucléaire (IRSN)

Dr. Dingkang Zhang
George W. Woodruff School
Georgia Institute of Technology

Date Approved: November 6, 2015

ACKNOWLEDGEMENTS

This work was supported by the US/DOE Nuclear Criticality Safety Program. Any opinions, findings, conclusions, or recommendations expressed in this publication are those of the author and do not necessarily reflect the views of the Department of Energy Office of Nuclear Energy.

First, I would like to thank my advisor, Dr. Farzad Rahnema, for giving me the opportunity to work and study at Georgia Tech. While at Georgia Tech, I have learned volumes from him about the many aspects of nuclear engineering. His leadership created an environment where I was able to successfully learn from the very best and brightest in many disciplines.

Next, I would like to thank Dr. Luiz Leal for giving me a chance, and allowing me to work with him at Oak Ridge National Laboratory. His friendliness, patience, encouragement, wisdom, and guidance have made me a better engineer and person. I am truly grateful for everything he has done for me, and I don't think I could have ever accomplished this task without him.

I would also like to thank the rest of my committee, Dr. Bojan Petrovic, Dr. Dingkang Zhang, and Dr. Tom Morley, for critiquing my work, and for teaching me a great deal through their own excellent courses. I hope that they all continue to enlighten students' minds for many years to come.

Of course, I would be remiss if I did not thank my fellow Computational Reactor and Medical Physics Laboratory members. My thanks extends to Kevin Connolly and Saam Yasseri for their expertise and engaging conversation. A special thanks goes out to my friends Chris Chapman, Ryan Hon, Alex Huning, Gabe Kooreman, Daniel Lago, and Kyle Remley, who all made graduate school more bearable and conference trips much more interesting!

Next, I would like to thank my family for all of their encouragement and support over the many years of my studies. Even when I doubted myself, their belief never wavered. I lack the words to express how truly proud I am to be a part of my family, and I only hope that I can continue to make them proud of me.

Lastly, I would like to thank my fiancée, Marissa. Her endless, unconditional love, caring, and understanding have helped keep me grounded and sane. Through the highs and the lows, she has always been able to raise my spirits. She is a truly beautiful person, inside and out. If there is anything I am looking forward to more than finishing this degree, it is marrying her.

TABLE OF CONTENTS

	Page
ACKNOWLEDGEMENTS	iv
LIST OF TABLES	viii
LIST OF FIGURES	ix
SUMMARY	xii
<u>CHAPTER</u>	
1 Introduction	1
2 Background	3
Relating the Schrödinger Equation to the R-Matrix	4
R-Matrix Formalism	8
Doppler Broadening	13
PURM Method	17
3 New URR Method	24
Generating the Resonance-Pair Sequence	24
Cross-Section Reconstruction	28
Doppler Broadening Treatment	35
Probability Table Construction	44
4 Results	47
Resolved Resonance Region	47
²³⁸ U Unresolved Resonance Region Probability Tables	78
Benchmarks	91
5 Conclusions and Future Work	115
APPENDIX A: ¹⁶ O ENDF/B-VII.1 Resolved FILE2 LRF=7 Data	116

APPENDIX B:	^{19}F ENDF/B-VII.1 Resolved FILE2 LRF=7 Data	118
APPENDIX C:	^{35}Cl ENDF/B-VII.1 Resolved FILE2 LRF=7 Data	121
APPENDIX D:	^{238}U ENDF/B-VII.1 Unresolved FILE2 LRF=1 Data	126
APPENDIX E:	^{238}U Probability Tables at 293.6 K	128
REFERENCES		138
VITA		141

LIST OF TABLES

	Page
Table 1: Material composition of the U-metal in the BIG TEN benchmark	96
Table 2: Regional dimensions and composition of the BIG TEN benchmark.	98
Table 3: k_{eff} results for the IEU-MET-FAST-007 benchmark using the stock MCNP continuous-energy ENDF/BVII.0 libraries, ^{238}U modified ENDF/BVII.0 libraries, ENDF/BVII.0 libraries, and ^{238}U modified ENDF/BVII.0 libraries.	100
Table 4: Regional dimensions of the IEU-MET-FAST-003 benchmark.	105
Table 5: Material definitions of the IEU-MET-FAST-003 benchmark.	106
Table 6: k_{eff} results for the IEU-MET-FAST-003 benchmark using the stock MCNP continuous-energy ENDF/BVII.1 libraries and the ^{238}U modified library.	107
Table 7: Regional dimensions and material names of the IEU-COMP-FAST-004 benchmark.	111
Table 8: Material definitions of the IEU-COMP-FAST-004 benchmark.	112
Table 9: k_{eff} results for the IEU-COMP-FAST-004 benchmark using the stock MCNP continuous-energy ENDF/BVII.1 libraries and the ^{238}U modified library.	114

LIST OF FIGURES

	Page
Figure 1: Flowchart depicting the PURM reconstruction procedure.	23
Figure 2: Best-case scenario for LH temperature broadening routine.	38
Figure 3: Graph showing 0K total cross section in worst-case scenario for LH temperature-broadening routine.	39
Figure 4: Graph showing impact of grid choice in worst-case scenario for LH temperature-broadening routine near the energy of reference.	40
Figure 5: Graph emphasizing the minimal impact the edge-error has on the temperature-broadened cross section near the energy of reference.	41
Figure 6: ^{16}O total neutron cross section.	49
Figure 7: ^{16}O neutron capture cross section.	50
Figure 8: ^{16}O neutron elastic scattering cross section.	51
Figure 9: ^{16}O (n, α) cross section.	52
Figure 10: ^{16}O double-differential elastic-scattering cross section.	53
Figure 11: ^{16}O double-differential (n, α) cross section.	54
Figure 12: ^{19}F total neutron cross section.	55
Figure 13: ^{19}F neutron capture cross section.	56
Figure 14: ^{19}F neutron elastic scattering cross section.	57
Figure 15: ^{19}F first inelastic scattering cross section.	58
Figure 16: ^{19}F second inelastic scattering cross section.	59
Figure 17: ^{19}F double-differential elastic-scattering cross section.	60
Figure 18: ^{19}F double-differential first inelastic-scattering cross section.	61
Figure 19: ^{19}F double-differential second inelastic-scattering cross section.	62
Figure 20: ^{35}Cl total neutron cross section.	63
Figure 21: ^{35}Cl neutron capture cross section.	64

Figure 22: ^{35}Cl neutron elastic scattering cross section.	65
Figure 23: ^{35}Cl (n, p) cross section.	66
Figure 24: ^{35}Cl double-differential (n, p) cross section.	67
Figure 25: ^{56}Fe total neutron cross section.	68
Figure 26: ^{56}Fe neutron capture cross section.	69
Figure 27: ^{56}Fe neutron elastic scattering cross section.	70
Figure 28: ^{56}Fe neutron inelastic scattering cross section.	71
Figure 29: ^{63}Cu total neutron cross section.	72
Figure 30: ^{63}Cu neutron capture cross section.	73
Figure 31: ^{63}Cu neutron elastic scattering cross section.	74
Figure 32: ^{65}Cu total neutron cross section.	75
Figure 33: ^{65}Cu neutron capture cross section.	76
Figure 34: ^{65}Cu neutron elastic scattering cross section.	77
Figure 35: Plot of the normalized total cross-section factors generated by both methods at 30 keV.	79
Figure 36: Plot of the normalized capture cross-section factors generated by both methods at 30 keV.	80
Figure 37: Plot of the normalized elastic cross-section factors generated by both methods at 30 keV.	81
Figure 38: Plot of the normalized total cross-section factors generated by both methods at 50 keV.	82
Figure 39: Plot of the normalized capture cross-section factors generated by both methods at 50 keV.	83
Figure 40: Plot of the normalized elastic cross-section factors generated by both methods at 50 keV.	84
Figure 41: Plot of the normalized inelastic cross-section factors generated by both methods at 50 keV.	85
Figure 42: Plot of the normalized total cross-section factors generated by both methods at 140 keV.	86

Figure 43: Plot of the normalized capture cross-section factors generated by both methods at 140 keV.	87
Figure 44: Plot of the normalized elastic cross-section factors generated by both methods at 140 keV.	88
Figure 45: Plot of the normalized inelastic cross-section factors generated by both methods at 140 keV.	89
Figure 46: k_{eff} sensitivity coefficients for the selected benchmark problems.	92
Figure 47: XZ-view through the center of the BIG TEN benchmark configuration.	94
Figure 48: XY-view through the center of the BIG TEN benchmark configuration.	95
Figure 49: XZ-view through the center of the BIG TEN benchmark configuration with labeled regions.	97
Figure 50: Normalized flux spectrum in the central IEU core.	102
Figure 51: Plane-view through the center of the IEU-MET-FAST-003 benchmark configuration.	104
Figure 52: XZ-view through the center of the IEU-COMP-FAST-004 benchmark configuration.	109
Figure 53: XY-view through the center of the IEU-COMP-FAST-004 benchmark configuration.	110

SUMMARY

In this dissertation, a new method for constructing probability tables in the Unresolved Resonance Region (URR) is presented. This new methodology is an extensive modification of the Single-Level Breit-Wigner (SLBW) resonance-pair sequence method commonly used to generate probability tables in the URR. Using a Monte Carlo process, many resonance-pair sequences are generated by sampling the average resonance parameter data for the unresolved resonance region from the ENDF data file. The resonance parameters are then converted to the Reich-Moore (RM) formalism to take advantage of the more robust R-Matrix Limited (RML) format. For each sampled set of resonance-pair sequences, the temperature-dependent cross sections are calculated on a small grid around the energy of reference using the RM formalism and the Leal-Hwang (LH) Doppler broadening methodology. The effective cross sections calculated at the energy of reference are then used to construct probability tables in the unresolved resonance region. The tables are then normalized to calculate the energy-dependent cross-section factors for the various reaction types.

The new URR probability table method reconstructs the cross section in a way that is consistent with the methodology used in the Resolved Resonance Region (RRR). By using the RM formalism, all the appropriate interference terms are captured in the cross section reconstruction, leading to a more physically accurate representation of the energy self-shielding effect. Further, the RML format removes any restriction on reaction type, allowing for any number and type of incoming and exiting channels to be treated explicitly. The new URR reconstruction method provides a physically accurate and

consistent way to capture the energy self-shielding effect through the cross-section factors calculated in the probability tables.

The RML algorithm is implemented in C++ in the AMPX code package. This implementation was then tested in the RRR by performing cross section reconstructions for many different isotopes, including ^{16}O , ^{19}F , ^{35}Cl , ^{56}Fe , ^{63}Cu , and ^{65}Cu . This RML implementation was then used in conjunction with a resonance-pair sequence generator to reconstruct the URR probability tables for ^{238}U . The modified probability tables were then introduced into the MCNP ENDF/B-VII.0 and ENDF/B-VII.1 continuous-energy neutron libraries. These libraries were then tested using a set of International Criticality Safety Benchmark Evaluation Project (ICSBEP) benchmarks that are known to be sensitive to perturbations in the ^{238}U cross section, including the IEU-COMP-FAST-004, IEU-MET-FAST-003, and IEU-MET-FAST-007 (Big Ten) benchmark problems.

CHAPTER 1

INTRODUCTION

Physically precise representation of neutron cross sections is vital to the accurate calculation of the cross-section resonance self-shielding effects, improving model fidelity. In the resolved resonance energy region (RRR), several approximations to the full R-Matrix formalism are known to accurately reconstruct the cross sections directly from a set of evaluated resonance parameters. In contrast to the RRR, in the unresolved resonance region (URR) the cross sections have historically been reconstructed from a set of statistical averages and a Single-Level Breit-Wigner (SLBW) approximation that is the least accurate among the various approximations to the R-Matrix formalism. While the underlying Monte Carlo routine used in the URR to generate probability tables is sound, the structure of the probability table is affected by the choice of the cross-section representation.

The purpose of this dissertation is to present an URR methodology that is more consistent with the approach used in the RRR. In contrast to the SLWB approximation used in many URR processing codes, a modern implementation of the most general approximation to the full R-Matrix theory, the R-Matrix Limited (RML) formalism, was expanded in the cross-section processing code AMPX [1] for use in the URR. The Reich-Moore (RM) approximation in the RML format is used in conjunction with a statistical pseudo-resonance pair series generator to reconstruct the neutron cross sections in the URR. The reconstructed cross sections are Doppler broadened using the Leal-Hwang (LH) method [2], and then used to generate probability tables in the URR. The theoretical background for the R-Matrix theory and the probability table method is presented in Chapter 2. The new URR method is presented in Chapter 3. The RML algorithm and new

URR method are validated and benchmarked in Chapter 4. Finally, conclusions and future work are given in Chapter 5.

CHAPTER 2

BACKGROUND

For completeness, this section presents a brief derivation of scattering theory as it relates to R-Matrix theory. The more industrious and interested reader is encouraged to read the Lane and Thomas article on the subject [3]. The derivation presented here is similar to the presentation given in the SAMMY manual, which is based on publications by Fröhner and Foderaro [4 - 6]. For the general derivation, the reader is again encouraged to review the Lane and Thomas publication. The derivation presented here is only valid in the case of spinless projectiles and targets, and only considers elastic scattering. Still, in light of the research presented here (neutron projectiles impinging on ^{238}U nuclei), the derivation is relevant and worthwhile.

In principle, one can directly calculate the neutron cross section from the wave functions of the nuclear system in question, provided the incoming and outgoing wave functions are well known. Unfortunately, in practice this is not possible; it is possible to know the incoming wave functions very well, but the reaction generally changes the outgoing wave functions in an unpredictable way. The driving force behind the R-Matrix theory is to circumvent this dilemma by instead using the wave function of the system when the two particles become close enough to form a compound nucleus. Even though the resulting wave function is complicated, it can be expanded in terms of its associated eigenstates. This internal wave function can then be matched to the incoming and outgoing wave functions in order to describe the cross section. The matching is performed through the properties of the eigenstates of the compound nucleus, namely through things such as the eigenvalues (energies), spin, parity, and reaction widths.

The real beauty of the R-Matrix formulation is that it only requires knowledge of the properties of the nuclear excitation levels, and does not require explicit knowledge of

physics of the underlying interaction between the neutron and the nucleus. The nucleus is treated as a black box, so that only the aforementioned eigenstate properties need to be prescribed in order to define the cross section. So, while we are unable to glean information about the forces inside the nucleus from this method, the information is not needed for our formalism.

Relating the Schrödinger Equation to the R-Matrix

As previously mentioned, the derivation presented here is only valid for spinless projectiles and targets (e.g., neutrons and ^{238}U) assuming only elastic scattering and absorption. For a real potential, the Schrödinger equation can be written as

$$\left(\frac{-\hbar^2}{2m}\nabla^2 + V\right)\Psi = E\Psi. \quad (1)$$

It is worth noting that if we allow V to be complex, then the real part of the potential causes scattering and the imaginary part of the potential would correspond to absorption.

We can then expand the wave function in partial waves as

$$\Psi(r, \cos \theta) = \sum_{l=0}^{\infty} \frac{\varphi_l(r)}{r} P_l(\cos \theta). \quad (2)$$

In the radial domain, each of the partial waves then obeys the equation

$$\left\{\frac{d^2}{dr^2} + \frac{2m}{\hbar^2}\left[E - V(r) - \frac{l(l+1)\hbar^2}{2mr^2}\right]\right\}\varphi_l(E, r) = 0. \quad (3)$$

These partial waves can be expressed in terms of their eigenfunctions by

$$\varphi_l(E, r) = \sum_{\lambda} A_{l\lambda} \varphi_l(E_{\lambda}, r). \quad (4)$$

These eigenfunctions must also obey Eq. (3), that is

$$\left\{ \frac{d^2}{dr^2} + \frac{2m}{\hbar^2} \left[E_{\lambda} - V(r) - \frac{l(l+1)\hbar^2}{2mr^2} \right] \right\} \varphi_l(E_{\lambda}, r) = 0. \quad (5)$$

We require the eigenfunctions to be finite, and thus require that

$$\varphi_l(E_{\lambda}, r = 0) = 0, \quad (6)$$

and

$$\left. \frac{d\varphi_l(E_{\lambda}, r)}{dr} \right|_{r=a} = \frac{B_l \varphi_l(E_{\lambda}, a)}{a}, \quad (7)$$

where B_l is real and a represents the position of the nuclear surface.

The eigenfunctions form a basis set, and can be normalized such that

$$\int_0^a \varphi_l(E_{\lambda}, r) \varphi_l(E_{\lambda'}, r) dr = \delta_{\lambda\lambda'}, \quad (8)$$

where $\delta_{\lambda\lambda'}$ is the Kronecker delta function.

Using this property of our basis set, we can express the expansion coefficients $A_{l\lambda}$ as

$$A_{l\lambda} = \int_0^a \varphi_l(E_\lambda, r) \varphi_l(E, r) dr. \quad (9)$$

We now eliminate the potential, $V(r)$. Multiplying Eq. (5) by the eigenfunction $\varphi_l(E_\lambda, r)$ and multiplying Eq. (3) by the partial wave $\varphi_l(E, r)$ and subtracting, we obtain

$$\varphi_l(E, r) \frac{d^2 \varphi_l(E_\lambda, r)}{dr^2} - \varphi_l(E_\lambda, r) \frac{d^2 \varphi_l(E, r)}{dr^2} + \frac{2m}{\hbar^2} (E_\lambda - E) \varphi_l(E, r) \varphi_l(E_\lambda, r) = 0. \quad (10)$$

Integrating Eq. (10) from 0 to a and applying integration by parts yields

$$\begin{aligned} & \left[\varphi_l(E, r) \frac{d\varphi_l(E_\lambda, r)}{dr} \right]_{r=a} - \int_0^a \frac{d\varphi_l(E, r)}{dr} \frac{d\varphi_l(E_\lambda, r)}{dr} dr - \left[\varphi_l(E_\lambda, r) \frac{d\varphi_l(E, r)}{dr} \right]_{r=a} \\ & + \int_0^a \frac{d\varphi_l(E, r)}{dr} \frac{d\varphi_l(E_\lambda, r)}{dr} dr + \frac{2m}{\hbar^2} (E_\lambda - E) \int_0^a \varphi_l(E_\lambda, r) \varphi_l(E, r) dr = 0. \end{aligned} \quad (11)$$

The last integral in Eq. (11) is the definition of the expansion coefficient $A_{l\lambda}$, so that

$$A_{l\lambda} = \frac{\hbar^2}{2m} (E_\lambda - E)^{-1} \left\{ \left[\varphi_l(E_\lambda, r) \frac{d\varphi_l(E, r)}{dr} \right]_{r=a} - \left[\varphi_l(E, r) \frac{d\varphi_l(E_\lambda, r)}{dr} \right]_{r=a} \right\}. \quad (12)$$

Applying our boundary conditions allows us express the partial waves at $r = a$ as

$$\varphi_l(E, a) = \frac{\hbar^2}{2ma} \sum_\lambda \left[\frac{\varphi_l(E_\lambda, a) \varphi_l(E_\lambda, a)}{E_\lambda - E} \right] \left[r \frac{d\varphi_l(E, r)}{dr} - B_l \varphi_l(E, r) \right]_{r=a}. \quad (13)$$

From Eq. (13) we can directly extract the R-Matrix, given by

$$R_l = \frac{\hbar^2}{2ma} \sum_{\lambda} \left[\frac{\varphi_l(E_{\lambda}, a) \varphi_l(E_{\lambda}, a)}{E_{\lambda} - E} \right]. \quad (14)$$

The R-Matrix is more commonly written as

$$R_l = \sum_{\lambda} \frac{\gamma_{\lambda} \gamma_{\lambda}}{E_{\lambda} - E}, \quad (15)$$

where γ_{λ} is given by

$$\gamma_{\lambda} = \sqrt{\frac{\hbar^2}{2ma}} \varphi_l(E_{\lambda}, a). \quad (16)$$

At this point, we can identify properties that are directly related to the nuclear data. A resonance at level λ is located at E_{λ} and has reduced-width amplitudes of γ_{λ} . These parameters are useful since they can be evaluated by fitting to cross-section measurements.

R-Matrix Formalism

The R-Matrix theory is the main methodology used to describe the nuclear reaction cross sections in the resolved resonance region. The R-Matrix theory is derived from the Schrodinger equation, treating the complicated nuclear potential inside the nucleus as a black box. The derivation of the R-Matrix is long, arduous, and well documented in several texts, including the “Handbook of Nuclear Engineering” [7]. Hence, only the final results of the derivation are presented here.

R-matrix theory is most easily expressed in terms of channels, where we have defined a channel to include a complete description of the particle pair (both incoming and outgoing) as well as the other information pertaining to interaction between the two particles. In accordance with the SAMMY notation, a channel is completely defined as $c = (\alpha, l, s, J)$, where α defines the particle-pair for the channel (including masses, charges, spins, parities, Q-value, etc.), l is associated with the angular momentum and its associated parity of the particle pair defined by α , s represents the channel spin (sum of the incoming particle spin and the target spin, and J is the total angular momentum (sum of the angular momentum and the channel spin).

With the definitions above, we can define the angle-integrated cross section for a reaction from entrance channel c to exit channel c' with total angular momentum J as:

$$\sigma_{cc'} = \frac{\pi}{k_a^2} g_{J\alpha} |e^{2iw_c} \delta_{cc'} - U_{cc'}|^2 \delta_{JJ'} \quad (17)$$

where k_α is the wave number in the center-of-mass system of the incident particle pair α , $g_{J\alpha}$ is the spin statistical factor, and w_c is the Coulomb phase-shift difference, and $U_{cc'}$ is the collision matrix connecting the incoming and outgoing channels.

The spin-statistical factor is defined as:

$$g_{J\alpha} = \frac{2J + 1}{(2i_p + 1)(2I + 1)}, \quad (18)$$

where i_p and I are the intrinsic spins of the projectile and target, respectively.

The wave number is given by:

$$(\hbar k_\alpha)^2 = \frac{2mM^2}{(m + M)^2} E, \quad (19)$$

where m and M are the masses of the projectile and target, respectively, and E is the laboratory kinetic energy of the projectile.

From the cross section equation, we now identify the collision matrix U , whose elements are given by:

$$U_{cc'} = \Omega_c W_{cc'} \Omega_{c'}. \quad (20)$$

The matrix W , contains the elusive R-Matrix, and may be written as:

$$W = P^{\frac{1}{2}}(I - RL)^{-1}(I - RL^*)P^{\frac{-1}{2}}. \quad (21)$$

The R-Matrix is defined as:

$$R_{cc'} = \sum_{\lambda} \frac{\gamma_{\lambda c} \gamma_{\lambda c'}}{E_{\lambda} - E} \delta_{JJ'}, \quad (22)$$

where λ refers to a particular resonance, E_{λ} is the energy of that resonance, and $\gamma_{\lambda c}$ is the reduced width amplitude, given by:

$$\Gamma_{\lambda c} = 2P_c \gamma_{\lambda c}^2, \quad (23)$$

where $\Gamma_{\lambda c}$ is the channel width of that resonance and P_c is the energy dependent penetrability for that channel. The definition of the R-Matrix given above provides insight into why this formulation is much more powerful than the SLBW formulae. The SLBW formalism is a crude approximation made to the R-Matrix in which all interference effects, including level-level interference and channel-channel interference are ignored. Both types of interference effects are captured in the R-Matrix formulation since the formalism is rigorous. The channel-channel interference effects are immediately obvious, as can be seen by the appearance of the reduced width amplitudes in the numerator of the summation. While the level-level interference effects are not so easily seen, they are captured since varying the resonance parameters of one particular resonance can interfere with the cross section shape locally and globally, possibly changing the shape of the cross section near another resonance.

As we have seen, the R-matrix defines the collision matrix, the potential scattering phase shifts (accounted for in Ω), the penetrability P , and L , a matrix defined in terms of the penetrability, shift factor, and arbitrary boundary constant at the channel radius. However, in practice, the presented formulation is computationally unstable. A more computationally stable formulation consists of substituting another matrix, X , for

the matrix W such that

$$W = I + 2iX. \quad (24)$$

Making the appropriate substitution, we find that X is given by

$$X = P^{\frac{1}{2}}L^{-1}(L^{-1} - R)^{-1}RP^{\frac{1}{2}}. \quad (25)$$

More explicitly, the elements of X are given by

$$X_{cc'} = P_c^{\frac{1}{2}}L_c^{-1} \sum_{c''} [(L^{-1} - R)^{-1}]_{cc''} R_{c''c'} P_{c'}^{\frac{1}{2}} \delta_{JJ'}. \quad (26)$$

The elastic scattering cross section is then given by

$$\begin{aligned} \sigma_{\alpha,\alpha} = \frac{4\pi}{k_\alpha^2} \sum_J g_{J\alpha} \sum_c [\sin^2(\varphi_c)(1 - 2\text{Im}(X_{cc})) - \text{Re}(X_{cc}) \sin(2\varphi_c) \\ + \sum_{c'} |X_{cc'}|^2]. \end{aligned} \quad (27)$$

Similarly, the total cross section is given by

$$\begin{aligned} \sigma_{\alpha,\text{total}} = \frac{4\pi}{k_\alpha^2} \sum_J g_{J\alpha} \sum_c \left[\frac{1}{2} \sin^2(\varphi_c) + \text{Im}(X_{cc}) \cos(2\varphi_c) \right. \\ \left. - \text{Re}(X_{cc}) \sin(2\varphi_c) \right]. \end{aligned} \quad (28)$$

Lastly, all other reaction channels from pair α to α' can be written as

$$\begin{aligned} \sigma_{\alpha,\alpha'} = \frac{4\pi}{k_\alpha^2} \sum_J g_{J\alpha} \sum_c [\sin^2(\varphi_c)(1 - 2\text{Im}(X_{cc})) \\ - 2\text{Im}(X_{cc})\sin(2\varphi_c)] \delta_{\alpha\alpha'} + \sum_{c'} |X_{cc'}|^2. \end{aligned} \quad (29)$$

Furthermore, using the same matrices and definitions from above, we can define the angular dependent cross section in the center-of-mass system in terms of the product of Legendre polynomials and their associated collision-matrix dependent coefficients [8]:

$$\frac{d\sigma_{\alpha\alpha'}(E)}{d\Omega_{CM}} = \sum_L B_{L\alpha\alpha'}(E) P_L(\cos\beta) \quad (30)$$

Here, $\alpha\alpha'$ identifies that the reaction is proceeding from particle-pair α to particle-pair α' , P_L is the Legendre polynomial of degree L , β is the angle of the outgoing particle relative to the incident particle in the center-of-mass system. The associated coefficients $B_{L\alpha\alpha'}$ are defined by an expression which is dependent on the collision matrix, the intrinsic spins of the projectile and target under consideration, the wave number associated with particle-pair α , and a geometric factor that is a function of several quantum numbers and the chosen Legendre degree:

$$\begin{aligned} B_{L\alpha\alpha'}(E) = \\ \frac{1}{4k_\alpha^2} \sum_{\substack{j_1, l_1, s_1, l'_1, s'_1 \\ j_2, l_2, s_2, l'_2, s'_2}} \frac{G\{j_1 s_1 l'_1 s'_1 j_1\} \{j_2 s_2 l'_2 s'_2 j_2\} L}{(2i+1)(2I+1)} \text{Re}[(\delta_{c_1 c'_1} - U_{c_1 c'_1}(E))(\delta_{c_2 c'_2} - U_{c_2 c'_2}(E))]. \end{aligned} \quad (31)$$

Doppler Broadening

The thermal motion of bound target nuclei gives rise to Doppler broadening. In practice, the system is above 0 K, and so incoming neutrons will be impeding on target samples whose nuclei exhibit a distribution of velocities. This thermal motion must be accounted for in two critical instances. At low energy, when the neutron speed is comparable to the thermal energy of the system, the target nuclei can no longer be treated as being at rest. The temperature broadening is also very important in the resonance regions, where the cross section can exhibit tall but narrow peaks. In this region the neutron energy is much greater than thermal energy of the target, but the target motion must be accounted for since the cross section often has resonance peaks with widths significantly smaller than the thermal energy. A brief overview of the equations for Doppler broadening and approximations of the target velocity distribution are presented here for completeness. A complete derivation is outside of the scope of this work, and can be found in several texts [9].

Definition of Doppler Broadening

The neutron cross section is a function of the relative speed between the target nucleus and the impending neutron. If we were interested in the neutron cross section as it relates to single target nuclei, this could easily be calculated by determining the relative velocity between the two. However, we are not interested in the cross section of a single target nucleus, but instead seek the cross section as it relates to the interaction rate with targets in a medium. In this medium, there is not a single target velocity, but a distribution of velocities driven by the temperature of the medium. Hence, the thermal motion of the target nuclei will give rise to an effective temperature-dependent cross section, $\sigma_{Doppler}(mv^2/2)$.

The temperature-dependent cross section can be defined as

$$v\sigma_{Doppler}(mv^2/2) \equiv \int d^3V p(\vec{V}) |\vec{v} - \vec{V}| \sigma(m|\vec{v} - \vec{V}|^2/2), \quad (32)$$

where \vec{v} is the velocity of the neutron in the laboratory system, $\sigma(m|\vec{v} - \vec{V}|^2/2)$ is the unbroadened cross section, \vec{V} is the velocity of the target nuclei, and $p(\vec{V})d^3V$ is the fraction of the nuclei with velocities within d^3V about \vec{V} [10]. It should be noted that the above expression allows us to write an averaged cross section that depends only on the neutron speed.

Free Gas Model

The target velocity distribution is often approximated as a monoatomic free gas in three dimensions. This is the well-known Maxwell-Boltzmann distribution [11], which can be written as

$$p(\vec{V})d^3V = (\sqrt{\pi}u)^{-3} e^{-\left(\frac{V}{u}\right)^2} d^3V, \quad (33)$$

where u is given by

$$u^2 = \frac{2kT}{M}, \quad (34)$$

with M representing the target mass and kT is the temperature in energy units.

If we combine the approximation for the target velocity distribution in Eq. (33) with the definition of the Doppler-broadened cross section in Eq. (32), we find that

$$v\sigma_{Doppler}(mv^2/2) = (\sqrt{\pi}u)^{-3} \int d^3V e^{-\left(\frac{V}{u}\right)^2} |\vec{v} - \vec{V}| \sigma(m|\vec{v} - \vec{V}|^2/2). \quad (35)$$

Now, we can change the integration variable from \vec{V} to $\vec{r} = \vec{v} - \vec{V}$, so our equation becomes

$$v\sigma_{Doppler}(mv^2/2) = (\sqrt{\pi}u)^{-3} \int d^3r e^{-\left(\frac{v^2-2vr\cos\theta+r^2}{u^2}\right)} r \sigma(mr^2/2). \quad (36)$$

The Doppler-broadened cross section can then be represented in spherical coordinates as:

$$\begin{aligned} & v\sigma_{Doppler}(mv^2/2) \\ &= (\sqrt{\pi}u)^{-3} \int_0^{2\pi} d\varphi \int_0^\infty r^2 dr \int_0^\pi \sin\theta e^{-\left(\frac{v^2-2vr\cos\theta+r^2}{u^2}\right)} r \sigma(mr^2/2) d\theta. \end{aligned} \quad (37)$$

Making the substitution $\mu = \cos\theta$ and evaluating the outermost integral, we find that

$$v\sigma_{Doppler}(mv^2/2) = \frac{2}{\sqrt{\pi}u^3} \int_0^\infty dr r^3 e^{-\left(\frac{v^2+r^2}{u^2}\right)} \sigma(mr^2/2) \int_{-1}^1 d\mu e^{\left(\frac{2vr\mu}{u^2}\right)}. \quad (38)$$

The innermost integral can be evaluated to yield

$$\sigma_{Doppler}(mv^2/2) = \frac{1}{\sqrt{\pi}v^2 u} \int_0^\infty dr r^2 \sigma(mr^2/2) \left[e^{-\left(\frac{v-r}{u}\right)^2} - e^{-\left(\frac{v+r}{u}\right)^2} \right]. \quad (39)$$

To further simplify the equation, we make the following substitution:

$$\begin{aligned} s(r) &= \sigma(mr^2/2), & r > 0 \\ s(r) &= -\sigma(m(-r)^2/2), & r < 0. \end{aligned} \quad (40)$$

Inserting the substitution for the unbroadened cross section, we find that

$$\sigma_{Doppler}(mv^2/2) = \frac{1}{\sqrt{\pi}v^2} \int_{-\infty}^{\infty} dr r^2 s(r) e^{-\left(\frac{v-r}{u}\right)^2}. \quad (41)$$

We will now apply this form of the approximate Doppler-broadened cross section to a particular case of interest, namely, when the cross section exhibits a $1/v$ behavior.

$1/v$ Cross Section

The $1/v$ form of the cross section is important since, at sufficiently low energies, far beneath the lowest resonance, the cross section is generally assumed to exhibit $1/v$ behavior [12]. In this case, we can write

$$\begin{aligned} s(r) &= \sigma(mr^2/2) = \frac{\sigma_0 v_0}{r}, & r > 0 \\ s(r) &= -\sigma(m(-r)^2/2) = -\frac{\sigma_0 v_0}{-r} = \frac{\sigma_0 v_0}{r}, & r < 0. \end{aligned} \quad (42)$$

Performing the substitution, we find that

$$\sigma_{Doppler}(mv^2/2) = \frac{\sigma_0 v_0}{\sqrt{\pi}v^2} \int_{-\infty}^{\infty} dr r e^{-\left(\frac{v-r}{u}\right)^2} = \frac{\sigma_0 v_0}{v}. \quad (43)$$

This exact result shows that, under the free gas model assumption, the cross section is conserved under Doppler broadening.

PURM Method

This section serves as an overview of the AMPX module PURM [13]. This material is presented here as PURM is the current AMPX module used to construct the probability tables in the URR. A more detailed description of the PURM methodology can be found in the AMPX manual.

Sampling Procedure

PURM reconstructs the URR cross sections on a grid defined by the ENDF evaluation using a Monte Carlo sampling procedure. In contrast to the ladder approach [14], PURM builds the sequence of resonance pairs around an energy of reference for which probability tables are desired. For each history, a set of resonance-pair sequences are created around each energy of reference by sampling from representative distributions, and then the sequence is used to reconstruct the temperature-broadened cross section at the energy of reference. As with the resonance ladder method, the resonance spacing is sampled from a Wigner distribution given by:

$$W(x) = \frac{\pi}{2} x e^{-\frac{\pi x^2}{4}}, \quad (44)$$

where x is the ratio of the sampled level spacing to the average level spacing. The average level spacing is dependent on the orbital angular momentum, l , and the total angular momentum, J , and so there are typically several resonance-pair sequences constructed per history. For example, in the case of ^{238}U , there are five (l, J) pairs provided in the ENDF evaluation, and so five independent resonance-pair sequences are generated for each PURM history, one for each pair.

The first pair of resonances in each (l, J) dependent sequence is determined by first sampling the average level spacing, $\langle D_{l,J} \rangle$, and a random number, $\rho \in [0,1)$. Then, the first resonance is placed at

$$E_{\lambda=1} = E_{ref} + \rho D_{l,J}, \quad (45)$$

and the second resonance in the pair is placed at

$$E_{\lambda=2} = E_{ref} + (\rho - 1)D_{l,J}, \quad (46)$$

where E_{ref} is the energy of reference, and $D_{l,J}$ is the sampled level spacing. The stochastic nature of the resonance placement is captured through the introduction of the random number ρ , which allows the starting point for each sequence to shift about the energy of reference, while maintaining the correct level spacing. The rest of the resonances are then added to the sequence in a similar manner; the level spacing is sampled, and the new resonance is placed at

$$E_{\lambda=n} = \begin{cases} E_{\lambda=n-2} + D_{l,J}, & n \text{ odd} \\ E_{\lambda=n-2} - D_{l,J}, & n \text{ even} \end{cases} \quad (47)$$

Once the locations of the energy levels are determined, the reaction widths are sampled for each resonance in the sequence. In the URR, the average resonance widths for each energy of reference are prescribed in the ENDF evaluation [15]. PURM determines how many resonance pairs are needed for each (l, J) sequence using the Δ_3 -statistics test developed by Dyson and Mehta [16].

The Δ_3 -statistics test quantifies the mean-square deviation between the number of observed energy levels between E_l and E_h :

$$\Delta_3 = \text{Min}(a, b) \left[\frac{1}{2L} \int_{E_l}^{E_h} (N(E) - aE - b)^2 dE \right], \quad (48)$$

where $2L$ is the total number of levels and $N(E)$ is the observed cumulative number of resonances. The values of a and b are constants that are determined on-the-fly by applying a linear fit to the cumulative number of levels, a requirement for the minimization of the Δ_3 value. The theoretical average value of the Δ_3 -statistics test is given by:

$$\langle \Delta_3 \rangle = \frac{1}{\pi^2} [\ln(n) - 0.0687], \quad (49)$$

where n is the number of energy levels observed in the interval. The purpose of the Δ_3 -statistics test is to ensure that the sampled level-spacing distributions are a sufficient representation of the resonance behavior in the neighborhood of the energy of reference. Once the resonance-pair sequence is determined, the reaction widths for each resonance are sampled from Chi-square distributions according to the number of degrees of freedom prescribed for each reaction type. The Chi-square distribution with ν degrees of freedom can be written as

$$\chi^2(x, \nu) = \frac{x^{\frac{\nu}{2}-1} e^{-\frac{x}{2}}}{2^{\frac{\nu}{2}} G\left(\frac{\nu}{2}\right)}, \quad (50)$$

where G has been used to represent the mathematical gamma function in order to avoid confusion with the resonance reaction widths, typically denoted by Γ . Except in the case

of elastic scattering, x is given by

$$x = \frac{\Gamma_{\lambda c}}{\langle \Gamma_{\lambda c} \rangle}, \quad (51)$$

where c represents the channel under consideration, $\Gamma_{\lambda c}$ is the sampled resonance width for channel c for level λ , and $\langle \Gamma_{\lambda c} \rangle$ is the average channel width for channel c in the vicinity of level λ . In the case of elastic scattering, x is instead defined to be

$$x = \frac{\Gamma_{\lambda n}^l}{\langle \Gamma_{\lambda n}^l \rangle}, \quad (52)$$

where $\Gamma_{\lambda n}^l$ is the sampled reduced neutron width for angular momentum l for level λ , and $\langle \Gamma_{\lambda n}^l \rangle$ is the average reduced neutron width for angular momentum l around resonance λ . It should be noted that reduced neutron width prescribed here is not related to the neutron width by the theoretical definition, but obeys the experimental definition, given by

$$\Gamma_{\lambda c} = \Gamma_{\lambda n}^l \sqrt{E} V_l(\rho), \quad (53)$$

where E is the resonance energy, ρ is the product of the channel radius and wave number, and V_l is given in terms of the penetrability, P_l , as

$$V_l(\rho) = \frac{P_l}{\rho}. \quad (54)$$

The number of degrees of freedom varies for each reaction. When the neutron width is assigned only one degree of freedom, the Chi-square distribution is equivalent to the Porter-Thomas distribution, given by

$$PT(x) = \frac{e^{-\frac{x}{2}}}{\sqrt{2\pi x}} \quad (55)$$

Once PURM has a complete resonance-pair sequence for history, the various cross sections are calculated at the energy of reference. The temperature-dependent cross sections are calculated by Doppler broadening the SLBW cross section directly using the psi-chi method [17]. In the psi-chi method, the temperature-dependent scattering cross section can be written, in a modified NJOY notation [18], as

$$\sigma_{potential} = \sum_l \frac{4\pi}{k^2} (2l + 1) \sin^2 \phi_l, \quad (56)$$

$$\sigma_{m\lambda} = \frac{4\pi}{k^2} \left(\frac{2J + 1}{2(2I + 1)} \right) \frac{\Gamma_{n,\lambda}}{\Gamma_\lambda}, \quad (57)$$

$$\begin{aligned} \sigma_{elastic} = & \sigma_{potential} \\ & + \sum_l \sum_\lambda \sigma_{m\lambda} \left\{ \left[\cos 2\phi_l - \left(1 - \frac{\Gamma_{n,\lambda}}{\Gamma_\lambda} \right) \right] \psi(\theta, x) \right. \\ & \left. + \sin(2\phi_l) \chi(\theta, x) \right\}, \end{aligned} \quad (58)$$

$$\sigma_{capture} = \sum_l \sum_\lambda \sigma_{m\lambda} \frac{\Gamma_{cap,\lambda}}{\Gamma_\lambda} \psi(\theta, x), \quad (59)$$

$$\sigma_{fission} = \sum_l \sum_\lambda \sigma_{m\lambda} \frac{\Gamma_{fiss,\lambda}}{\Gamma_\lambda} \psi(\theta, x), \quad (60)$$

where again k is the neutron wave number, l denotes the orbital angular momentum, ϕ_l is the phase shift, λ indicates the resonance under consideration, J is the total angular momentum, I is the spin of the target nucleus, and the Doppler line-shape functions are represented by $\psi(\theta, x)$ and $\chi(\theta, x)$. The temperature-dependent variable θ is given by

$$\theta = \frac{\Gamma_\lambda}{\sqrt{\frac{4k_B T E}{A}}}, \quad (61)$$

where k_B is the Boltzmann constant, T is the absolute temperature, and A is the atomic weight ratio. The temperature-independent variable x is given by

$$x = \frac{2}{\Gamma_\lambda} \left[E - \left(E_\lambda + \frac{S_l(E_\lambda) - S_l(E)}{2P_l(E_\lambda)} \Gamma_{n,\lambda}(E_\lambda) \right) \right], \quad (62)$$

where we have introduced the energy-dependent shift factor and the penetrability factor, S_l and P_l , respectively. The line-shape functions can then be written as

$$\psi(\theta, x) = \frac{\sqrt{\pi}}{2} \theta \operatorname{Re} \left[\frac{i}{\pi} \int_{-\infty}^{\infty} \frac{e^{-t^2}}{\frac{\theta}{2}(x+i) - t} dt \right] \quad (63)$$

and

$$\chi(\theta, x) = \frac{\sqrt{\pi}}{2} \theta \operatorname{Im} \left[\frac{i}{\pi} \int_{-\infty}^{\infty} \frac{e^{-t^2}}{\frac{\theta}{2}(x+i) - t} dt \right]. \quad (64)$$

Even though it is not as accurate as some other methods [19], the psi-chi method is a powerful tool for generating Doppler-broadened cross sections. The method allows

for the direct computation of the Doppler-broadened cross section at a desired energy, without the need to reconstruct the cross section in the surrounding area. Since the module PURM only needs the cross sections to be tabulated at a small set of energy points (namely, the energies of reference), this method is well-suited to the task. However, this cross section formulation can also lead to negative elastic cross section values. If PURM encounters a negative cross section, it will resample the resonance parameters and recalculate all cross sections for that set. For a given history, all desired temperature-dependent cross sections could be calculated using the same set of resonance parameters by varying the temperature parameter, T , in Eq. (61).

This entire sampling procedure is carried out for many histories, and used to create the temperature-dependent probability tables at the energy of reference. A simple flowchart illustrating the PURM procedure is given in Fig. 1.

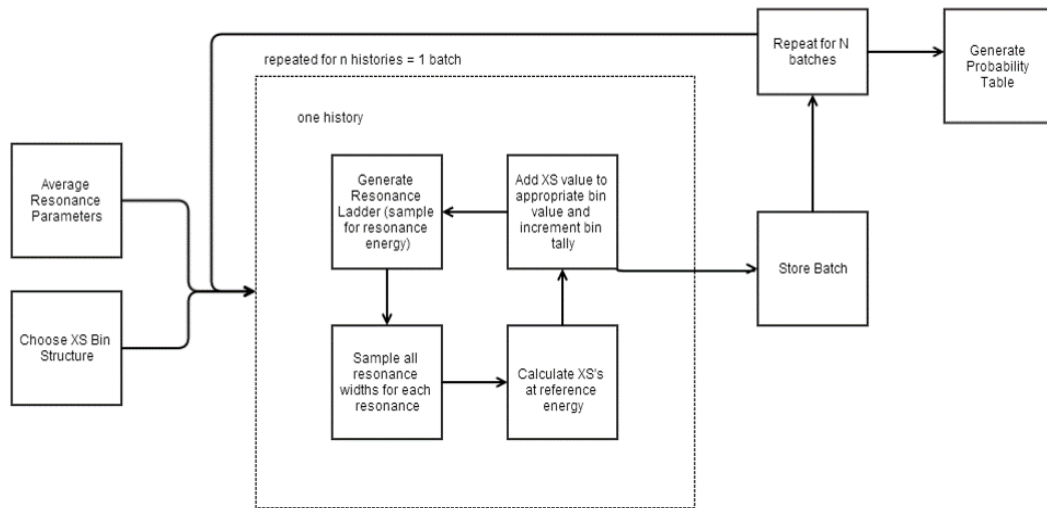


Figure 1. Flowchart depicting the PURM reconstruction procedure.

CHAPTER 3

NEW URR METHOD

In this chapter, the new URR method is presented. The methodology works in a way similar to PURM, but utilizes the more rigorous RML cross-section format. Appropriate modifications have been made to the sampling routine to include the additional channels that were previously unavailable under the SLBW approximation. Necessarily, the LH Doppler broadening routine has replaced the psi-chi method, as the psi-chi method relies on the SLBW cross-section representation. The probability table generation has been implemented in a way that is nearly identical to PURM, generating normalized cross-section factors at the ENDF prescribed energies of reference.

Generating the Resonance-Pair Sequence

The new AMPX module developed in this dissertation generates a resonance-pair sequence in a way similar to the PURM method outlined in Chapter 2. The resonance energy level spacings are distributed according to a Wigner distribution, which can be integrated to yield an explicit cumulative distribution function:

$$W_{CDF}(x) = 1 - e^{-\frac{\pi x^2}{4}}. \quad (65)$$

This cumulative distribution function can be inverted to yield a straightforward way to sample x . If we let ρ represent a random number in the range $(0,1)$, we find that x is given by

$$x = \sqrt{\frac{-4}{\pi} \ln \rho}. \quad (66)$$

The sampled spacing, $D_{l,J}$, is given by the product of x and the average level spacing $\langle D_{l,J} \rangle$. After the spacing has been sampled, the first two resonances are then placed around one of the energies of reference. This is done by first sampling a random number ρ' uniformly from the range (0,1). The first resonance is then placed at

$$E_{\lambda=1} = E_{ref} + \rho' D_{l,J}, \quad (67)$$

and the second resonance is placed at

$$E_{\lambda=0} = E_{ref} + (\rho' - 1) D_{l,J}. \quad (68)$$

This allows the starting point of the resonance-pair sequences to shift around the energy of reference while still maintaining the appropriate level spacing. These two resonances serve as the starting point to build the rest of the sequence. The sequence begins by climbing up from the starting resonance at $E_{\lambda=1}$, with the location of each new resonance given by

$$E_{\lambda=n+1} = E_{\lambda=n} + D_{l,J,n+1}, \quad n > 0, \quad (69)$$

where $D_{l,J,n+1}$ represents the n th sampling of the level spacing. In a similar fashion, the bottom of the sequence is then generated by descending from $E_{\lambda=0}$, with the location of each new resonance given by

$$E_{\lambda=n-1} = E_{\lambda=n} - D_{l,J,n-1}, \quad n \leq 0, \quad (70)$$

where $D_{l,J,n-1}$ represents the n th sampling of the level spacing during the climb down. In contrast to PURM, the energy-dependent average level spacing is updated to reflect the correct parameter set.

During the construction of the resonance-pair sequence, the sampled resonance energies will appear increasingly further away from the energy of reference. In fact, it is typical that a large portion of the sampled energy levels will be so far from the original energy of reference, that they are being placed near a new energy of reference, which has its own set of average parameters. The new methodology will update the average parameters to reflect this change in energy position. There are a few options for determining which set of average parameters to use, including linear interpolation between neighboring sets or simply using the closest set. The default choice for determining the appropriate parameter set is to use the nearest energy of reference to the last sampled resonance energy. This default choice is in agreement with the ENDF prescription for cross section reconstruction, which dictates that any interpolation is carried out on the cross sections, and not the parameter sets. However, interpolation on parameters seems more appropriate than on the cross section. The data evaluation should make sure that the results obtained by energy and parameter interpolations coincide.

Once the resonance locations are determined, a set of resonance reaction widths are sampled from appropriate Chi-square distributions according to the number of degrees of freedom in a manner analogous to the PURM sampling technique. As with the average level spacing, the average reaction widths are updated to use the parameter set at the nearest energy of reference.

It is worth noting that the shape of the Porter-Thomas distribution leads to most of the sampled neutron widths falling far below the average value; in fact, the distribution is skewed so that a fair sampling will lead to nearly 70% of the widths falling below the average width. By contrast, the fission reaction is typically assumed to be a multi-channel process, and is typically assigned two or three degrees of freedom. In the case of neutron capture, it is assumed a very large number of capture channels are available, such that $\nu \rightarrow \infty$, and the associated Chi-square distribution then becomes a Dirac delta function centered at $\langle \Gamma_{\lambda\gamma} \rangle$. Hence, each sampled capture width is identical to the average capture

width, meaning $\langle \Gamma_{\lambda\gamma} \rangle = \Gamma_{\lambda\gamma}$ for all λ . The Chi-square distributions are sampled using a rejection technique and the definition of the Chi-square distribution, namely

$$x = \sum_{i=1}^{\nu} \rho_i^2, \quad (71)$$

where x is the sample following a Chi-square distribution with ν degrees of freedom, and the ρ_i are independent, standard normal random variables.

The PURM sampling procedure only generates SLBW resonance parameters, which do not allow for the inclusion of multiple channels per spin-group definition. However, the new URR methodology does allow for the inclusion of multiple channels. Unfortunately, since ENDF only allows the use of the SLBW format in the URR, the higher-order channel terms are not included in the evaluation.

Since the RML format allows all channels, they should all be included in the computation. While the URR ENDF evaluations do not provide all of the channels explicitly, the missing channels can be determined using vector algebra from the neutron spin, intrinsic target spin, orbital angular momentum, and total angular momentum. The given ENDF parameters and user-defined particle-pair definitions are given to the program SAMQUA [20], which then provides the appropriate (l, s) channel definitions for each spin group and particle pair. Once the new channels are determined, they are assigned a reaction width by sampling from the appropriate distribution in the same way that the original sets of reaction widths were determined. After any necessary additional sampling is complete, the resonance-pair sequence is now defined in a set of RML parameters instead of the SLBW parameters that PURM would generate.

Cross-Section Reconstruction

As with the resolved resonance region, great care must be taken in constructing the grid so that it reflects the true cross-section behavior in the region. The grid is typically much easier to construct in the resolved resonance region, and most code packages will form an energy grid that places more points around resonances and fewer points when the cross section is varying much less rapidly. In most cases, the cross-section data is reconstructed so that linear interpolation between points is accurate to 0.1% or better. This is a perfectly sound way to reconstruct the cross section, as it avoids providing inconsequential information in the slowly-varying areas, but still provides an excellent picture of the resonance peaks.

In the resolved resonance region, the aforementioned general energy grid construction procedure works very well, as it has been made in a way that will provide excellent behavior for both temperature broadening routines and Riemann integration schemes. When determining average values from these Riemann integration routines, the spacing between points governs how much each point contributes to the total integral. In effect, regardless of the complexity of the integration routine chosen, the contribution of the change of the function between points in each region is weighted by the spacing between the points. So, even though there are fewer points in the slowly varying regions, their contribution to the average is weighted much more than the contribution from the rapid change over the resonance peaks.

In contrast to the RRR, in which the cross section is well represented by a discrete set of explicit resonance parameters, most codes do not attempt to directly reconstruct the cross section over the entire URR. In the URR, the resonance widths have become smaller than the experimental resolution, and therefore individual resonance parameters can no longer be fit to the data. For this reason, cross section processing codes base their URR reconstruction technique by sampling from the averages of the physical quantities. The cross sections are calculated at the energies of reference prescribed in the ENDF

evaluation using the SLBW approximation, which can be Doppler broadened directly without reconstructing the surrounding energy grid.

While the statistical resonance parameter sampling procedure for the new methodology is similar to those used for SLBW calculations, the RML approximation does not allow the same single-point Doppler broadening. Hence, in order to obtain the temperature-broadened cross section at each energy of reference, the 0K cross sections must be accurately reconstructed in the neighborhood of the energies of reference. Therefore, the cross section reconstruction necessary for the new URR methodology requires an approach identical to those used in the RRR.

In order for the reconstruction to accurately represent the cross section behavior, the energy grid must be defined so that the resonance peaks are not masked by the smooth cross section behavior. If the energy grid spacing is too large, the reconstruction will miss the resonance peaks entirely, and only capture the smoothly varying background cross-section. For example, in the case of ^{238}U , if an energy spacing of 0.01 eV is used, roughly 75% of the resonance contribution to the elastic scattering cross section is not represented on the grid at all. This is due to the resonance not falling haphazardly onto a grid point, or not being close enough to a grid point, since the elastic width of ^{238}U in the unresolved resonance region is on the order of 0.001 eV.

If one were to attempt to use a hyper-fine mesh, then the driving force behind the energy grid spacing must be the minimum non-zero, contributing reaction width found amongst all the sampled resonances. Using ^{238}U as an example, the minimum reaction width is likely to be the elastic scattering channel, which is computed using a sample taken from a Porter-Thomas distribution. Due to the nature of the Porter-Thomas distribution, it is not uncommon for the minimum elastic scattering width to be on the order of 10^{-12} eV. For an evenly meshed energy grid over the unresolved resonance region of ^{238}U , the grid would require on the order of 10^{17} points. Hence, in the case of ^{238}U , this makes creating an evenly meshed energy grid an intractable problem.

Since using an evenly spaced energy grid is effectively impossible, one might consider using a different metric to balance the contribution from the resonant and non-resonant cross-section behavior. Considering that most of the resonance peaks have very small widths, most of them will be missed on a coarse mesh. However, since those peaks are being missed, this means that the coarse mesh is effectively only capturing the non-resonant behavior of the cross section.

One might try to balance the contribution from the resonant and non-resonant behavior equally by using an equal number of points in the two regions. In order to capture the resonance peaks, one could construct a fine grid about each resonance energy. For convenience, this locally fine grid will be referred to as the resonance grid. Once the resonance grid has been constructed, an evenly spaced coarse mesh would then be determined, spanning the entire unresolved resonance region. To balance between the two behaviors, the coarse grid would be created using an equal number of points as the resonance grid. These two grids would then be combined to form the complete energy grid used in the calculation of the probability tables. By construction, the resonant and non-resonant cross-section behavior would have equal weighting through the number of points. Unfortunately, this approach will ultimately fail for very small resonance widths because the peak will be effectively non-existent. If there is no peak, then the region is effectively exhibiting non-resonant behavior, and will be more than double-counting the non-resonant behavior.

Some older codes have attempted to avoid this grid-density problem by using a halving-iteration scheme. These halving schemes start with a coarse grid, and add points to the grid when the cross section at the mid-point can't be accurately interpolated from the neighboring points. Unfortunately, these routines will also sometimes lead to inaccurate cross section representations, especially near inflection points. The new URR methodology avoids all of these issue by using the AMPX module POLIDENT [21] to

perform the energy-grid construction. For completeness, a brief description of the POLIDENT mesh-generation scheme is provided.

POLIDENT starts the reconstruction by first determining an initial fine-energy mesh. The initial spacing between grid points is estimated from the average level spacing and average neutron width, and is given by

$$\Delta E = C \sqrt{\frac{\langle \Gamma_n \rangle}{\langle D \rangle}}. \quad (72)$$

The cross sections are then reconstructed on the fine mesh using the desired cross-section formalism. For the new URR methodology, POLIDENT calls the modern RML algorithm implementation. POLIDENT then numerically determines the location of the critical points of the functions, and adds them to the energy grid. The cross section is then evaluated at each resonance energy to ensure the peaks have been captured, and are added to the fine grid as necessary. A number of points are then added to the grid between the points of inflection and resonance peak; the number of points added increases with increasing value of the slope between the peak and the inflection point, with up to twenty points inserted between them. At this point, a halving-scheme is then used to ensure that the grid sufficiently represents all cross section values in the given energy range.

While a resonance-pair sequence can be generated to span the entire URR, the entire sequence can't be included in the cross section reconstruction at each point due to computational limitations. In order for the temperature broadening to be carried out, the cross section must be constructed on a grid surrounding the energy of reference. In the case of ^{238}U , a typical resonance-pair sequence will consist of over sixty thousand resonances over the span of the URR. If a similar evaluation were provided for the RRR, the number of resonances could feasibly be included in the calculation of the cross

section at every grid point. However, the RRR reconstruction only requires the cross section calculation to be carried out one time at each point on the energy grid. In contrast, in the URR, the cross section must be calculated at every point in the grid for many unique resonance-pair sequences. If every resonance in the sampled sequences were included, the reconstruction on even a relatively small energy grid would require tens of seconds of computation time for each sequence at each energy of reference. If the entire resonance-pair sequence is used for each point on the grid, it would take one the order of CPU-months to reconstruct probability tables in the URR.

Fortunately, it is not necessary to include every resonance in the reconstruction at every point on the energy grid, only the resonances that are near to the energy under consideration. Of course, this requires the definition of what it means for a resonance to be “near” to the grid point. To determine if a resonance is near, we start by examining the R-Matrix, given by

$$R_{cc'} = \sum_{\lambda} \frac{\gamma_{\lambda c} \gamma_{\lambda c'}}{E_{\lambda} - E} \delta_{JJ'}, \quad (73)$$

where $\gamma_{\lambda c}$ is the reduced width amplitude for channel c and resonance λ , E_{λ} is the resonance energy, E is the energy under consideration, δ is the Kronecker delta function, and J and J' are the total angular momentum for channels c and c' , respectively. We will further only consider the elastic scattering cross section, as it is the dominant reaction type for ^{238}U in the URR. For neutrons interacting with ^{238}U , there is only one channel available for elastic scattering in each spin group. Hence, for elastic scattering, our R-Matrix becomes

$$R_{cc'}(E) = R_{cc}(E) = R(E) = \sum_{\lambda} \frac{\gamma_{\lambda}^2}{E_{\lambda} - E} \quad (74)$$

where γ_λ^2 is related to the elastic width by

$$\Gamma_{n\lambda} = 2P_l \gamma_\lambda^2, \quad (75)$$

and P_l is the penetration factor.

We can then write

$$R(E) = \sum_\lambda \frac{\Gamma_{n\lambda}}{2P_l(E_\lambda - E)}. \quad (76)$$

The $\Gamma_{n\lambda}$ are calculated from the sampled partial elastic widths according to the relation

$$\Gamma_{n\lambda} = \Gamma_{n\lambda}^l \sqrt{E_\lambda} \frac{P_l(\rho)}{\rho}, \quad (77)$$

where ρ is given by

$$\rho = \frac{1}{\hbar} \sqrt{\frac{2M^2 E}{(M+1)^2}} a_c, \quad (78)$$

and a_c is the channel radius. We then find that

$$R(E) = \sum_\lambda \frac{\Gamma_{n\lambda}^l \sqrt{E_\lambda} P_l(\rho_\lambda)}{2\rho_\lambda P_l(\rho_E) (E_\lambda - E)}, \quad (79)$$

where ρ_λ is evaluated at E_λ and ρ_E is evaluated at E .

We can now define a resonance as being far from the energy under consideration if

$$\sum_{\lambda_{near}} \frac{\Gamma_{n\lambda} \sqrt{E_\lambda} P_l(\rho_\lambda)}{2\rho_\lambda P_l(\rho_E)(E_\lambda - E)} \gg \frac{\Gamma_{n, far} \sqrt{E_{far}} P_l(\rho_{far})}{2\rho_{far} P_l(\rho_E)(E_{far} - E)} = \epsilon_{far}. \quad (80)$$

Since ρ does not vary greatly over the URR of ^{238}U , we can further simplify the expression for ϵ_{far} to

$$\epsilon_{far} \approx \frac{\Gamma_{n, far} \sqrt{E_{far}}}{E_{far} - E}. \quad (81)$$

For ^{238}U , the product $\Gamma_{n\lambda} \sqrt{E_\lambda}$ is on the order of a few eV, so that the contribution is minimal when divided by $E_\lambda - E$, which will be on the order of keV. Computational experience has shown that most resonances (those more than a few thousand eV away) can be ignored, leading to a drastic reduction in computational time, so that each ^{238}U probability table can be calculated within a few days CPU-time.

Doppler Broadening Treatment

The temperature-corrected cross sections are calculated using the Leal-Hwang method, in which the Doppler-broadened cross section is given by [2]:

$$\sigma_{Doppler}(E) = F(v, t)/E, \quad (82)$$

where v is the square root of the energy E , and $F(v, t)$ is the solution of a partial differential equation of the same form as a one-dimensional time-dependent heat equation, given by

$$\frac{\partial^2 F}{\partial v^2} = \frac{\partial F}{\partial t}, \quad (83)$$

where t is related to the temperature of the sample, T , by

$$t = \frac{k_B T}{2M}, \quad (84)$$

with k_B denoting Boltzmann's constant and M representing the target mass. This is the equivalent differential form of the free-gas model integral equation.

This heat-like equation is subject to the initial condition

$$F(v, 0), -\infty \leq v \leq \infty, \quad (85)$$

with boundary conditions

$$\begin{aligned} F(-\infty, t) &= F(-\infty, 0), \\ F(\infty, t) &= F(\infty, 0). \end{aligned} \quad (86)$$

The function $F(v, t)$ can then be calculated using a finite-difference method. If a constant mesh size is used, the explicit finite difference equation for F at v_i and t_j is given by

$$F_i^{j+1} = s(F_{i+1}^j + aF_i^j + F_{i-1}^j), \quad (87)$$

where

$$s = \frac{\delta t}{(\delta v)^2}, \quad (88)$$

and

$$a = \frac{1 - 2s}{s}. \quad (89)$$

As with many finite-difference formulations, the coefficient s must be no greater than 0.5 to ensure numerical stability. By representing F as a Taylor series expansion and choosing $s = 1/6$, it can be shown that the expected error is on the order of

$$\epsilon \propto \frac{(\delta v)^4}{360} \frac{\partial^6 F}{\partial v^6} - \frac{(\delta t)^2}{6} \frac{\partial^3 F}{\partial t^3}. \quad (90)$$

If the mesh size is non-uniform, F can be expressed as [22]:

$$F_i^{j+1} = s_{nc} \left(a_{nc} F_i^j + \frac{2(F_{i-1}^j \delta v_r + F_{i+1}^j \delta v_l)}{\delta v_r + \delta v_l} \right), \quad (91)$$

where s and a are now grid-dependent variables, given by

$$s_{nc} = \frac{\delta t}{\delta v_r \delta v_l}, \quad (92)$$

and

$$a_{nc} = \frac{1 - 2s}{s}, \quad (93)$$

with

$$\delta v_r = v_{i+1} - v_i \quad (94)$$

and

$$\delta v_l = v_i - v_{i-1}. \quad (95)$$

Energy Grid Justification

Since the RM approximation does not allow for single-point Doppler broadening, the new URR methodology requires that the OK cross sections are reconstructed on an energy grid surrounding the energy of reference. In general, the LH Doppler-broadening method provides accurate temperature-corrected cross sections. However, the finite-difference formulation can lead to significant errors near the edge of the energy mesh, which are more pronounced at very high and very low energies [22]; this error is not an issue in the URR, as the energy range does not span very high or very low energies. Below the URR, adding points past the edges of the grid can help alleviate this error. If no additional points are added, the edge error will be substantial, but the grid points far from the energy boundaries will still be very close to the edge-corrected values.

When performing the reconstruction, the best-case scenario occurs when the sampled parameters produce resonances that are substantially different from the energy

of reference. In this case, the LH Doppler broadening will produce cross sections that are effectively identical at the energy of reference, provided that the choice of energy grid includes the resonances closest to the energy of reference. An example of this best-case scenario is given in Fig. 2. For this set of resonance parameters, the total cross section at the energy of reference on each grid differs by less than 10^{-6} .

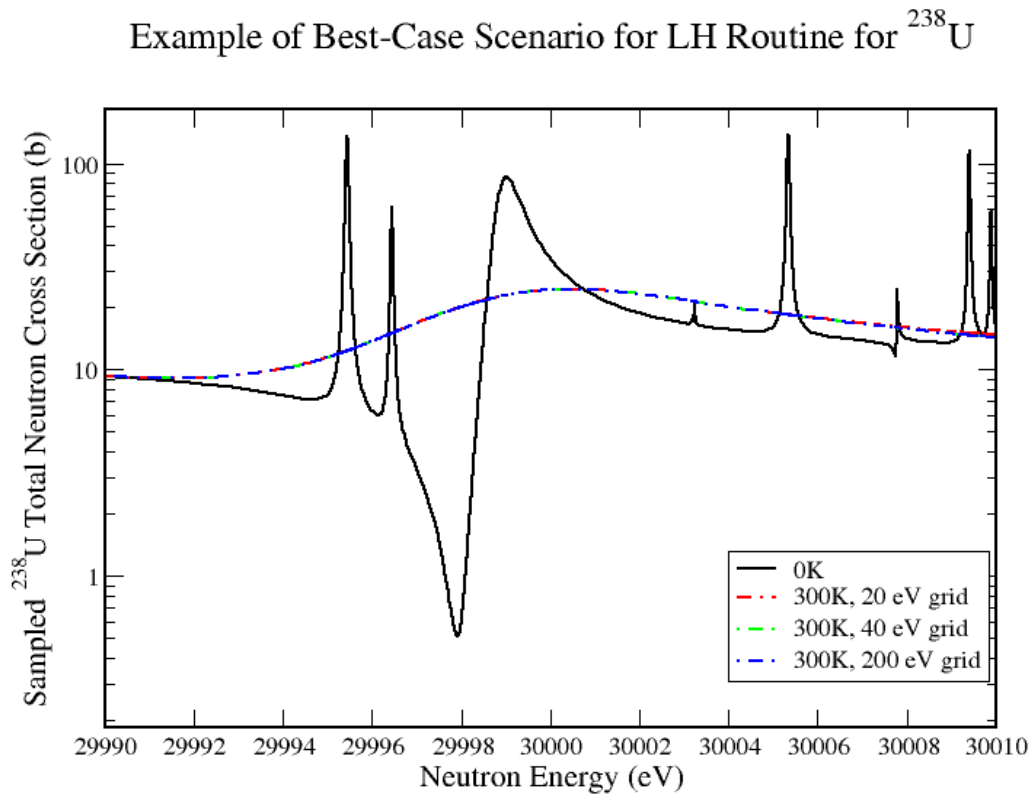


Figure 2. Best-case scenario for LH temperature broadening routine.

The worst-case scenario occurs when the sampled resonance-pair sequence places a resonance very close to the energy of reference and resonances near the edge of the grid. In this case the grid size and center point do have some marginal effect on the temperature-broadened cross section at the energy of reference. These differences are typically very small, with a maximum difference of a few percent between the highest

and lowest reconstructed values. An example of this worst-case scenario is given in Fig. 3 and Fig. 4, with Fig. 3 showing the 0K total cross section and Fig. 4 showing the 300K broadened total cross section on a variety of energy grids. The difference between the highest and lowest estimate of the total cross section is approximately 2.5%. However, this behavior is also not monotonic; a larger grid size might produce a slightly lower or higher value at the energy of reference than a smaller grid. Since the average cross section in each bin of the probability table differs by a much larger percentage, the slight difference in value has a very minimal impact on the results. The graph in Fig. 5 demonstrates the grid's impact on the reconstruction; the reconstructions are much different at their respective end points, but are otherwise in very good agreement with one another.

^{238}U Total Cross Section at 0K for Worst-Case Broadening Scenario

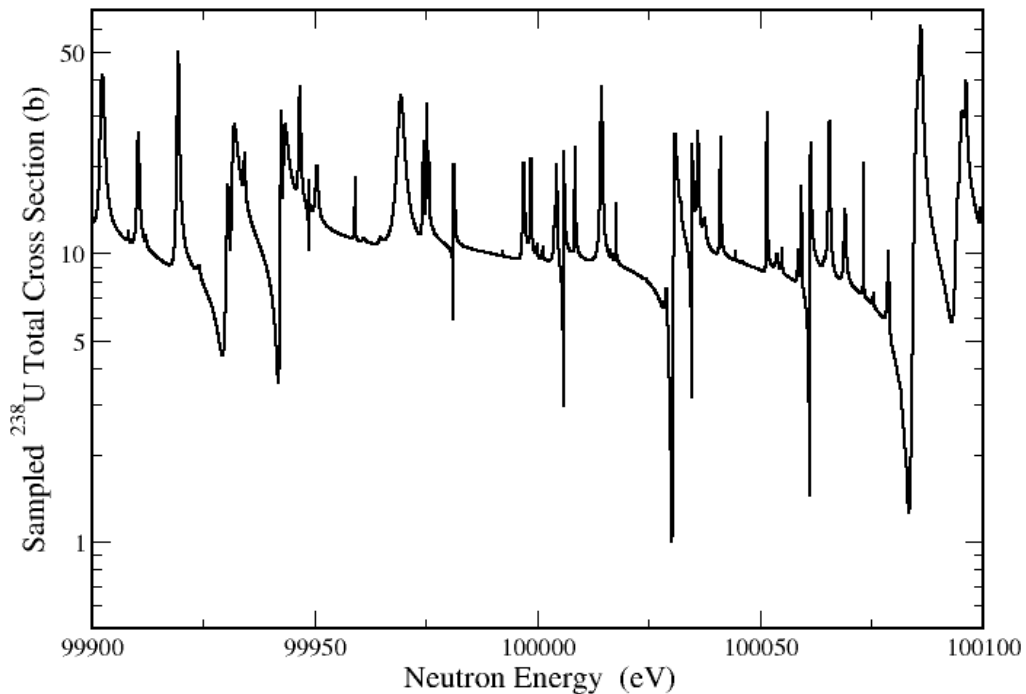


Figure 3. Graph showing 0K total cross section in worst-case scenario for LH temperature-broadening routine.

Worst-Case Broadening Scenario at E_{ref}

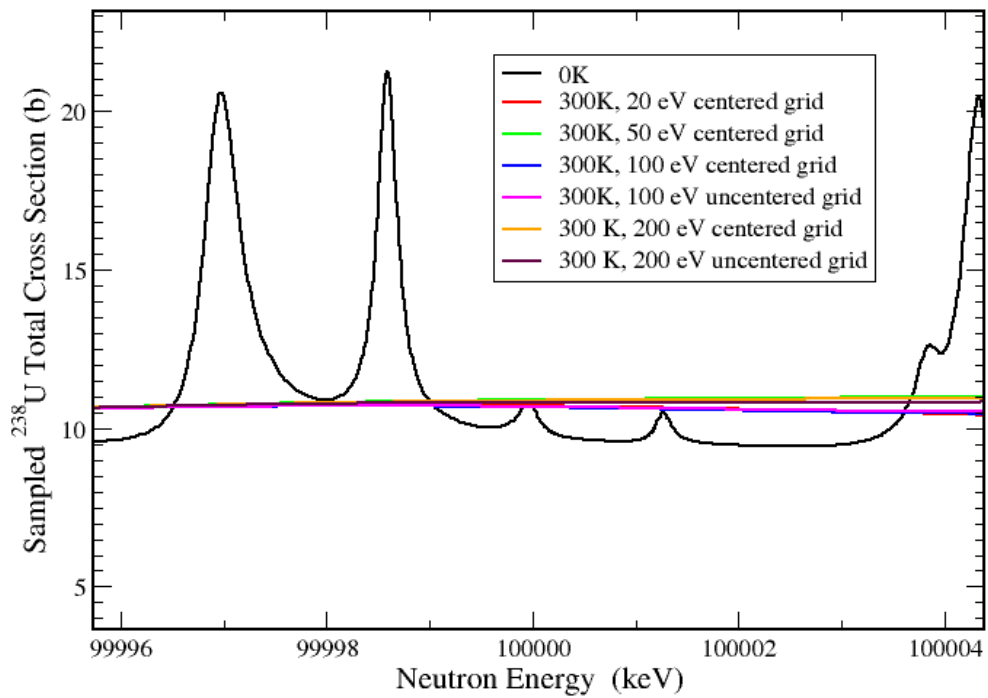


Figure 4. Graph showing impact of grid choice in worst-case scenario for LH temperature-broadening routine near the energy of reference.

Worst-Case Broadening Scenario

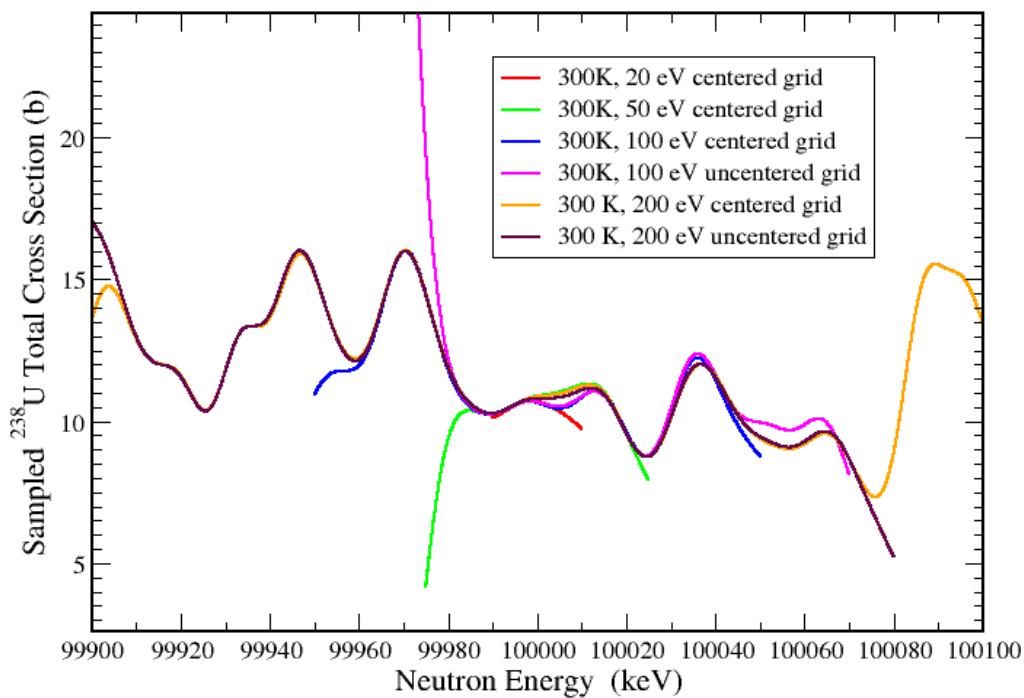


Figure 5. Graph emphasizing the minimal impact the edge-error has on the temperature-broadened cross section near the energy of reference.

As a further justification for the energy grid, let us consider the approximate expression for the SLBW form of the temperature-dependent capture cross section proposed by Bethe and Placzek [23], which can be written as

$$\sigma_{cap}(E, T) \sim \sigma_0 \frac{\Gamma_{cap}}{\Gamma} \left(\frac{E_{res}}{E} \right)^{1/2} \psi(x, \xi), \quad (96)$$

where

$$\psi(x, \xi) = \frac{\xi}{2\sqrt{\pi}} \int_{-\infty}^{\infty} dy \frac{e^{-((x-y)/\xi)^2}}{1+y^2}, \quad (97)$$

with

$$x = \frac{2(E - E_{res})}{\Gamma} \quad (98)$$

and

$$\xi = \frac{\Gamma}{\Gamma_D}. \quad (99)$$

In the last equation, Γ_D is known as the Doppler width, and is given by

$$\Gamma_D = \left(\frac{4E_{res}kT}{A} \right)^{1/2}. \quad (100)$$

In the case of ^{238}U , the Doppler width in the URR will be relatively small. The URR spans from 20 keV to just above 149 keV, so that all of the sampled E_{res} will be more than 10 keV and much less than 200 keV. Even for large values of the thermal energy kT , the Γ_D will be on the order of a few to tens of eV. In the URR of ^{238}U , the total width Γ will typically on the order of 0.1 eV, and in rare cases on the order of 1 eV.

The contribution of the resonance at E_{res} is only important to the cross section calculation at E when the value of the ψ function is large. In the rare case of a large Γ on the order of eV, ξ will be between 0.5 and 1, depending on whether we are in the lower or upper end of the URR. If the resonance is located right at the edge of the energy grid, then for the proposed choice of a 20 eV grid, x will have a magnitude of about 20. If we evaluate ψ for these values of ξ and x , we find that the resonance contributes only 0.25% of its peak value at E . In the more typical case, ξ would be on the order of 10^{-2} or 10^{-3} , and x will have a magnitude much larger than 50, leading to a ψ of less than 0.1%. This is why it is acceptable to Doppler broaden the cross section onto a small grid around the reference energy, as the far away resonances will have increasingly smaller impact on the Doppler broadening at E , provided that the resonances in question have small widths in comparison to the Doppler width and are located at an E_{res} substantially far from E .

Probability Table Construction

Once the cross section has been reconstructed and temperature broadened, the probability tables can be created. Here, a probability table is a tabular representation of the average behavior of the cross section for each reaction type over a well-defined energy range. This approach is used in the unresolved resonance region out of necessity; in this region, the resonance behavior has surpassed detector resolution, and is thus unable to have the same parameters fit to the data as in the resolved resonance region. Hence, the probability table approach allows for the average behavior, as taken from detection measurements, to be reflected by some average set of parameters, as prescribed by the evaluator. One could use this same approach in the resolved resonance region, but it is unnecessary and ill-advised, as the true cross section can be reconstructed on an arbitrarily fine grid with excellent accuracy.

The probability table is divided up by cross section value limits in order to create unique bins for tallying. The bin limits can be set in a variety of ways; in order for interpolation between probability tables to be valid, equi-probable bins are chosen. In order to calculate the bin tallies, the cross section values are typically sorted in order of increasing total cross section. It should be noted that this choice ensures that the bins of each individual probability table will increase monotonically in total cross section, but allows for non-monotonic behavior of all other cross sections. It is necessary for the cross sections to be sorted in increasing order by one of the cross section values to calculate the bin tallies.

Since the individual resonances can't be resolved experimentally, the reaction cross sections must be expressed as an average value at the energy of reference. This gives rise to a Lebesgue expression of the reaction cross section, where we write the expected cross section as [24]

$$\langle \sigma_x(E_{ref}) \rangle = \int_{\sigma_{min}}^{\sigma_{max}} d\sigma'_x p(\sigma'_x | E_{ref}) \sigma'_x, \quad (101)$$

where σ_{min} and σ_{max} are the minimum and maximum values for reaction cross section σ_x , and $p(\sigma'_x | E_{ref})$ is the probability distribution function of σ_x at the energy of reference, E_{ref} . The average value, $\langle \sigma_x(E_{ref}) \rangle$, is also referred to as the infinite-dilution cross section. The infinite-dilution cross section will not exhibit the same resonance structure present in the URR, but the energy self-shielding effect can be recaptured through the use of probability tables.

Once the bin limits have been set and the cross section values have been sorted, the bin probabilities and average values are calculated. For each batch, the probability assigned to each bin is set as

$$P_{i,b} = \frac{n_{i,b}}{n_b}, \quad (102)$$

where $P_{i,b}$ is the probability assigned to bin i for batch b , $n_{i,b}$ is the number of points falling within the bin limits of bin i for batch b , and n_b is the total number of grid points used in batch b .

The average cross section for reaction c within bin i for batch b is calculated as

$$\overline{\sigma_{i,b}^c} = \frac{1}{n_{i,b}} \sum_{j=1}^{n_{i,b}} \sigma_{j,b}^c, \quad (103)$$

where $\overline{\sigma_{i,b}^c}$ is the average cross section for reaction c within bin i for batch b , $n_{i,b}$ is again the number of points falling within bin i for batch b , and the $\sigma_{j,b}^c$ are the cross section values for reaction c falling within the bin limits of bin i for batch b .

After the appropriate number of batches has been tallied, the “grand mean” values are calculated. The final probability assigned to bin i , P_i , is given by

$$P_i = \frac{1}{n} \sum_{b=1}^n P_{i,b}, \quad (104)$$

where $P_{i,b}$ is the probability assigned to bin i for batch b and n is the total number of batches processed. The variance for bin i , V_i^2 , is then computed as

$$V_i^2 = \frac{1}{n(n-1)} \sum_{b=1}^n (P_i - P_{i,b})^2. \quad (105)$$

Similarly, the final average cross sections for bin i and reaction c , $\overline{\sigma_i^c}$, is given by

$$\overline{\sigma_i^c} = \frac{1}{n} \sum_{b=1}^n \overline{\sigma_{i,b}^c}. \quad (106)$$

The variance in the cross section for bin i and reaction c , $\Delta_{i,c}^2$, is calculated as

$$\Delta_{i,c}^2 = \frac{1}{n(n-1)} \sum_{b=1}^n (\overline{\sigma_i^c} - \overline{\sigma_{i,b}^c})^2. \quad (107)$$

CHAPTER 4

RESULTS

In this chapter, several numerical results are presented in order to validate the new URR methodology. First, the cross-section reconstructions of several isotopes are presented to verify that the RML algorithm generates the correct OK values. Then, the new ^{238}U probability tables are presented and compared to the PURM results. Finally, several benchmark problems are presented to verify that the new URR methodology creates accurate cross-section factor probability tables.

Resolved Resonance Region

Before implementing the RML algorithm into the new URR methodology, it was first tested by reconstructing the cross sections of several isotopes in the RRR. The OK reconstruction was performed for several isotopes by both the SAMRML code [4] and the new implementation, and the results were compared. For rigorous testing, the isotopes chosen for testing represent a wide range of masses and reaction types. Here, the OK RRR reconstructions are presented for ^{16}O , ^{19}F , ^{35}Cl , ^{56}Fe , ^{63}Cu , and ^{65}Cu . For the energy-differential cross sections, the reconstructions were performed on an energy grid determined by SAMMY. For the double-differential cross sections, the reconstruction was performed on the same energy grid with an evenly spaced twenty-point angular grid. The new RML algorithm produced energy- and double-differential reconstructions in excellent agreement with the SAMRML results.

^{16}O Cross Sections

One of the advantages of the RML format is its ability to make appropriate Coulomb corrections to handle charged-particle channels. Since an (n, α) reaction opens

for ^{16}O in the RRR above 2.4 MeV, it was a prime candidate for testing the Coulomb-corrected functions used in the calculation. The ^{16}O reconstruction was performed over its entire RRR, spanning from 10^{-5} eV to 6.2 MeV. The OK energy-differential reconstruction was found to be in excellent agreement with the SAMRML results, displaying a relative difference of less than 10^{-6} at all points, except near the (n, α) threshold. This difference is due to instability in the computation induced by the prohibitively small penetrability. However, this difference is of no concern, as the (n, α) cross section is less than 10^{-10} barns near the threshold; once the cross section rises above 10^{-8} barns, the two reconstructions are always in agreement to within a relative difference of 10^{-6} . The ENDF formatted resonance parameter set used to perform the ^{16}O cross-section reconstruction is given in Appendix A, and is a preliminary update of the ^{16}O resonance parameters as part of the Collaborative International Evaluated Library Organization (CIELO) project [25].

In the plotted reconstructions, the smoothly varying cross-sections in the low-energy region have been omitted to provide a clearer image of the resonant peaks in the RRR. The ^{16}O total cross section reconstruction is plotted in Fig. 6, the capture cross section is plotted in Fig. 7, the elastic-scattering cross section is plotted in Fig. 8, and the (n, α) cross section is plotted in Fig. 9.

^{16}O Total Neutron Cross Section at 0K

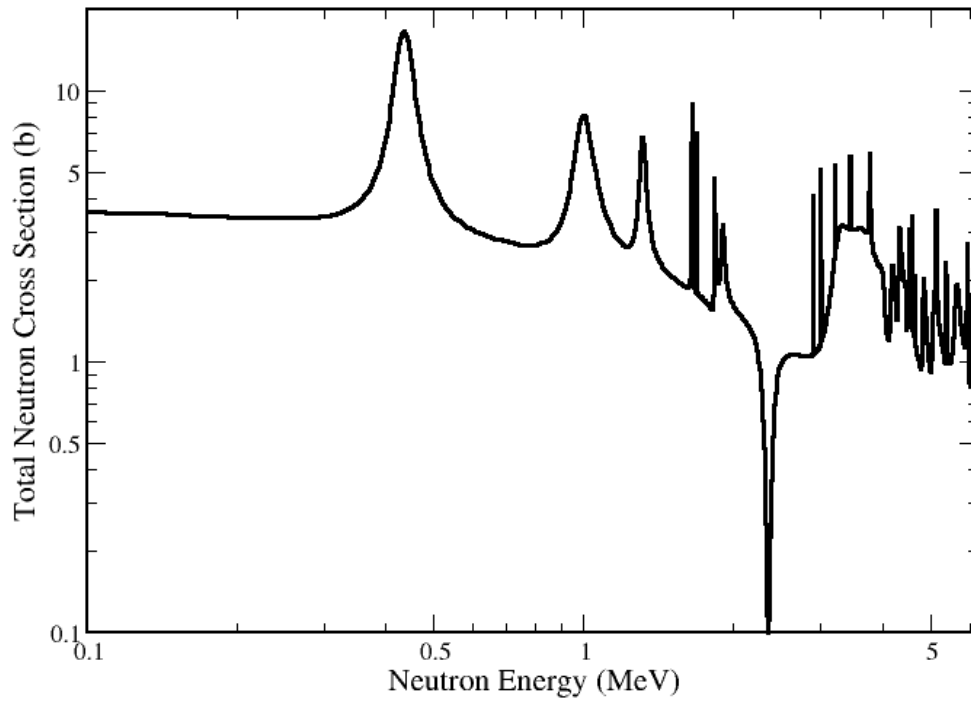


Figure 6. ^{16}O total neutron cross section.

^{16}O Neutron Capture Cross Section at 0K

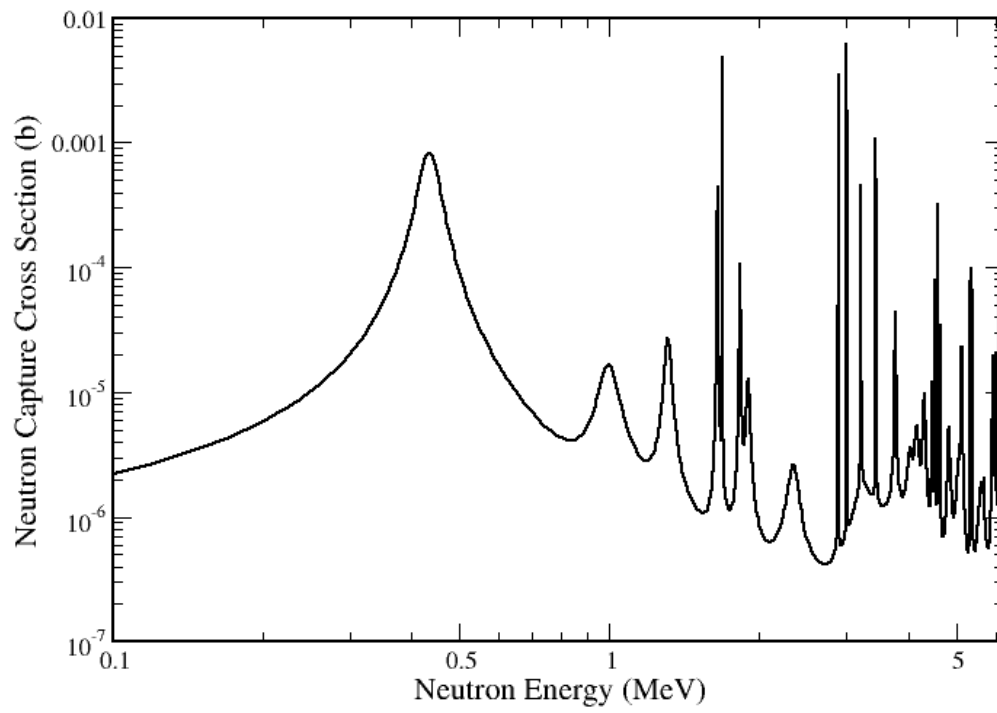


Figure 7. ^{16}O neutron capture cross section.

^{16}O Neutron Elastic Scattering Cross Section at 0K

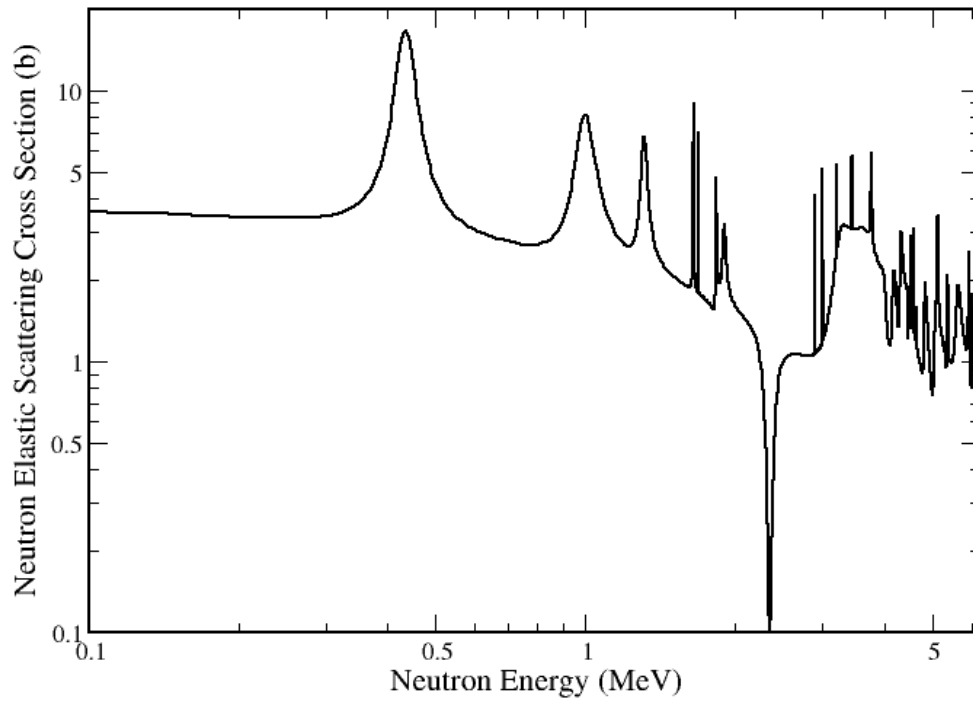


Figure 8. ^{16}O neutron elastic scattering cross section.

^{16}O (n,α) Cross Section at 0K

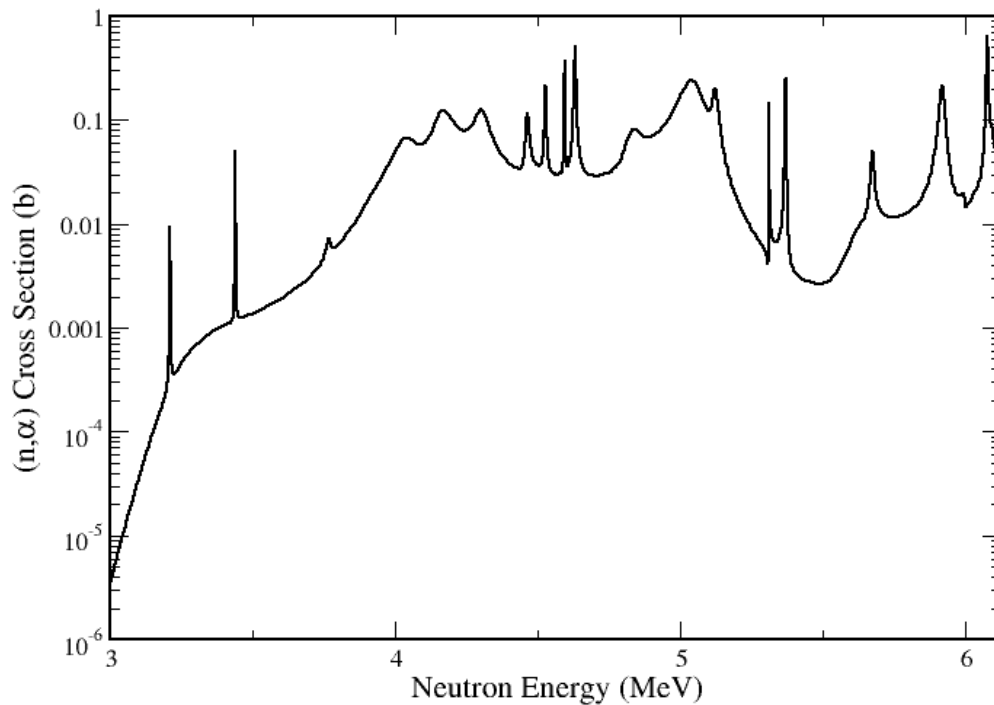


Figure 9. ^{16}O (n,α) cross section.

In addition to the energy-differential cross sections, the ^{16}O double-differential cross sections were reconstructed over the RRR. The new algorithm generated double-differential cross sections that were exactly identical to the SAMRML results. While the results may not be truly identical, they were identical to within the precision of the SAMRML output, which is only printed to four decimal places for the double-differential results. As expected, the ^{16}O double-differential cross sections display non-monotonic behavior in both energy and angle. The double-differential reconstructions for the ^{16}O double-differential elastic scattering and double-differential (n,α) cross sections are shown for all angles at select energies in Fig. 10 and Fig. 11, respectively.

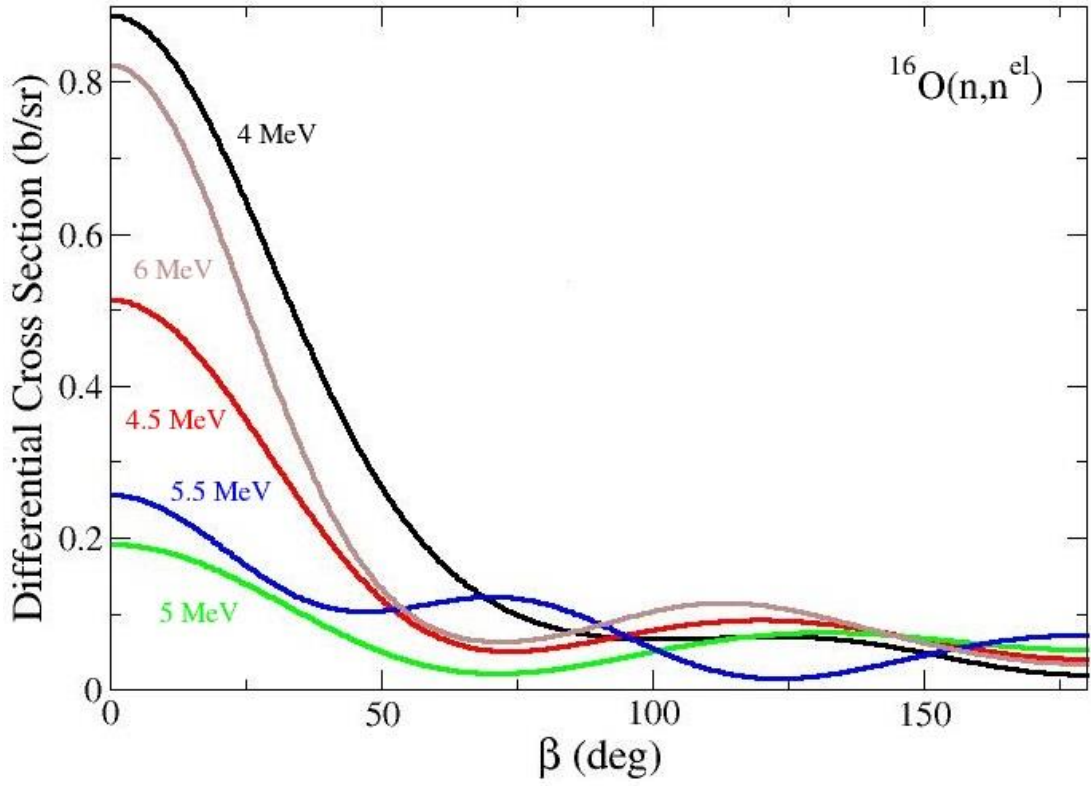


Figure 10. ^{16}O double-differential elastic scattering cross section.

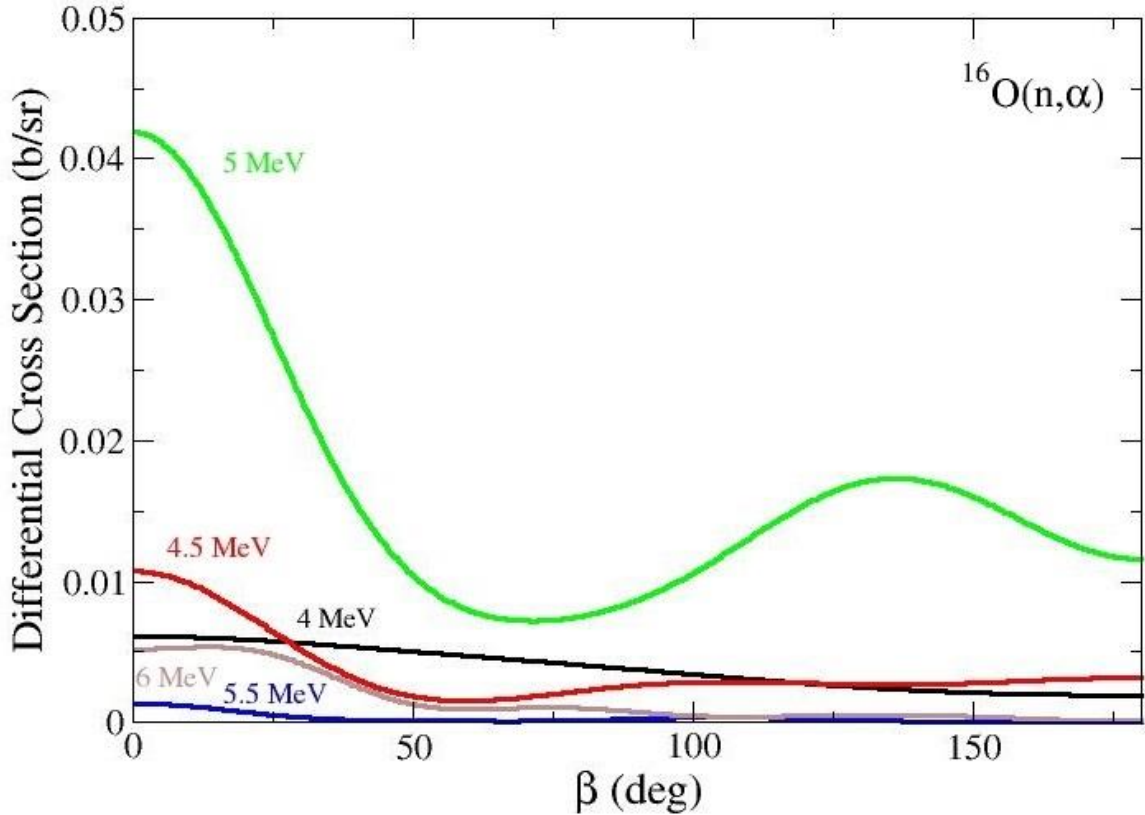


Figure 11. ^{16}O double-differential (n, α) cross section.

^{19}F Cross Sections

Another advantage of the RML format is the capability to independently reconstruct multiple inelastic scattering channels. In the case of ^{19}F , there are two inelastic scattering reactions open in the RRR. The first inelastic scattering reaction opens at threshold energy of 110 keV, and the second inelastic scattering reaction opens around 197 keV. The ^{19}F reconstruction was performed over its entire RRR, spanning from 10^{-5} eV to 1 MeV. As with ^{16}O , the 0K ^{19}F energy-differential reconstruction was found to be in excellent agreement with the SAMRML reconstruction, with a relative difference of less than 10^{-6} , except for the inelastic reactions near their respective thresholds. This difference is again caused by the extremely small penetration factor near the threshold energy. However, this difference only occurs when the cross section is vanishingly small

and of no consequence. The ENDF formatted resonance parameter set used to perform the ^{19}F cross-section reconstruction is given in Appendix B.

The ^{19}F cross section reconstructions shown here omit the smoothly varying cross section in the low-energy region in order to better visualize the resonance peaks in the RRR. The ^{19}F total cross section is depicted in Fig. 12, the capture cross section is plotted in Fig. 13, the elastic scattering cross section is shown in Fig. 14, the first inelastic scattering cross section is displayed in Fig. 15, and the second inelastic scattering cross section is given in Fig 16.

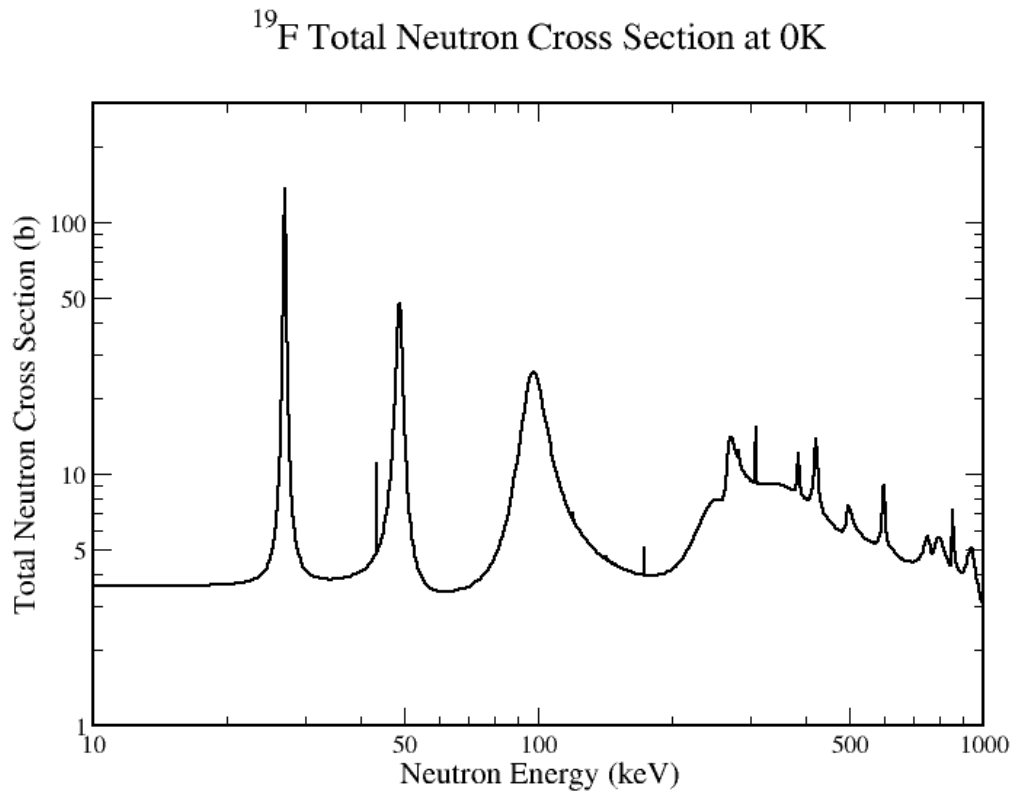


Figure 12. ^{19}F total neutron cross section.

^{19}F Neutron Capture Cross Section at 0K

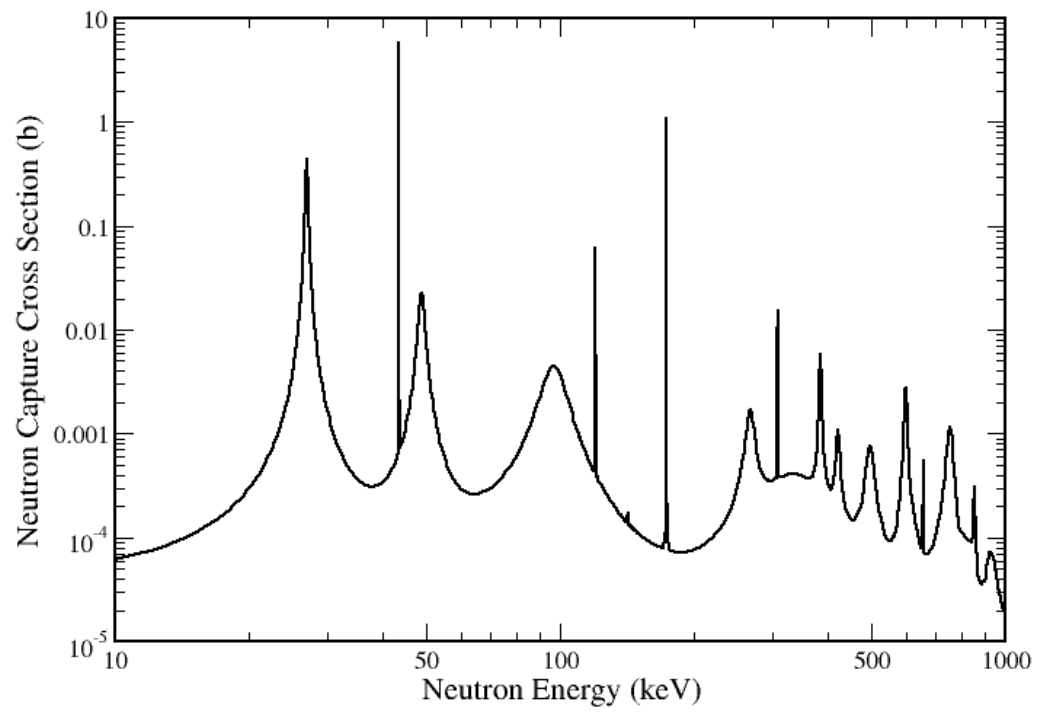


Figure 13. ^{19}F neutron capture cross section.

^{19}F Neutron Elastic Scattering Cross Section at 0K

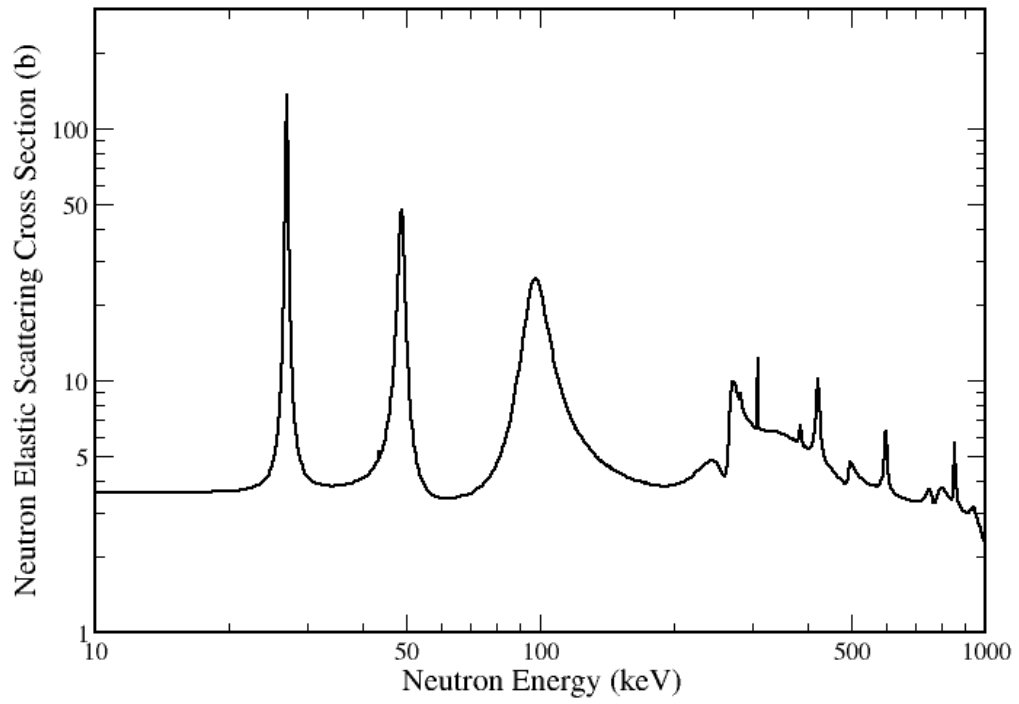


Figure 14. ^{19}F neutron elastic scattering cross section.

^{19}F First Neutron Inelastic Scattering Cross Section at 0K

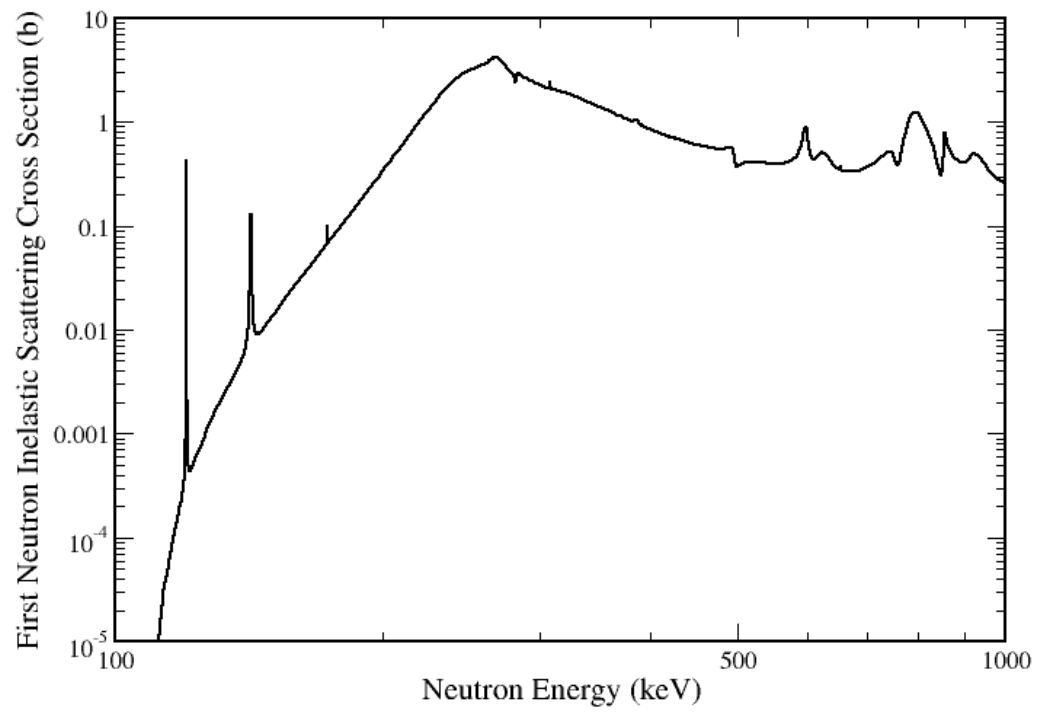


Figure 15. ^{19}F first inelastic scattering cross section.

^{19}F Second Neutron Inelastic Scattering Cross Section at 0K

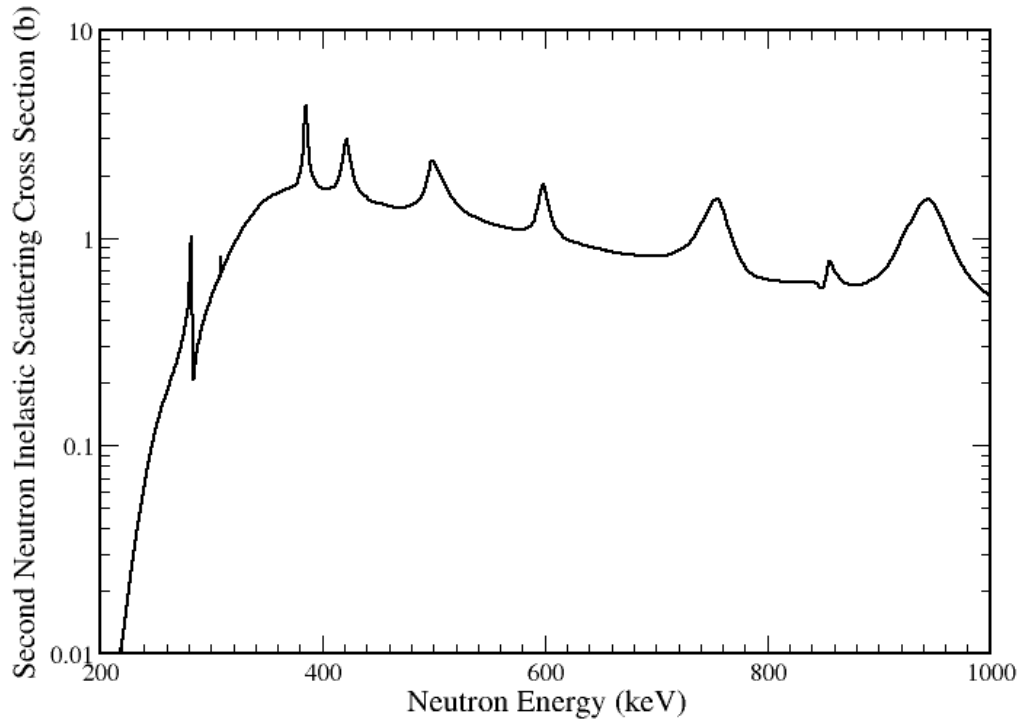


Figure 16. ^{19}F second inelastic scattering cross section.

In addition to the energy-differential cross sections, the ^{19}F double-differential cross sections were reconstructed over the RRR. The new algorithm again generated double-differential cross sections that were exactly identical to the SAMRML results. As with the ^{16}O double-differential cross sections, the ^{19}F double-differential cross sections display non-monotonic behavior in both energy and angle. The double-differential reconstructions for the ^{19}F double-differential elastic scattering, first inelastic scattering, and second inelastic scattering cross sections are shown for all angles at select energies in Fig. 17, Fig. 18, and Fig. 19, respectively.

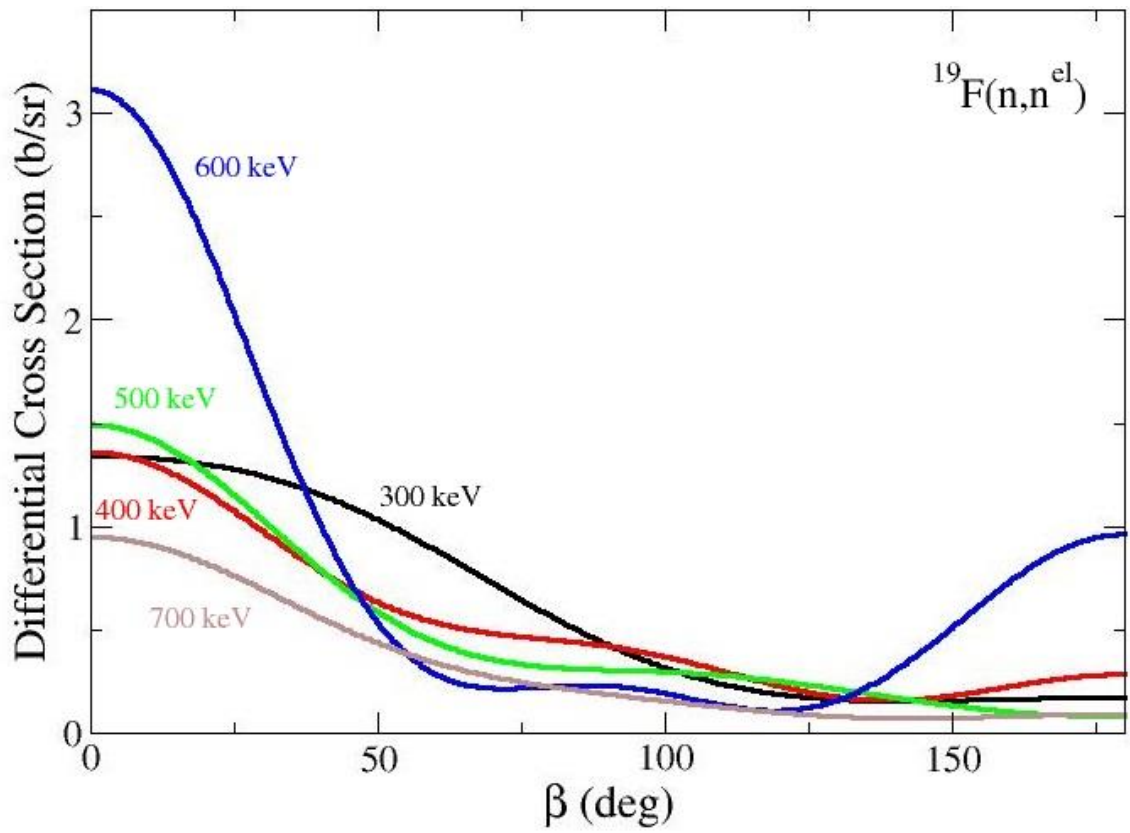


Figure 17. ^{19}F double-differential elastic scattering cross section.

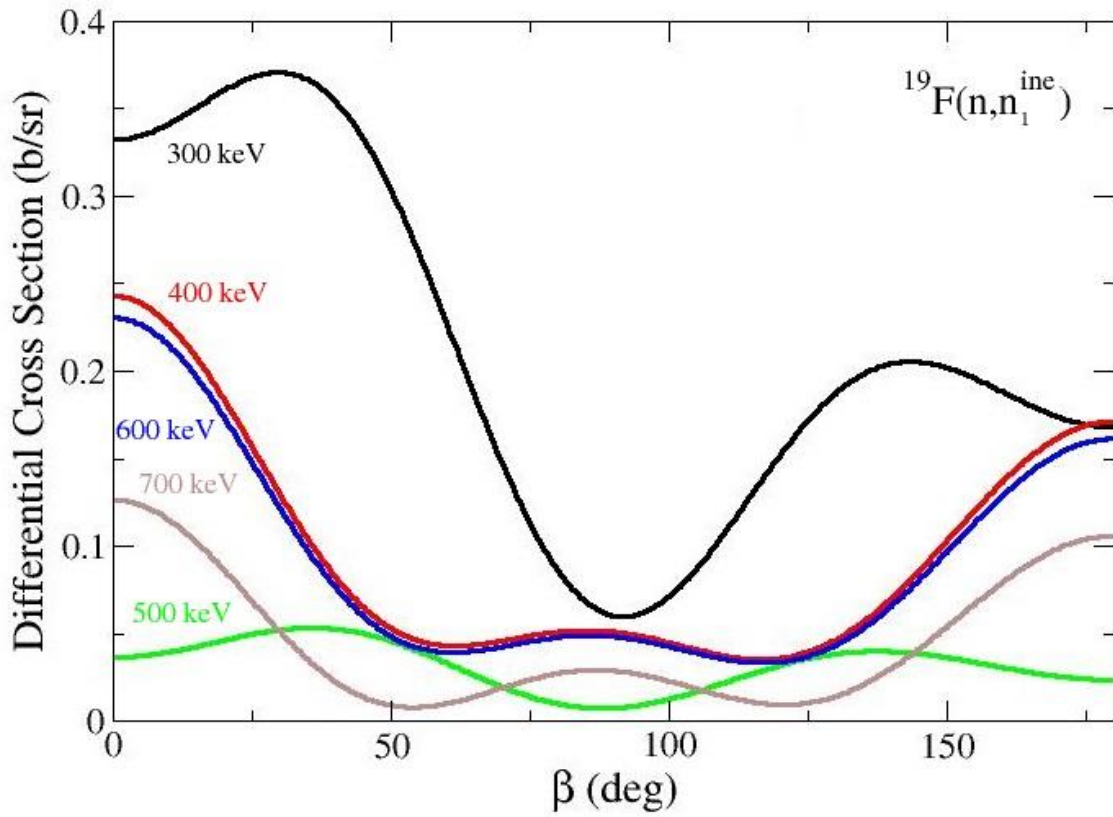


Figure 18. ^{19}F double-differential first inelastic scattering cross section.

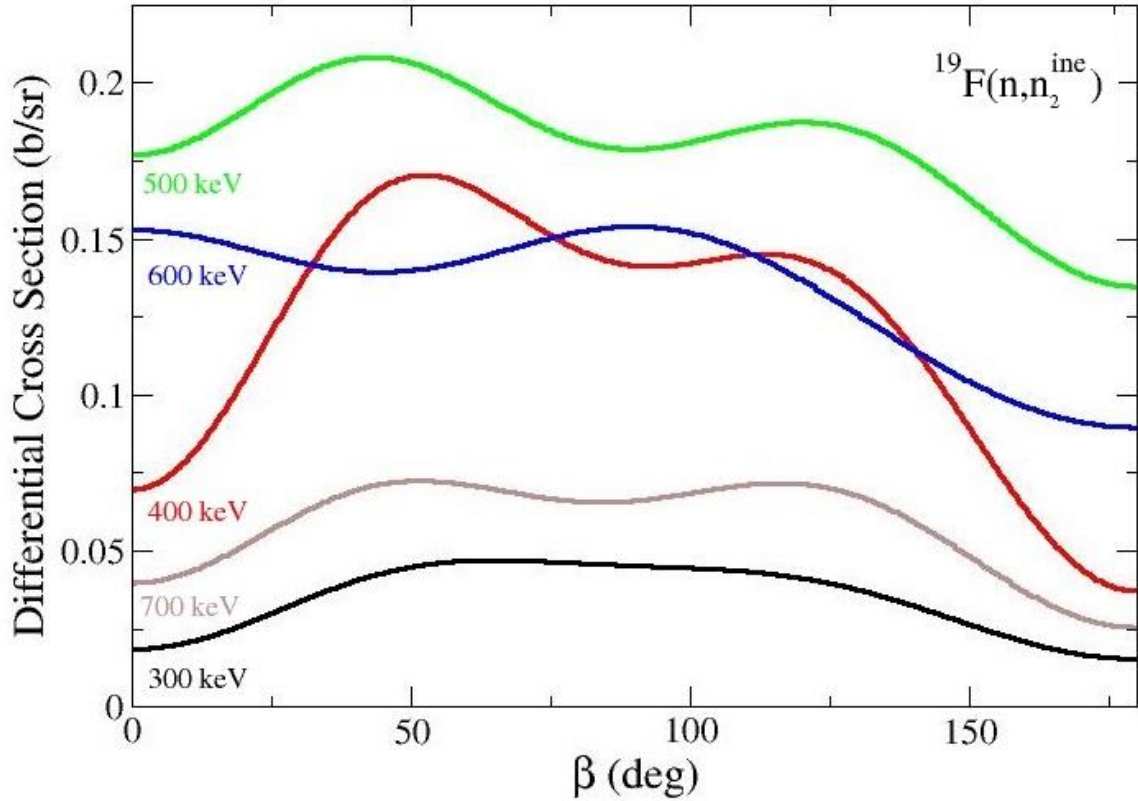


Figure 19. ^{19}F double-differential second inelastic scattering cross section.

^{35}Cl Cross Sections

The isotope ^{35}Cl was chosen to test the ability of the RML implementation to handle a different type of charged particle interaction, namely, the (n, p) reaction. Further, the (n, p) reaction for ^{35}Cl is exothermic, so that there is no threshold energy for the reaction to proceed. The 0K ^{35}Cl energy-differential cross sections were reconstructed over the entire RRR, spanning 10^{-5} eV to 1.2 MeV, and found to be in excellent agreement with the SAMRML reconstruction everywhere, with a relative difference of less than 10^{-6} . Unlike the other cases, there was no slight disagreement found anywhere in the reconstruction, due to the exothermic nature of the (n, p) reaction with ^{35}Cl . The

ENDF formatted resonance parameter set used to perform the ^{35}Cl cross-section reconstruction is given in Appendix C.

The ^{35}Cl cross section reconstructions shown here omit the smoothly varying cross section in the low-energy region to graphically separate the resonance peaks in the RRR. The ^{35}Cl total cross section is depicted in Fig. 20, the capture cross section is plotted in Fig. 21, the elastic scattering cross section is shown in Fig. 22, and the (n,p) cross section is given in Fig 23.

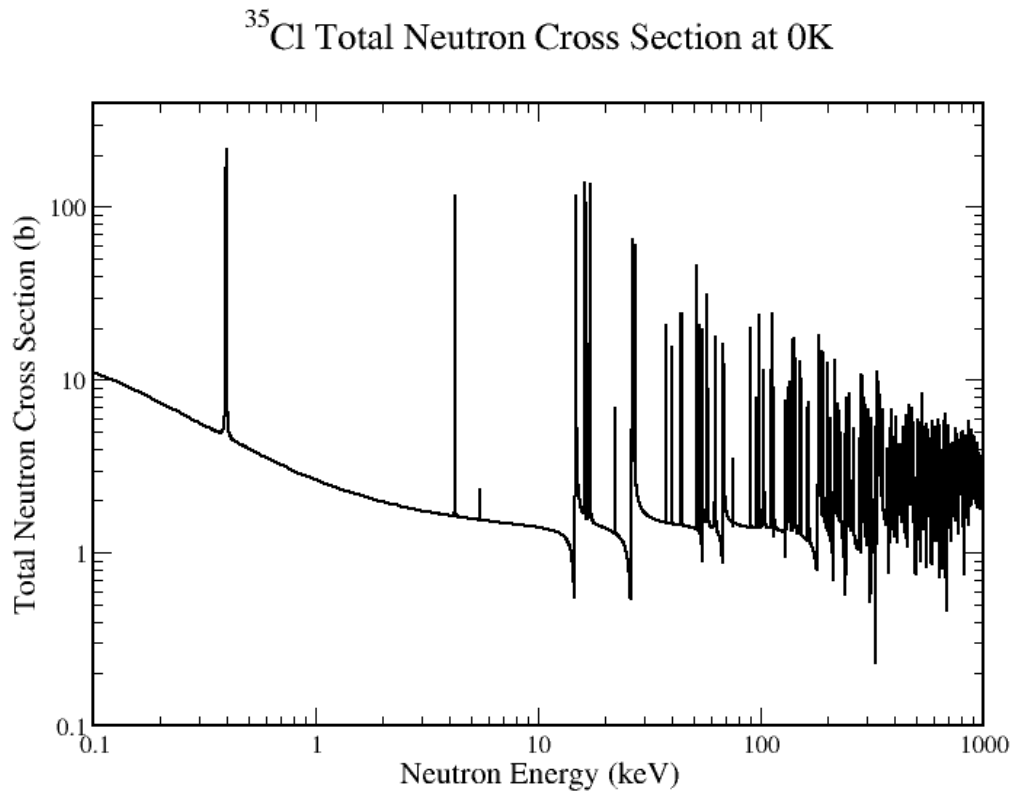


Figure 20. ^{35}Cl total neutron cross section.

^{35}Cl Neutron Capture Cross Section at 0K

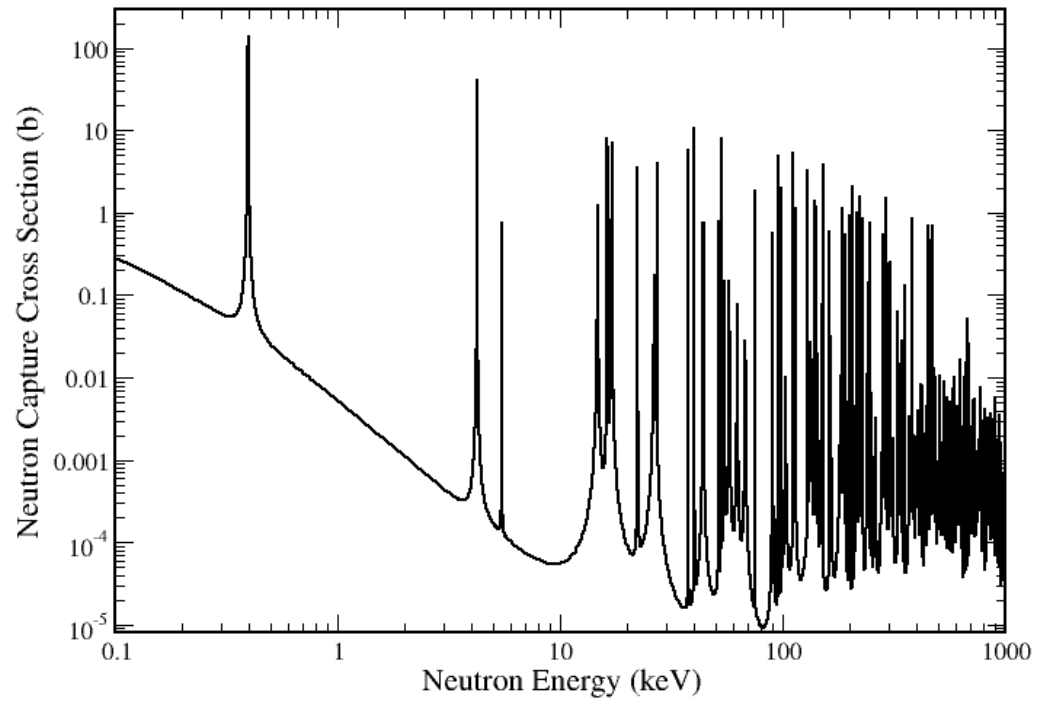


Figure 21. ^{35}Cl neutron capture cross section.

^{35}Cl Neutron Elastic Scattering Cross Section at 0K

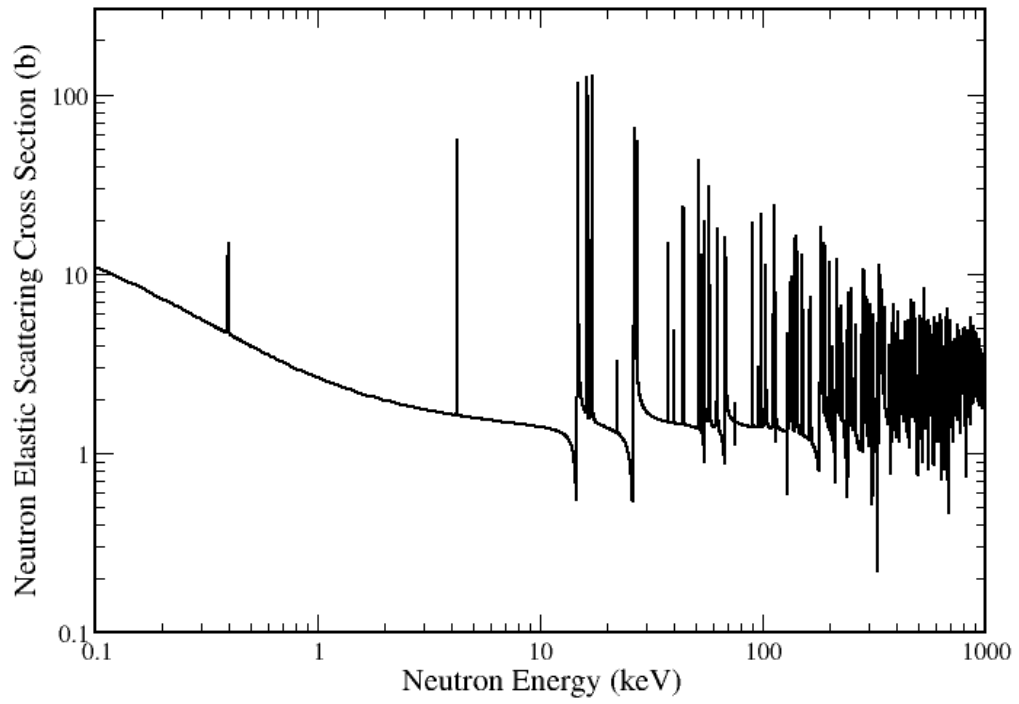


Figure 22. ^{35}Cl neutron elastic scattering cross section.

^{35}Cl (n,p) Cross Section at 0K

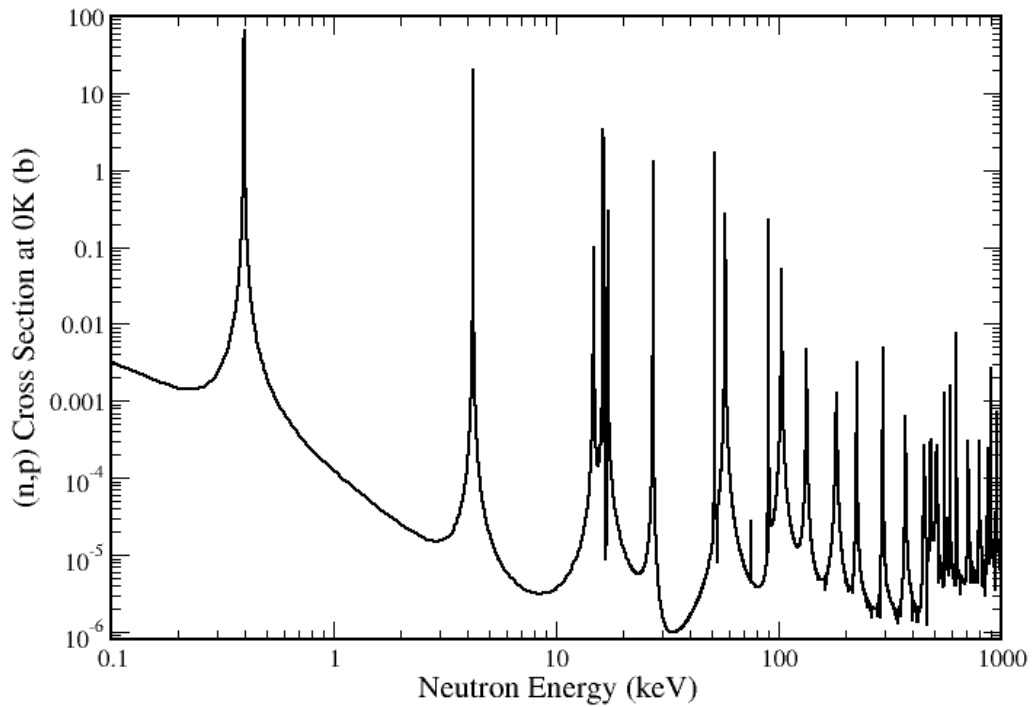


Figure 23. ^{35}Cl (n,p) cross section.

In addition to the energy-differential cross sections, the ^{35}Cl double-differential cross sections were reconstructed over the RRR. As with the other isotopes, the new algorithm again generated double-differential cross sections that were exactly identical to the SAMRML results. The ^{35}Cl double-differential cross sections display non-monotonic behavior in both energy and angle, as expected. The double-differential reconstruction for the ^{35}Cl double-differential (n,p) cross section is shown for all angles at select energies in Fig. 24.

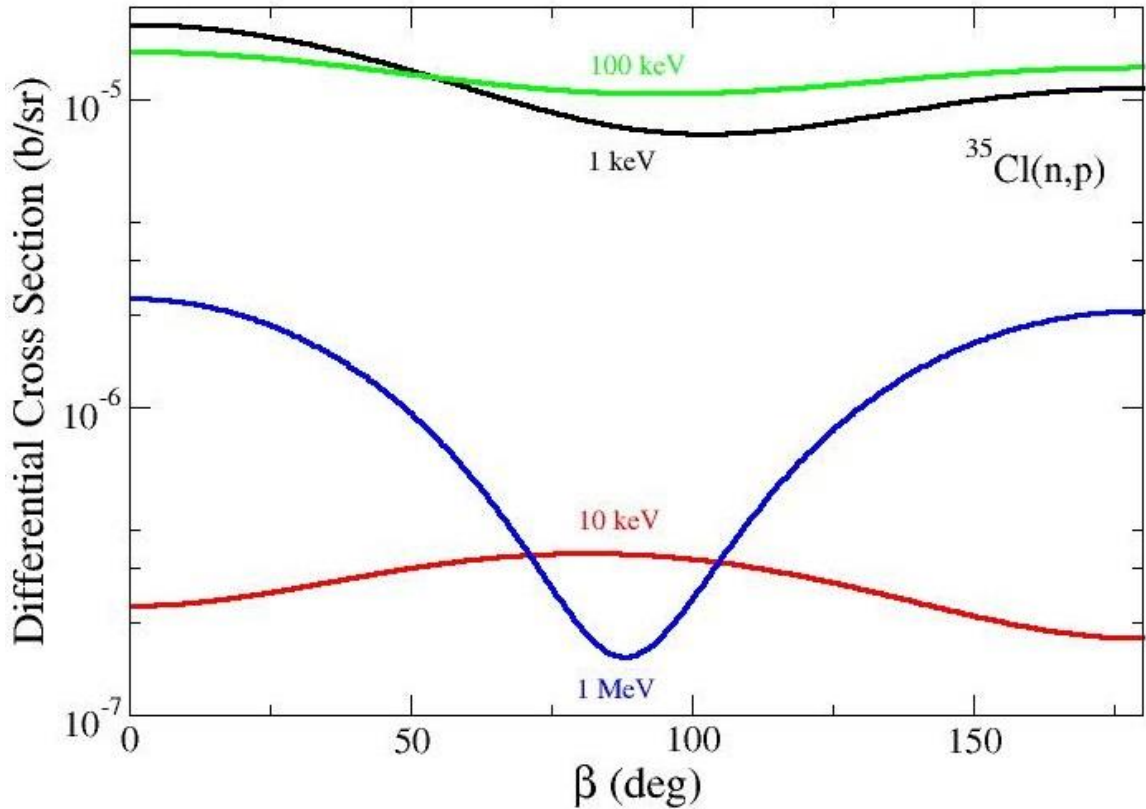


Figure 24. ^{35}Cl double-differential (n, p) cross section.

^{56}Fe Cross Sections

The energy-differential cross sections were reconstructed for ^{56}Fe , a large component of many of the structural materials in a reactor environment. In contrast to ^{19}F , which has two inelastic reactions open in its RRR, there is only one available inelastic reaction in the RRR of ^{56}Fe , spanning from 10^{-5} eV to 2 MeV. As in the other cases, the OK reconstruction of all cross sections agreed with the SAMRML results to within a relative difference of 10^{-6} , except near the inelastic threshold, where once again the cross section is vanishingly small. Once again, this disagreement rapidly dies off away from the threshold, and the reconstructions of all cross sections are found to be in very close agreement. The ENDF formatted resonance parameter set used to perform the reconstruction is not provided, as the data spans nearly two thousand lines. Furthermore,

the resonance parameter set used to perform this reconstruction is also part of the ongoing CIELO pilot project to update the ^{56}Fe nuclear data evaluation [26]. A similar resonance parameter set for ^{56}Fe can be obtained from the National Nuclear Data Center [27], but is only to be used up to 850 keV.

The ^{56}Fe cross section reconstructions shown here omit the smoothly varying cross section in the low-energy region in order to better visualize the resonance peaks in the RRR. The ^{56}Fe total cross section is depicted in Fig. 25, the capture cross section is plotted in Fig. 26, the elastic scattering cross section is shown in Fig. 27, and the inelastic scattering cross section is provided in Fig. 28.

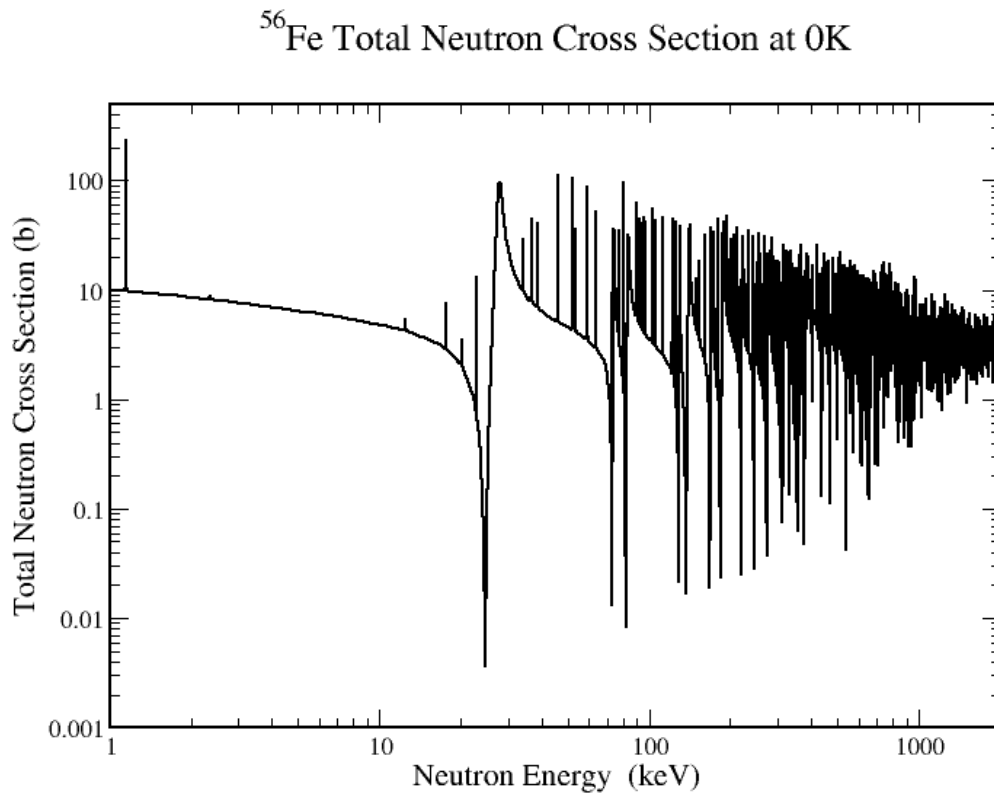


Figure 25. ^{56}Fe total neutron cross section.

^{56}Fe Neutron Capture Cross Section at 0K

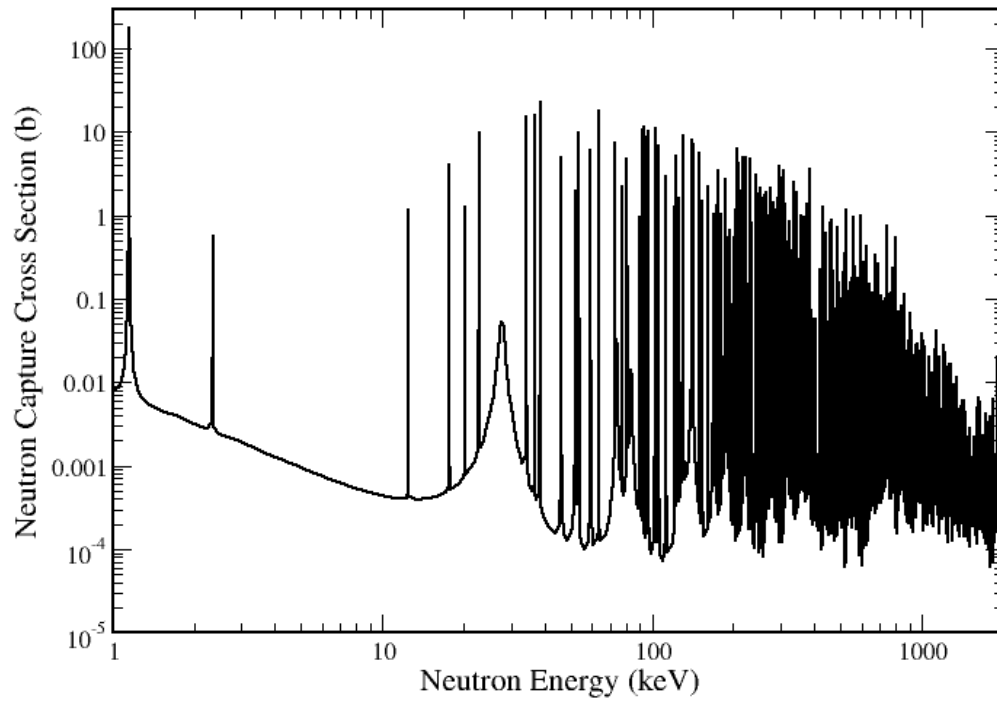


Figure 26. ^{56}Fe neutron capture cross section.

^{56}Fe Neutron Elastic Scattering Cross Section at 0K

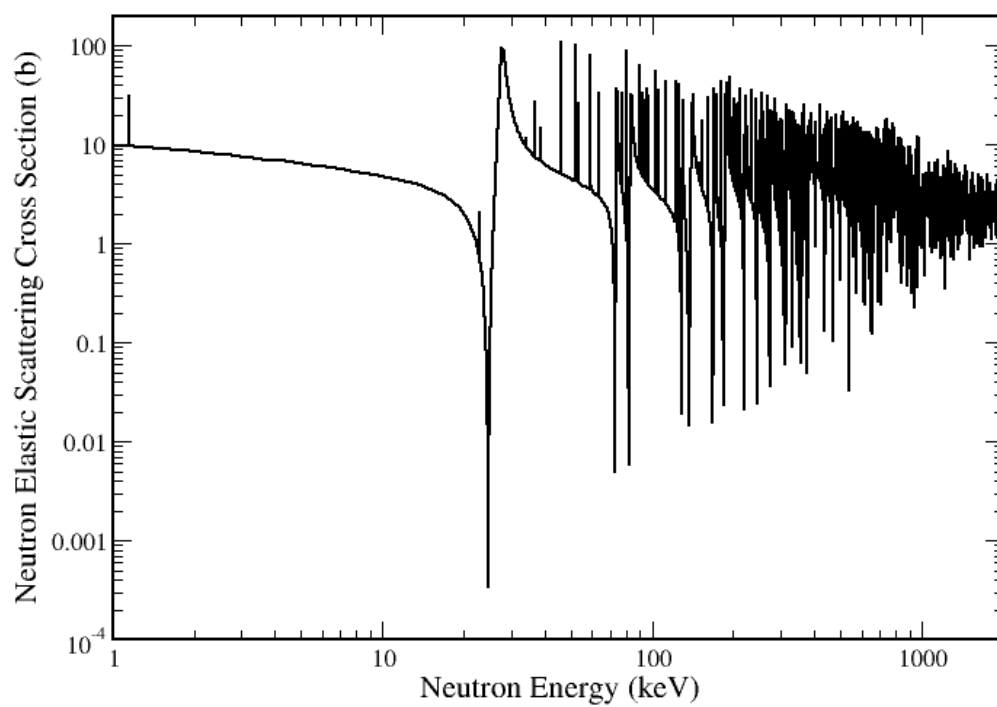


Figure 27. ^{56}Fe neutron elastic scattering cross section.

^{56}Fe Neutron Inelastic Scattering Cross Section at 0K

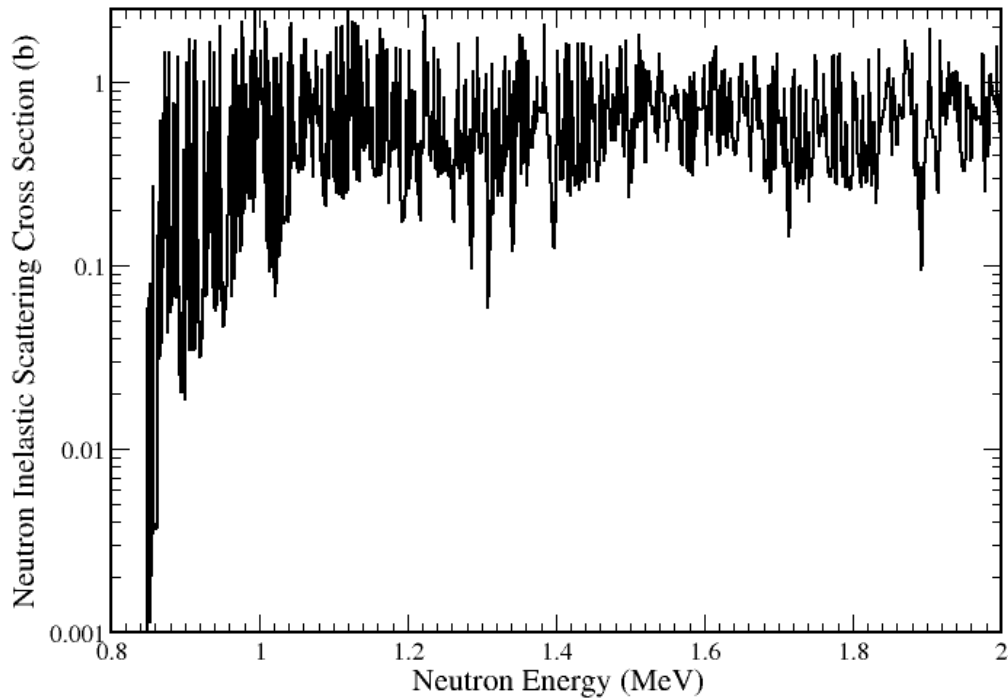


Figure 28. ^{56}Fe neutron inelastic scattering cross section.

Cu Cross Sections

The energy-differential cross sections were reconstructed for two Cu isotopes, ^{63}Cu and ^{65}Cu . While not found as prolifically as ^{56}Fe , these copper isotopes are also found in reactor environments. These isotopes are unique to the test suite in that they both have negative-parity ground state configurations. Further, neither isotope has a threshold reaction in the RRR, so that there should be no disagreement between the new algorithms results and the SAMRML results. For both ^{63}Cu and ^{65}Cu , the reconstructions were carried out over their RRRs, which both span from 10^{-5} eV to 300 keV. As expected, the reconstructions for both isotopes agreed with their respective SAMRML results to within a relative difference of 10^{-6} everywhere. The ENDF formatted resonance parameter sets

used to perform the reconstruction are not provided, as each data set spans around one thousand lines. The copper evaluations used to perform the reconstructions can be from the National Nuclear Data Center [27].

As with the other isotopes, both the ^{63}Cu and ^{65}Cu cross section reconstructions shown here omit the smoothly varying cross section in the low-energy region in order to better visualize the resonance peaks in the RRR. The ^{63}Cu total cross section is depicted in Fig. 29, the capture cross section is plotted in Fig. 30, and the elastic scattering cross section is shown in Fig. 31. The ^{65}Cu total cross section is depicted in Fig. 32, the capture cross section is plotted in Fig. 33, and the elastic scattering cross section is shown in Fig. 34.

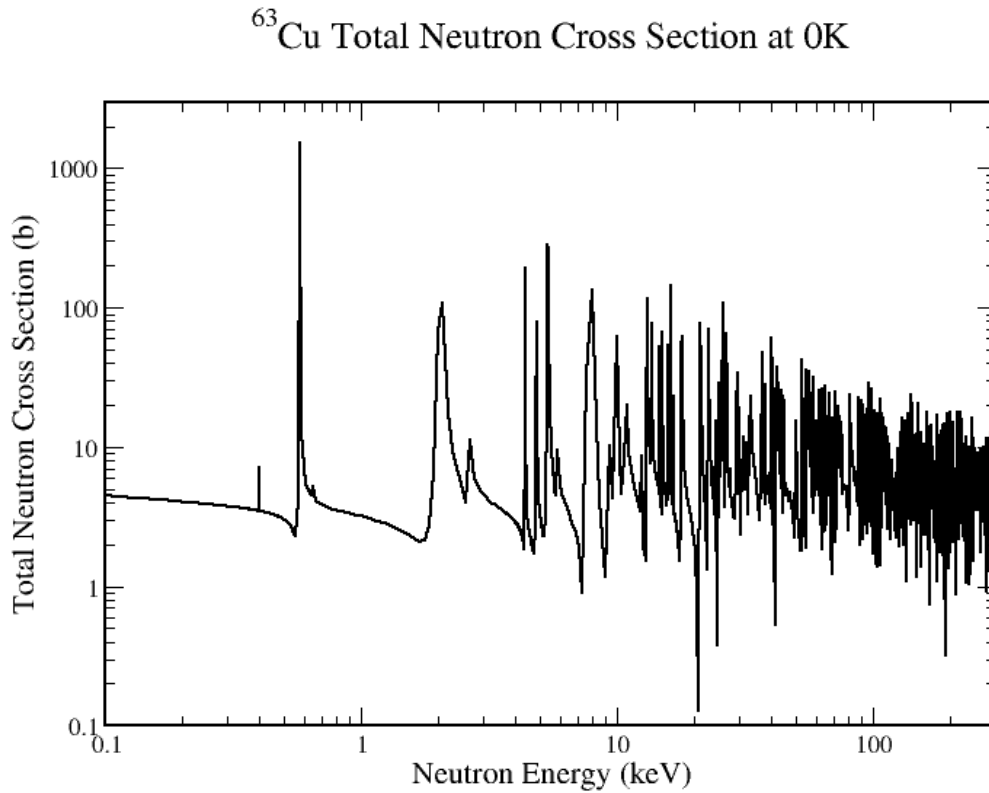


Figure 29. ^{63}Cu total neutron cross section.

^{63}Cu Neutron Capture Cross Section at 0K

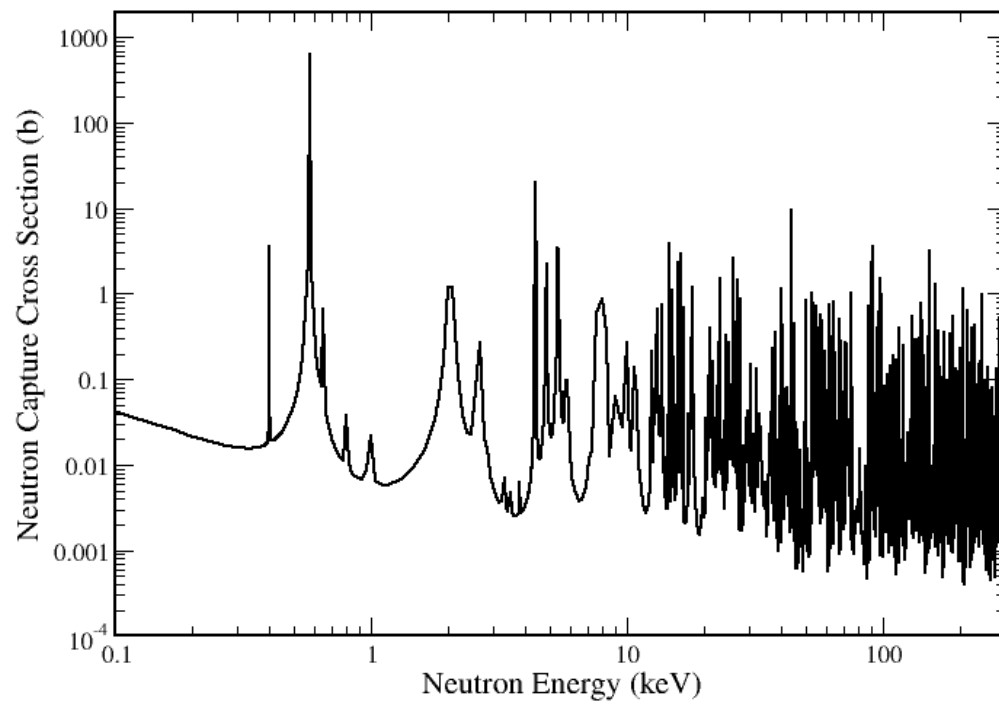


Figure 30. ^{63}Cu neutron capture cross section.

^{63}Cu Neutron Elastic Scattering Cross Section at 0K

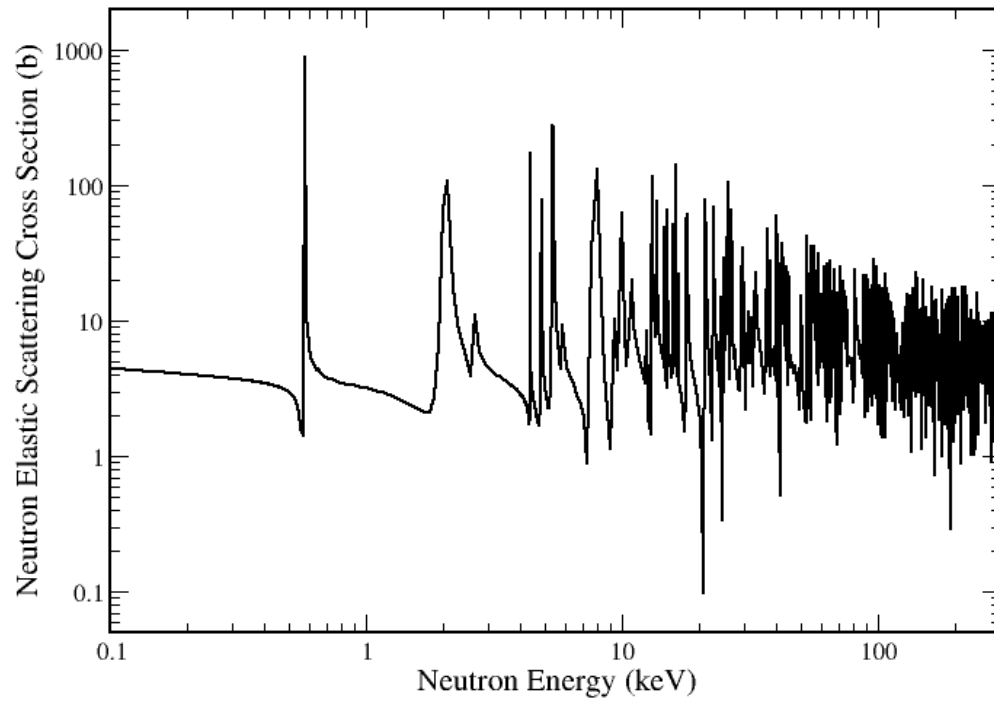


Figure 31. ^{63}Cu neutron elastic scattering cross section.

^{65}Cu Total Neutron Cross Section at 0K

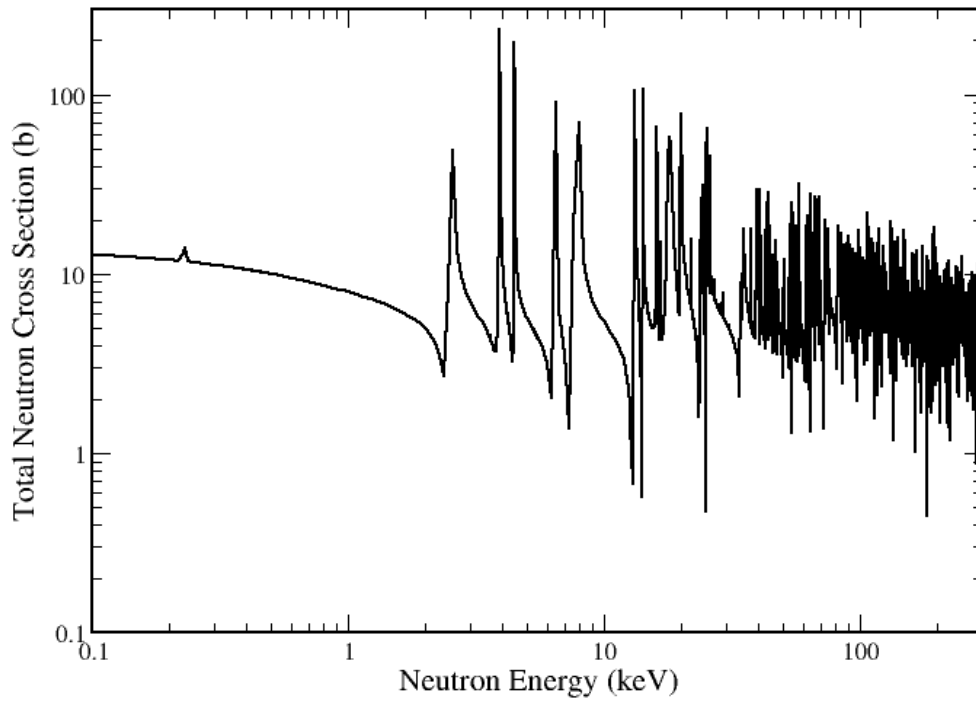


Figure 32. ^{65}Cu total neutron cross section.

^{65}Cu Neutron Capture Cross Section at 0K

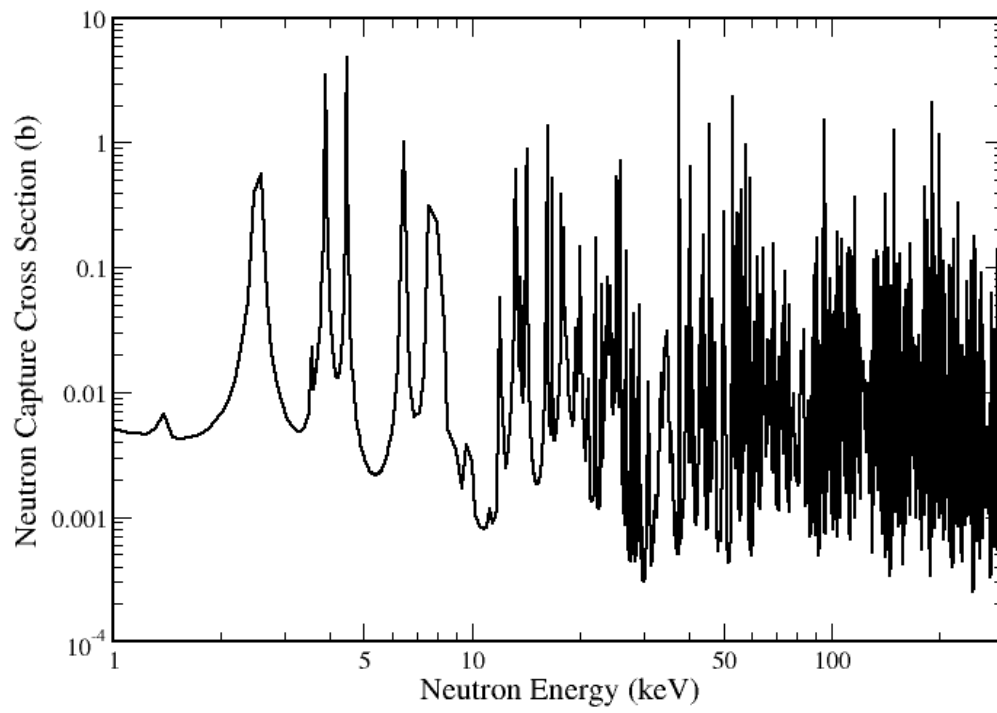


Figure 33. ^{65}Cu neutron capture cross section.

^{65}Cu Neutron Elastic Scattering Cross Section at 0K

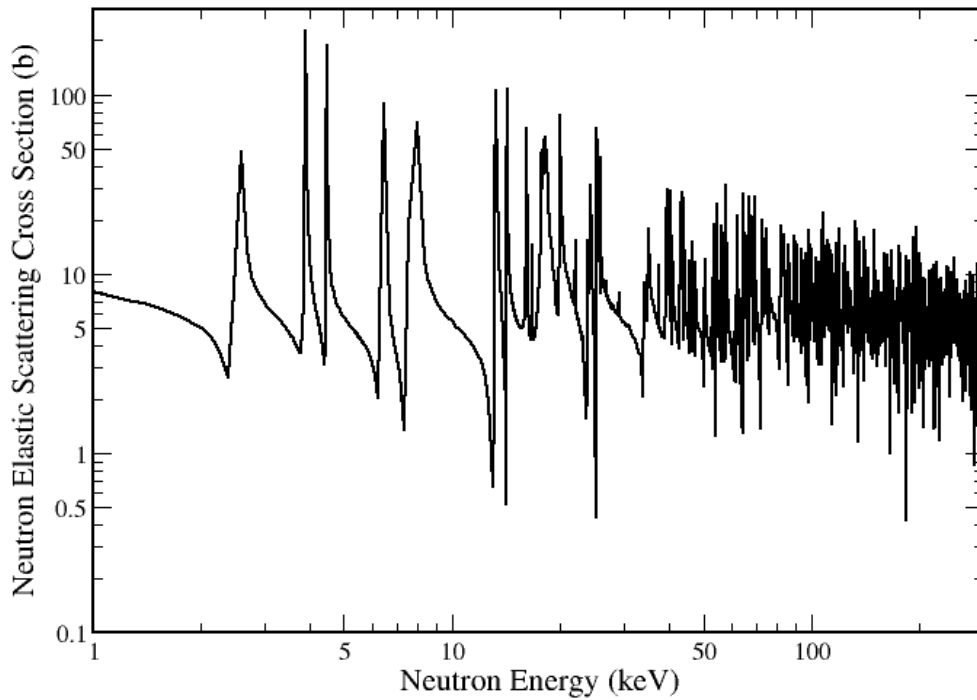


Figure 34. ^{65}Cu neutron elastic scattering cross section.

Since all of the 0K RRR energy-differential and double-differential cross-section reconstructions for ^{16}O , ^{19}F , ^{35}Cl , ^{56}Fe , ^{63}Cu , and ^{65}Cu , the new RML algorithm has been verified to work consistently and accurately for a wide-range of input parameters. Of course, as more RML evaluated data libraries become available, they will be used to further test the new algorithm implementation for any minor discrepancy.

^{238}U Unresolved Resonance Region Probability Tables

The new URR methodology was used to generate probability tables for ^{238}U using the ENDF/B-VII.1 File-2 average resonance parameters. The URR part of File-2 is given in Appendix D. The probability tables presented are normalized for each reaction, in accordance with the evaluation's self-shielding flag. As such, these probability tables represent the effective cross-section factors for ^{238}U , and are scaled by the File-3 data when used in the transport calculations. To ensure that the probability tables exhibited the correct behavior, they were compared with the results of the AMPX module PURM.

The URR for ^{238}U extends from 20 keV to just over 149 keV. PURM and the new methodology were used to calculate probability tables at the 18 energies of reference provided in the evaluation. The probability tables for PURM were all generated at 293.6 K using 60,000 histories per table. The new methodology was used to generate probability tables at 293.6 K, but using only 30,000 histories per table. This reduction in number of histories was one of practicality, as the large increase in run-time was not worth the decrease in uncertainty within each cross-section bin. Additional histories only mildly decrease the uncertainty in the most variable bins. The highest variation is always found in the minimum and maximum cross section bins, since they are used to tally the vanishingly small and wildly large fluctuations, respectively, in the sampled cross sections. However, this low number of histories is sufficient to obtain reasonable uncertainty on the cross-section bins, as the calculation is relatively well behaved.

The normalized cross-section factors calculated by PURM and the new method were found to be in good agreement. The factors computed by each code are plotted against each other for a few select energies that span different regions of ^{238}U 's URR. The new URR method's results and PURM results are shown at 30 keV, below the inelastic threshold, in Fig. 35, Fig. 36, and Fig. 37 for the total, capture, and elastic cross-section factors, respectively. Similarly, the two sets are compared at 50 keV, above the inelastic threshold, for the total, capture, elastic, and inelastic cross-section factors in

Fig. 38, Fig. 39, Fig. 40, and Fig. 41, respectively. Finally, the two sets of results are compared at 140 keV, near the upper end of the URR, with the total, capture, elastic, and inelastic cross-section factors plotted in Fig. 42, Fig. 43, Fig. 44, and Fig. 45, respectively. The error bars are shown on the total cross-section factor only; this choice will be discussed shortly. The complete set of normalized probability tables generated by the new method can be found in Appendix E.

^{238}U Normalized Total Cross-Section Factors at 30 keV and 293.6K

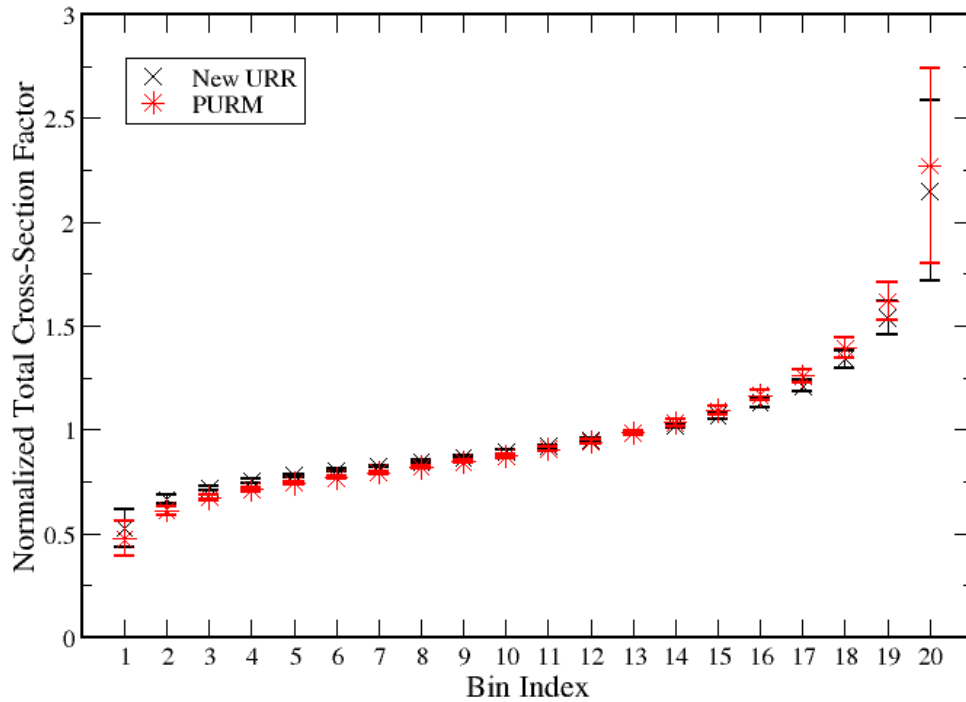


Fig. 35 Plot of the normalized total cross-section factors generated by both methods at 30 keV.

^{238}U Normalized Capture Cross-Section Factors at 30 keV and 293.6K

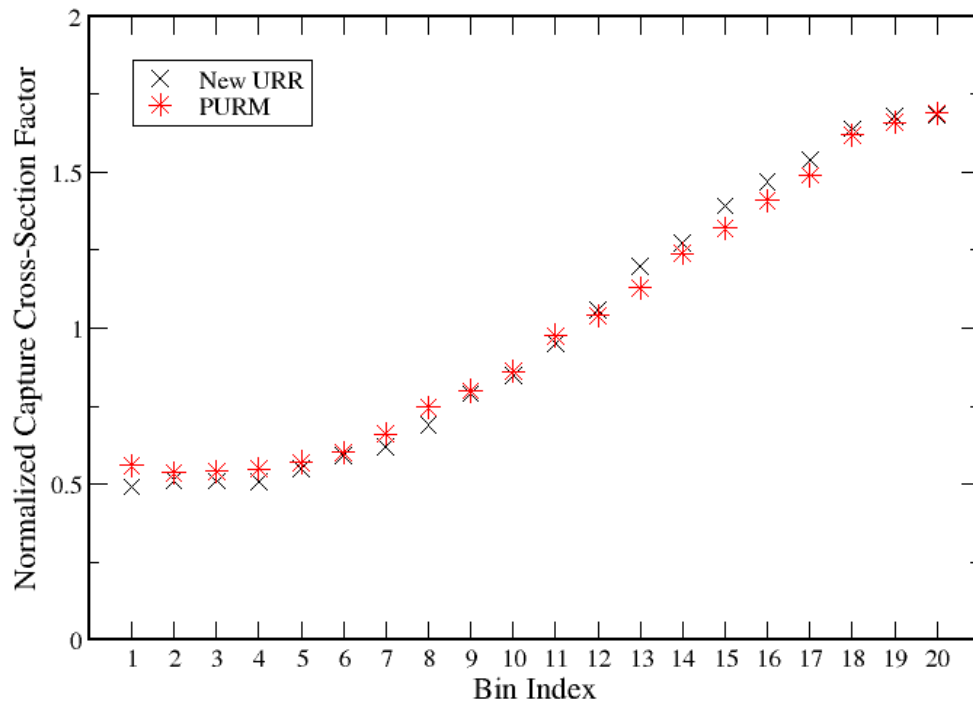


Fig. 36 Plot of the normalized capture cross-section factors generated by both methods at 30 keV.

^{238}U Normalized Elastic Cross-Section Factors at 30 keV and 293.6K

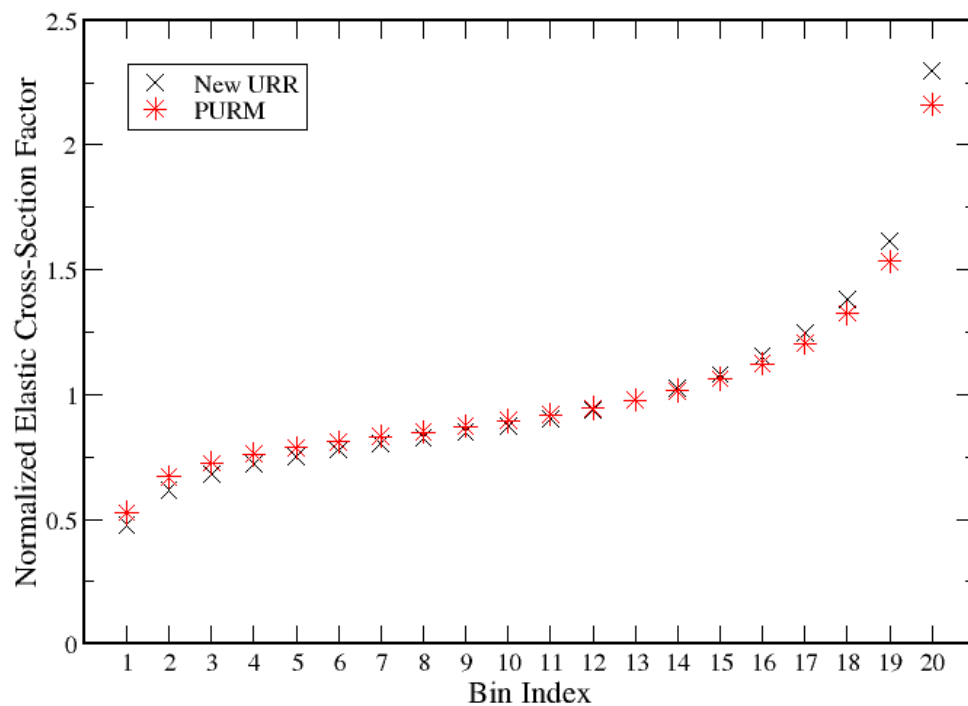


Fig. 37 Plot of the normalized elastic cross-section factors generated by both methods at 30 keV.

^{238}U Normalized Total Cross-Section Factors at 50 keV and 293.6K

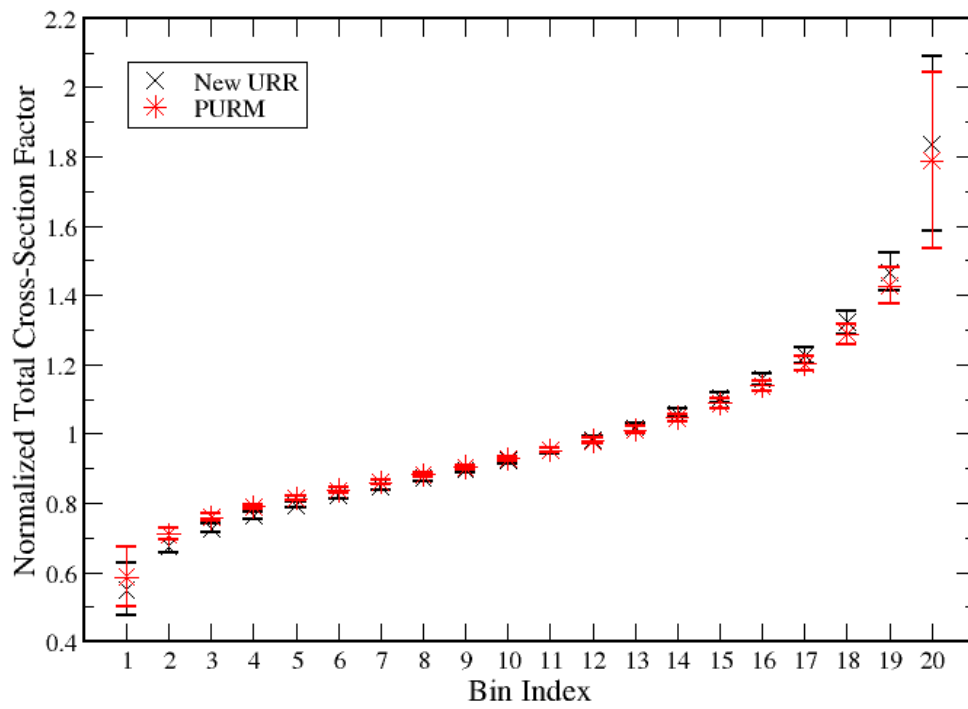


Fig. 38 Plot of the normalized total cross-section factors generated by both methods at 50 keV.

^{238}U Normalized Capture Cross-Section Factors at 50 keV and 293.6K

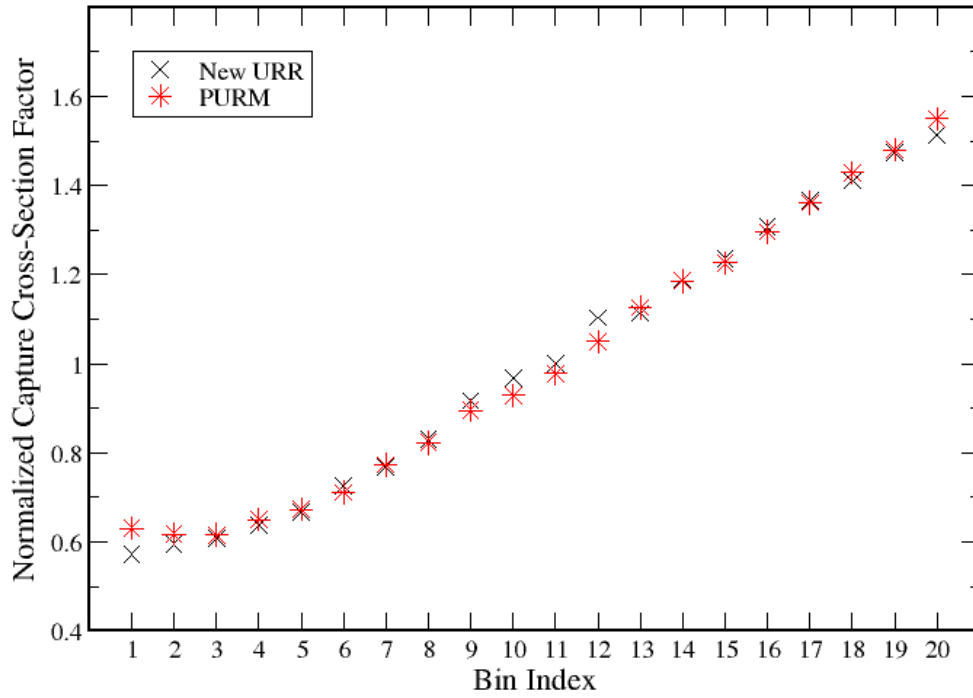


Fig. 39 Plot of the normalized capture cross-section factors generated by both methods at 50 keV.

^{238}U Normalized Elastic Cross-Section Factors at 50 keV and 293.6K

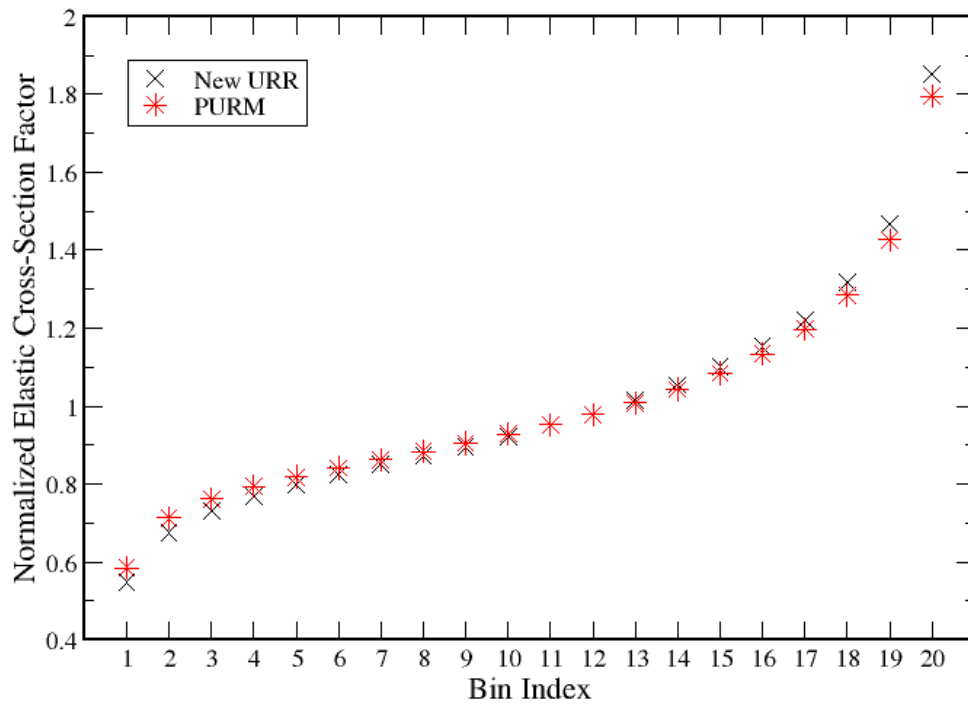


Fig. 40 Plot of the normalized elastic cross-section factors generated by both methods at 50 keV.

^{238}U Normalized Inelastic Cross-Section Factors at 50 keV and 293.6K

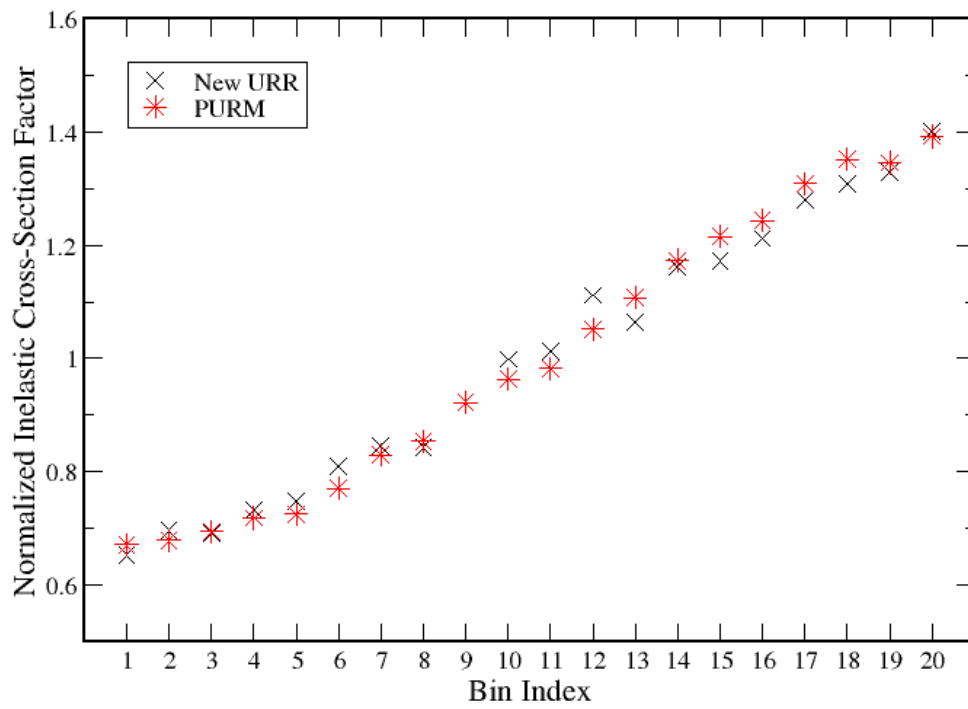


Fig. 41 Plot of the normalized inelastic cross-section factors generated by both methods at 50 keV.

^{238}U Normalized Total Cross-Section Factors at 140keV and 293.6K

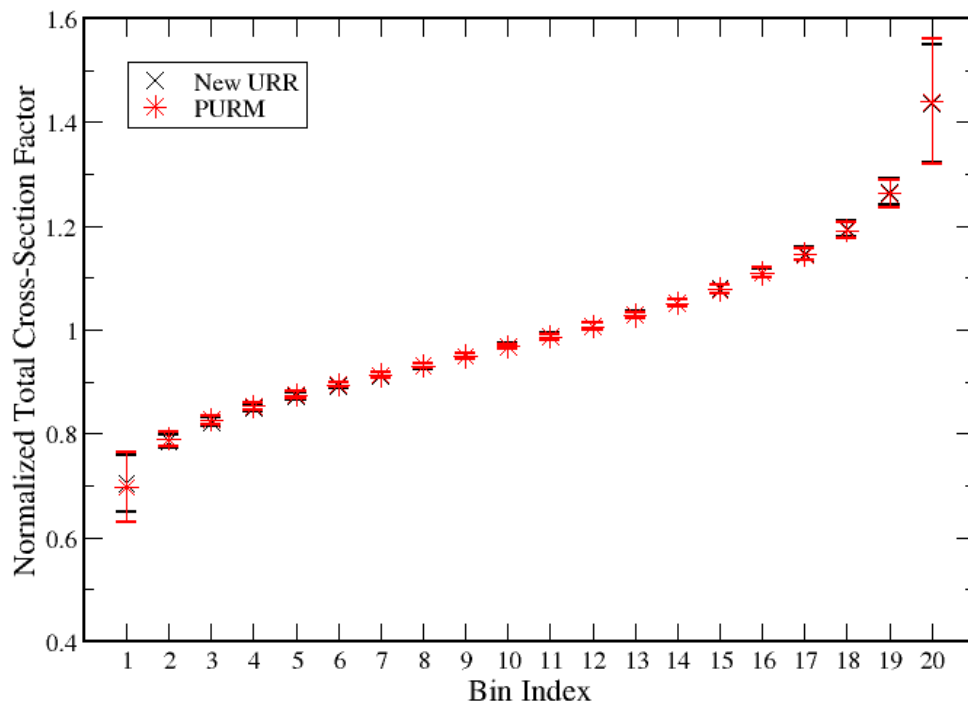


Fig. 42 Plot of the normalized total cross-section factors generated by both methods at 140 keV.

^{238}U Normalized Capture Cross-Section Factors at 140keV and 293.6K

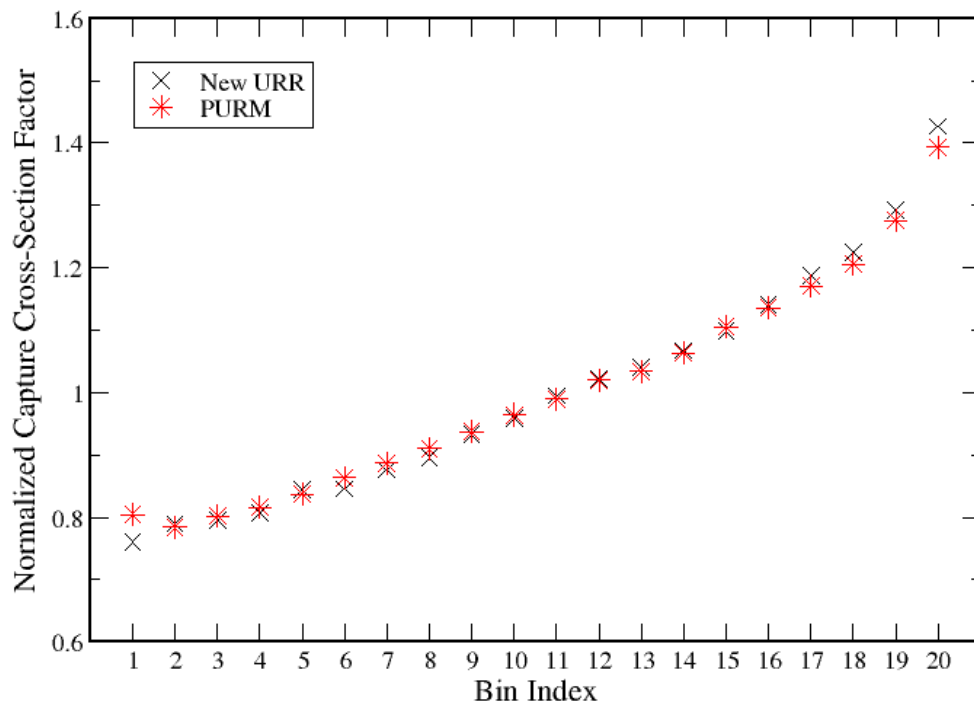


Fig. 43 Plot of the normalized capture cross-section factors generated by both methods at 140 keV.

^{238}U Normalized Elastic Cross-Section Factors at 140keV and 293.6K

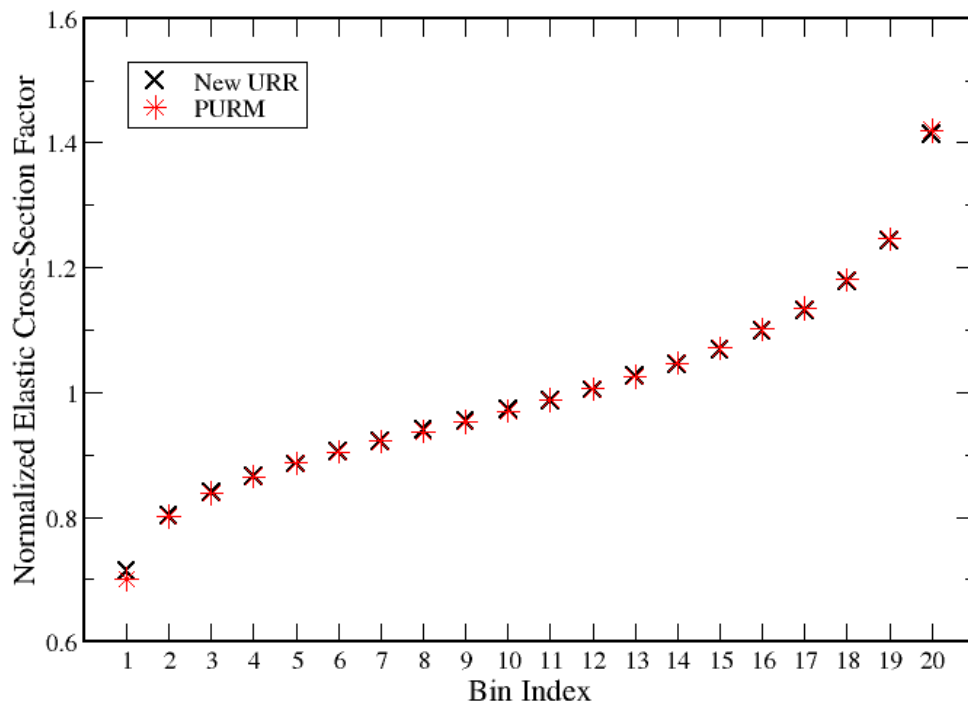


Fig. 44 Plot of the normalized elastic cross-section factors generated by both methods at 140 keV.

²³⁸U Normalized Inelastic Cross-Section Factors at 140keV and 293.6K

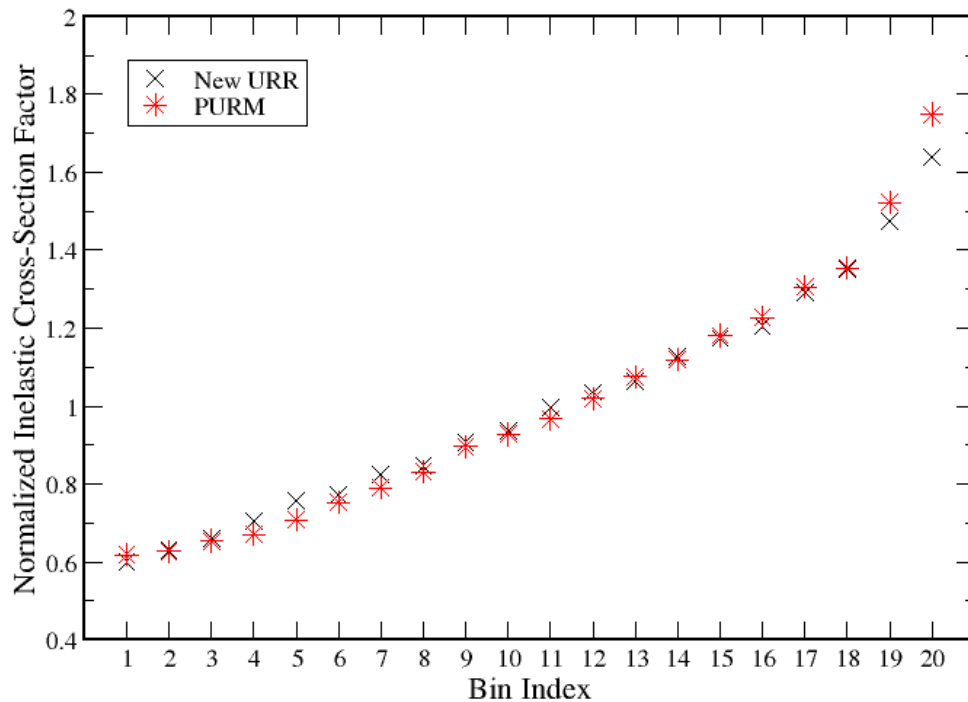


Fig. 45 Plot of the normalized inelastic cross-section factors generated by both methods at 140 keV.

As evidenced in Fig. 35-45, the two sets of cross-section factors showed good agreement, and exhibited the same trends in behavior. Further, the total cross-section factors of PURM and the new method always agreed to within one sigma of one another. Only the total cross-section factors are plotted with error bars because it is only that variation that has any significance. Since the probability tables are binned according to increasing total cross section, we must ensure that set of factors is converging.

Binning by the total cross section ensures small variation within the most dominant reaction cross section and mostly monotonically increasing cross-section factors for all reaction types. This also ensures that the distributions shown are physically

accurate. If we choose to bin by one of the individual reaction cross sections, we are biasing the importance of that reaction in relation to the calculation of the overall cross-section factor. This also explains why the probability tables are not constructed for each individual reaction and stitched together at the end. The combination of individual reaction tables would not guarantee consistency, meaning that the sum of the average individual reactions inside a bin would not be guaranteed to produce the correct average total cross section for that bin. Furthermore, the combination results in a non-physical table, as it implies that all reaction cross sections increase simultaneously, which is not guaranteed.

In addition, it is important to remember that there is no correlation between the different reaction widths. The reaction widths obey similar Chi-squared distribution laws, but there is no connection between the sampling for each reaction type. For example, let's examine a sampled resonance in which only the elastic and capture channels are open. If the sampled elastic width is very large, this will lead to a large elastic cross section around the resonance energy. However, this does not guarantee anything about the capture cross section. The capture width is sampled independently, and may also be very large, very small, or anywhere in between. This accounts for the high variability of the individual reaction widths inside each table bin.

Benchmarks

Three benchmark problems were selected from the International Handbook of Evaluated Criticality Safety Benchmark Experiments (ICSBEP) [28] to test the validity of the new URR method. The three problems investigated include the IEU-MET-FAST-007, IEU-MET-FAST-003, and IEU-COMP-FAST-004 benchmarks. The problems were chosen using the Database for the International Handbook of Evaluated Criticality Safety Benchmark Experiments (DICE) software [29]. The problems were selected based on their fast spectra and large amount of ^{238}U , so that the probability tables would have an impact on the benchmark solution. The k_{eff} sensitivity to the ^{238}U total neutron cross section for each benchmark was plotted using the DICE software, and is shown in Fig. 46. The sensitivities plotted were provided in the ICSBEP handbook, which were generated using the SCALE [30] 238-group general purpose criticality safety library and TSUNAMI-3D [31]. The sensitivity profiles plotted in Fig. 46 show that perturbations to the ^{238}U total neutron cross section in the URR will change the k_{eff} for each of the three benchmarks. In contrast, the same three benchmarks show no sensitivity to the ^{238}U total neutron cross section below approximately 1 keV due to their respective fast spectrums.



Fig. 46 k_{eff} sensitivity coefficients for the selected benchmark problems.

IEU-MET-FAST-007 Benchmark

The IEU-MET-FAST-007 benchmark is more commonly known as the BIG TEN benchmark. The BIG TEN benchmark is based on the Los Alamos Big Ten assembly, consisting of a 10% enriched ^{235}U mixed-uranium-metal cylindrical core surrounded by a ^{238}U reflector.

The benchmark setup is depicted in Fig. 47 and Fig. 48. Fig. 47 depicts an XZ planar cut through the center of the configuration, and Fig. 48 shows an XY planar cut through the axial mid-point of the setup. In both Fig. 47 and Fig. 48, the material composition of each region is identified by number and color. The benchmark material compositions and region dimensions are provided in Table 1 and Table 2, respectively, with the region identifier corresponding to the numbering scheme shown in Fig. 49, which maintains the same color shading as Fig. 47 to represent the material composition.

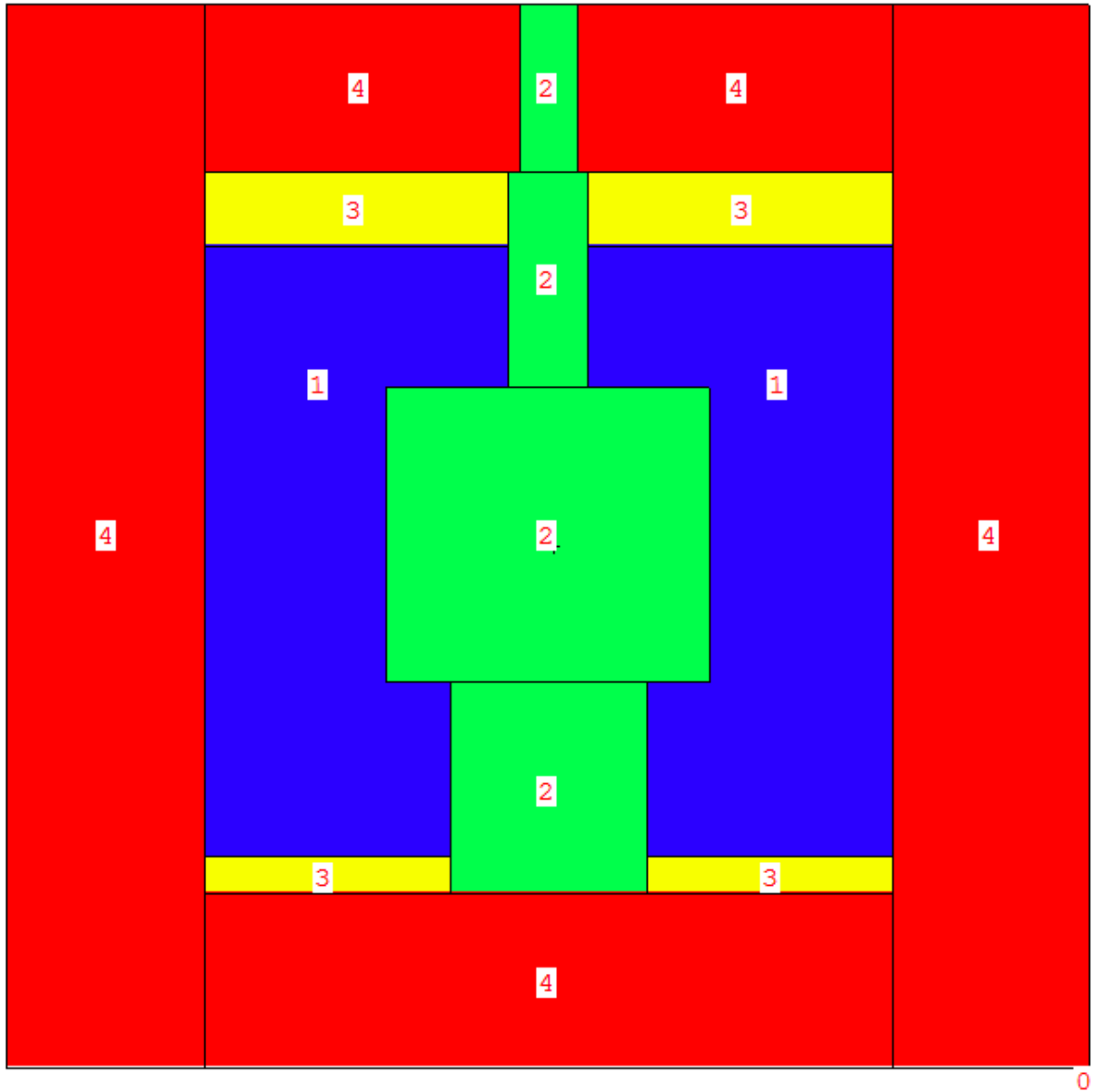


Fig. 47 XZ-view through the center of the BIG TEN benchmark configuration. The material definitions for the regions are given below in Table 1.

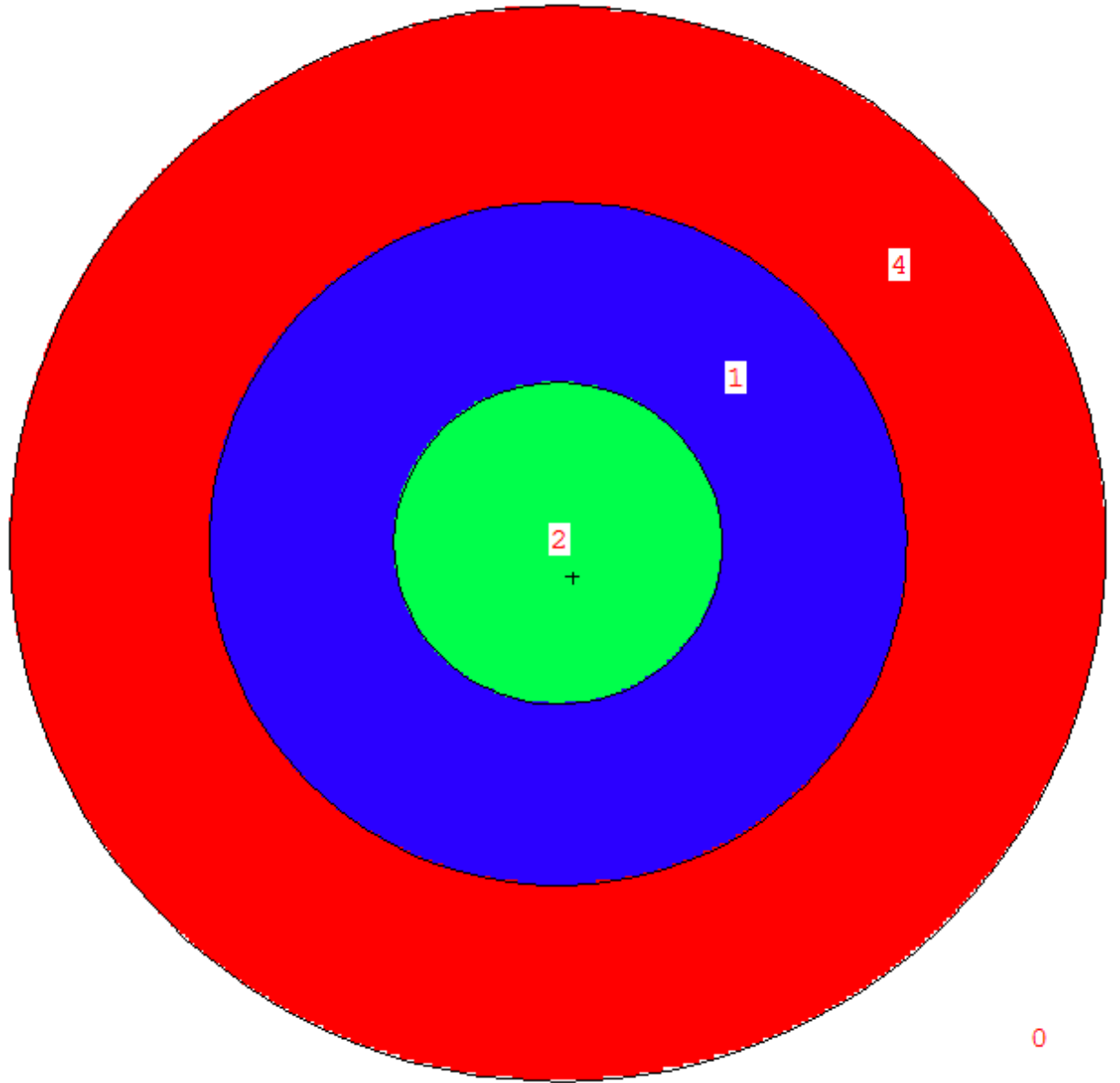


Fig. 48 XY-view through the center of the BIG TEN benchmark configuration. The material definitions for the regions are given below in Table 1.

Table 1 Material composition of the U-metal in the BIG TEN benchmark in atoms/barn-cm.

Name	Number	Color	²³⁴ U	²³⁵ U	²³⁶ U	²³⁸ U
Homogenized HEU and Natural U	1	Blue	5.4058E-5	4.9831E-3	1.3733E-5	4.3108E-2
IEU	2	Green	2.4761E-5	4.8461E-3	4.3348E-5	4.2695E-2
Natural U	3	Yellow	2.6518E-6	3.4701E-4	0	4.7846E-2
Depleted U	4	Red	2.8672E-7	1.0058E-4	1.1468E-6	4.7677E-2

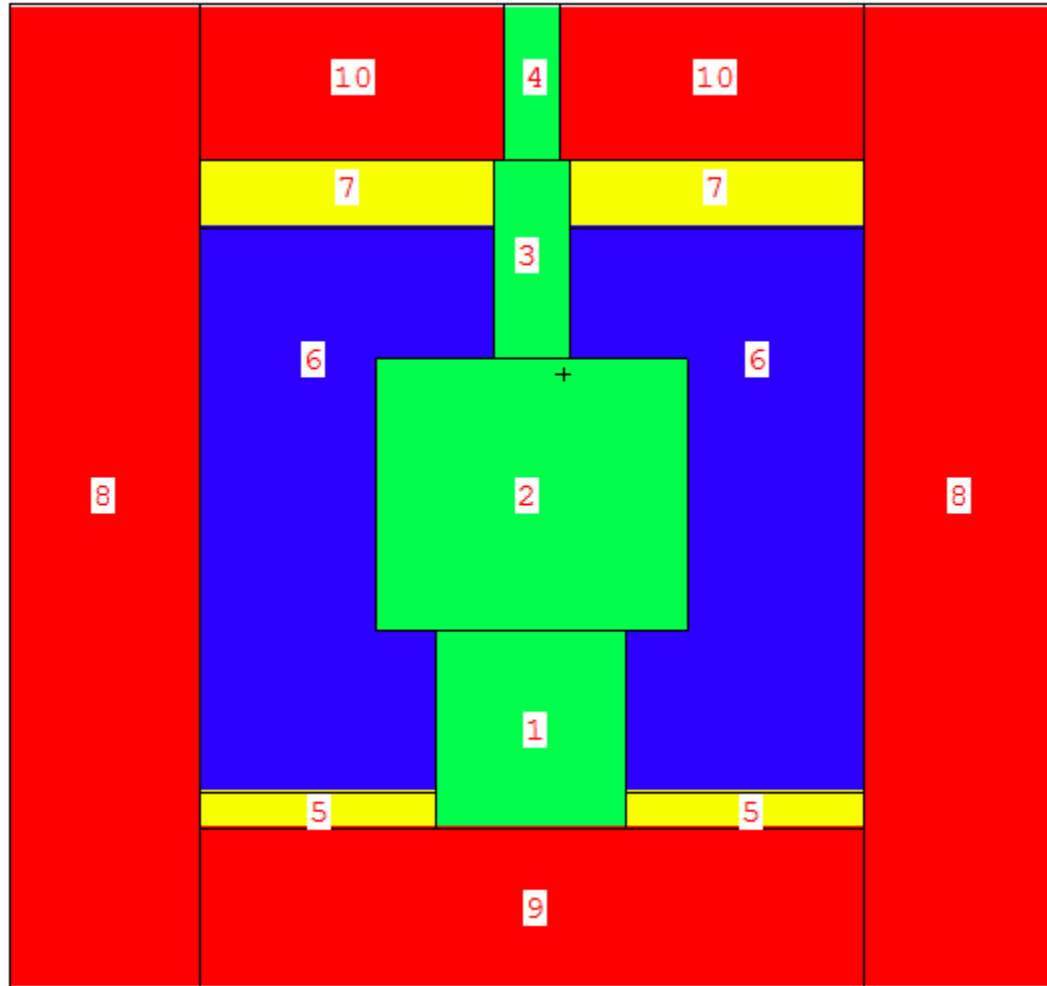


Fig. 49 XZ-view through the center of the BIG TEN benchmark configuration with labeled regions. The dimensions of each region are given below in Table 2.

Table 2 Regional dimensions and composition of the BIG TEN benchmark.

Region	Material	Outer Radius (cm)	Height (cm)
1	IEU	7.62	19.34351
2	IEU	12.54604	26.74112
3	IEU	3.10996	19.46148
4	IEU	2.25014	15.24
5	Natural U	26.67	3.48717
6	Hom. HEU + Nat. U	26.67	55.41309
7	Natural U	26.67	6.64585
8	Depleted U	41.91	96.52
9	Depleted U	26.67	15.73389
10	Depleted U	26.67	15.24

The measured system k_{eff} was found to be 1.0062 ± 0.0003 . However, the detailed benchmark does not include all of the experimental setup. Ignoring the assembly's transfer bar leads to a change in k_{eff} of -0.0011 ± 0.0003 , and ignoring the external environment led to a change in k_{eff} of -0.0006 ± 0.0003 . This means that the detailed benchmark should yield a k_{eff} of 1.0045 ± 0.0007 . Here, we look at the simplified benchmark model, which has a bias of 0.0004 ± 0.0003 relative to the benchmark model. So, the simplified benchmark model should provide a k_{eff} of 1.0049 ± 0.0008 .

The improved simplified MCNP benchmark model was used in conjunction with several sets of continuous-energy ENDF libraries to compute k_{eff} . MCNP5v1.6 was used to calculate the system k_{eff} using the MCNP continuous-energy ENDF/BVII.0 libraries. The MCNP5v1.6 calculations were carried out with the URR probability tables

turned off, as well as with them turned on. The ^{238}U URR probability tables were then replaced by the new URR probability tables, and the same two cases were run again. In addition, MCNP6.1 was used to calculate the system k_{eff} using the MCNP continuous-energy ENDF/BVII.0 libraries and ENDF/BVII.1 libraries. The MCNP6.1 runs were carried out with the URR probability tables turned off, as well as with them turned on. The MCNP ^{238}U URR probability tables were then replaced by the new URR probability tables, and the same two cases were run again. In all cases, k_{eff} was computed using a total of 50 million active histories, using 100 thousand neutron histories per generation and 500 active generations after 100 skip cycles. The results of the calculations are provided in Table 3.

Table 3. k_{eff} results for the IEU-MET-FAST-007 benchmark using the stock MCNP continuous-energy ENDF/BVII.0 libraries, ^{238}U modified ENDF/BVII.0 libraries, ENDF/BVII.0 libraries, and ^{238}U modified ENDF/BVII.0 libraries.

Library	Probability Tables	MCNP5v1.6	MCNP6.1
ENDF/BVII.0	No	1.00098 ± 0.00007	1.00098 ± 0.00007
ENDF/BVII.0	Yes	1.00492 ± 0.00008	1.00492 ± 0.00008
ENDF/BVII.0+Modified ^{238}U	No	1.00098 ± 0.00007	1.00098 ± 0.00007
ENDF/BVII.0+Modified ^{238}U	Yes	1.00537 ± 0.00007	1.00537 ± 0.00007
ENDF/BVII.1	No	1.00089 ± 0.00007	1.00089 ± 0.00007
ENDF/BVII.1	Yes	1.00453 ± 0.00007	1.00453 ± 0.00007
ENDF/BVII.1+Modified ^{238}U	No	1.00089 ± 0.00007	1.00089 ± 0.00007
ENDF/BVII.1+Modified ^{238}U	Yes	1.00531 ± 0.00007	1.00531 ± 0.00007

As expected, there was no difference between the MCNP5v1.6 and MCNP6.1 results. Since the transport simulations were identical in all cases for the same library, only the more modern MCNP6.1 was used for testing the other benchmarks. With the probability tables disabled, MCNP only uses the infinite-dilution cross-section in the

URR, so that the energy self-shielding effect is ignored completely. Without the self-shielding effect, both the ENDF/BVII.0 and ENDF/BVII.1 libraries led to an underestimate of k_{eff} by over 400 pcm, almost five sigma below the benchmark k_{eff} . With the probability tables enabled, both the ENDF/BVII.0 and ENDF/BVII.1 libraries produce a k_{eff} that is in excellent agreement with the benchmark value, falling well within one sigma of the measured value. The ^{238}U modified ENDF/BVII.0 libraries led to an overestimate of k_{eff} of approximately 40 pcm, but is still well within one sigma of the benchmark value. Similarly, the ^{238}U modified ENDF/BVII.1 libraries lead to about the same 40 pcm overestimate, but was still well within one-sigma of the benchmark k_{eff} .

To further investigate the validity of the modified ^{238}U probability tables, an estimate of the energy spectrum inside of the IEU core was generated using an F4 tally. For each library, the track-length flux estimate is plotted in Fig. 50. The error bars represent the one standard deviation uncertainty reported by MCNP.

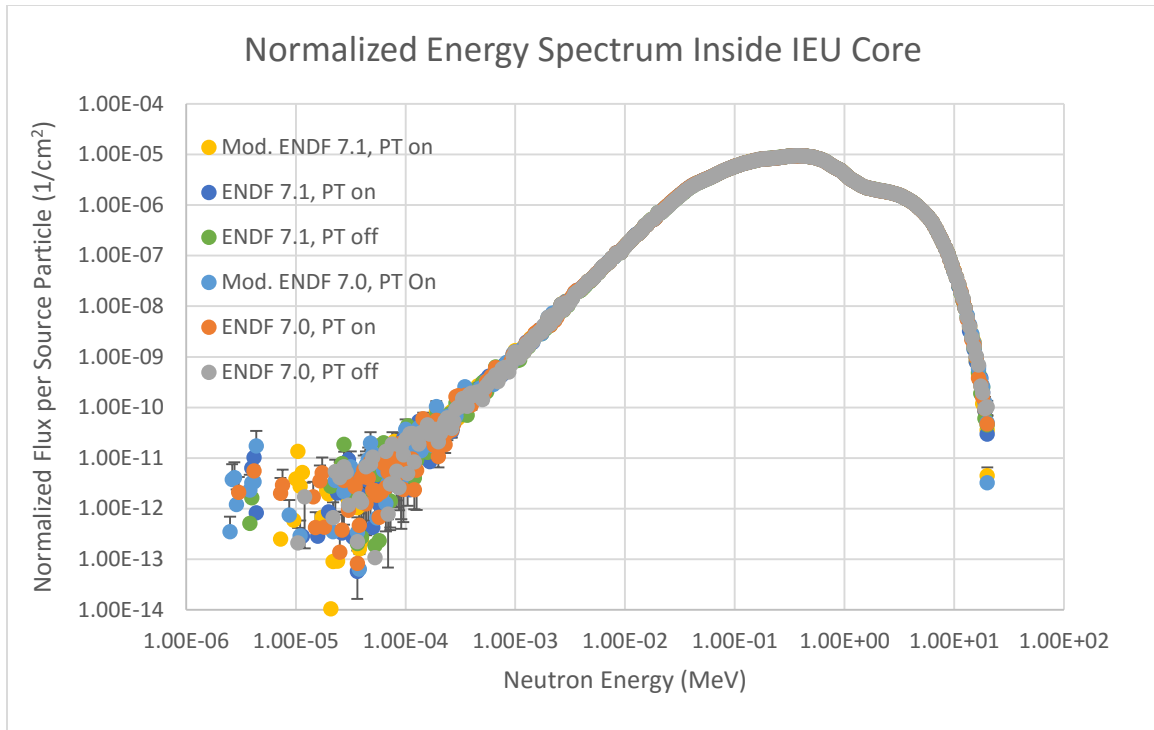


Fig. 50 Normalized flux spectrum in the central IEU core. The flux has been normalized to the total number of active source particles, or 50 million neutron histories. The error bars represent one standard deviation as reported by MCNP.

The largest variation among the flux estimates is in the lower end of the spectrum, and is due to the relatively low number of neutrons slowing down to that energy without being absorbed or lost by the system. Otherwise, the flux tallies are in very good agreement with one another, including the estimates using the updated probability tables for ^{238}U . As such, it can be concluded that the new ^{238}U probability tables provide an accurate representation of the energy self-shielding effect for the Big Ten benchmark problem.

IEU-MET-FAST-003 Benchmark

The IEU-MET-FAST-003 benchmark is based on a bare spherical assembly of approximately 36 wt% ^{235}U assembled at VNIIEF's critical test facility. The core consists of 10 concentric spheres of uranium metal, each with an enrichment of between 36.30 and 36.61 wt% ^{235}U . All uranium metal was coated in a protective 50- μm coating composed of 50 wt% Cu and 50 wt% Ni. The main impurities in the composition of the uranium pieces were C, Fe, and W, and are included in the benchmark definition. The actual configuration was simplified in the benchmark by homogenizing over each spherical shell. A plane-view of the benchmark through the center of the configuration is presented in Fig. 51. The region dimensions are presented in Table 4. The material definitions for the regions are given in Table 5.

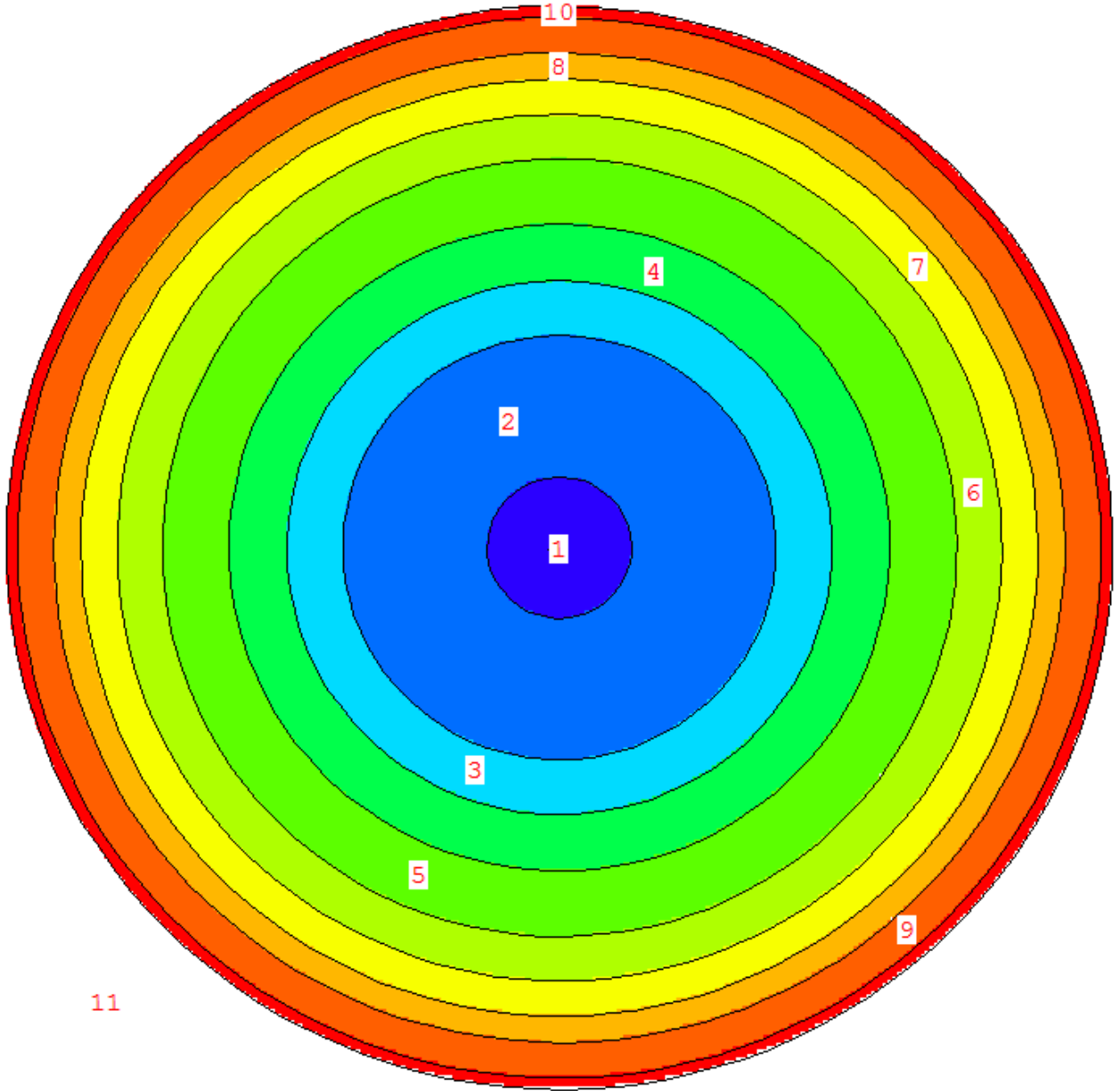


Fig. 51 Plane-view through the center of the IEU-MET-FAST-003 benchmark configuration. The material definitions and dimensions for the regions are given below.

Table 4. Regional dimensions of the IEU-MET-FAST-003 benchmark.

Region	Outer Rad. (cm)
1	2.000
2	6.000
3	7.550
4	9.150
5	11.00
6	12.25
7	13.25
8	14.00
9	15.00
10	15.324

Table 5. Material definitions of the IEU-MET-FAST-003 benchmark. Compositions are given in units of atoms/barn-cm.

Region	²³⁴ U	²³⁵ U	²³⁸ U	C	Fe	Ni	Cu	W
1	1.2743E-4	1.7093E-2	2.9308E-2	5.5181E-4	2.5713E-4	1.3191E-3	1.2183E-3	6.0083E-6
2	1.5814E-4	1.7321E-2	2.9785E-2	4.6687E-4	1.6066E-4	1.7665E-4	1.6315E-4	1.7665E-4
3	1.5677E-4	1.7194E-2	2.9508E-2	3.7026E-4	1.5926E-4	2.9710E-4	2.7440E-4	2.9710E-4
4	1.5581E-4	1.7174E-2	2.9235E-2	5.5201E-4	1.5829E-4	2.2621E-4	2.0893E-4	2.2621E-4
5	1.3256E-4	1.7141E-2	2.9417E-2	7.3802E-4	1.1904E-4	2.1030E-4	1.9423E-4	2.1030E-4
6	1.6004E-4	1.7121E-2	2.9159E-2	5.5031E-4	9.8630E-5	3.6459E-4	3.3673E-4	3.6459E-4
7	1.7235E-4	1.6958E-2	2.8806E-2	9.0767E-4	9.7607E-5	3.8907E-4	3.5934E-4	3.8907E-4
8	1.4729E-4	1.6779E-2	2.8482E-2	6.2781E-4	9.6445E-5	4.2215E-4	3.8989E-4	4.2215E-4
9	1.4996E-4	1.7018E-2	2.9013E-2	1.3697E-3	1.3748E-4	4.3479E-4	4.0157E-4	4.3479E-4
10	1.3891E-4	1.6796E-2	2.8748E-2	6.3157E-4	7.7618E-5	1.5579E-3	1.4389E-3	1.5579E-3

The measured k_{eff} value for the bare spherical assembly was reported to be 1.0000 ± 0.0017 . The MCNP benchmark model was used in conjunction with several sets of continuous-energy ENDF libraries to compute k_{eff} . MCNP6.1 was used to calculate the system k_{eff} using the MCNP continuous-energy ENDF/BVII.1 libraries. The calculation was carried out with the URR probability tables turned off, as well as with them turned on. The ²³⁸U URR probability tables were then replaced by the new URR probability tables, and the same two cases were run again. In all cases, k_{eff} was computed using a total of 50 million active histories, using 100 thousand neutron histories per generation and 500 active generations after 100 skip cycles. The results of the calculations are provided in Table 6.

Table 6. k_{eff} results for the IEU-MET-FAST-003 benchmark using the stock MCNP continuous-energy ENDF/BVII.1 libraries and the ^{238}U modified library.

Library	Probability Tables	k_{eff}
ENDF/BVII.1	No	1.00266 ± 0.00009
ENDF/BVII.1	Yes	1.00222 ± 0.00009
ENDF/BVII.1+Modified ^{238}U	No	1.00266 ± 0.00009
ENDF/BVII.1+Modified ^{238}U	Yes	1.00204 ± 0.00009

As expected, the k_{eff} values calculated without the probability tables agree for both the original and modified library set. This indicates that the data library was not edited erroneously, as the rest of the MCNP library data would have been in the wrong place, leading to a different value of k_{eff} . With or without the probability tables, the MCNP ENDF/BVII.1 continuous-energy libraries produce a k_{eff} that over-estimates the measured k_{eff} by over 200 pcm. The modified ^{238}U library produces a k_{eff} closer to the benchmark k_{eff} , but also leads to an approximately 200 pcm overestimate. In all cases, the calculated k_{eff} was found to be within two sigma of the actual value. This is another confirmation that the new ^{238}U probability tables are valid. As with the other benchmark problems, the IEU-MET-FAST-003 benchmark was chosen for its known sensitivity to perturbations to the ^{238}U cross section probability tables, due to its fast spectrum. If the tables were not physically accurate, the calculated k_{eff} would not be accurate, due to the benchmark's known sensitivity to perturbations in the ^{238}U cross section.

IEU-COMP-FAST-004 Benchmark

The IEU-COMP-FAST-004 benchmark is based on the ZPR-3 Assembly 12. The system was designed as an intermediate enrichment uranium compound system with a fast neutron spectrum. The core was composed of highly enriched uranium plates, graphite plates, and depleted uranium plates in stainless steel drawers that were inserted into a 31v31 steel tube matrix on a split-table machine. This configuration is prohibitively difficult to present as a benchmark problem, and so the benchmark presents a simplified cylindrical model. The ZPR-3 Assembly 12 is approximated as a cylindrical assembly composed of highly enriched uranium, depleted uranium, and graphite, with an average ^{235}U enrichment of 21 at%. The cylindrical geometry attempts to approximate the square matrix loading and corresponding radial blanket. An XZ-view of the benchmark configuration is presented in Fig. 52. The corresponding XY-view of the benchmark is given in Fig. 53. The region dimensions are presented in Table 7. The material definitions for the regions are given in Table 8. The orange regions represent the steel-drawer gaps, with the space between region 7 and region 3 corresponding to region 5, and the space between region 2 and region 6 corresponding to region 4. The unmarked matrix radial blankets above and below region 8 correspond to region 10 and region 9, respectively.

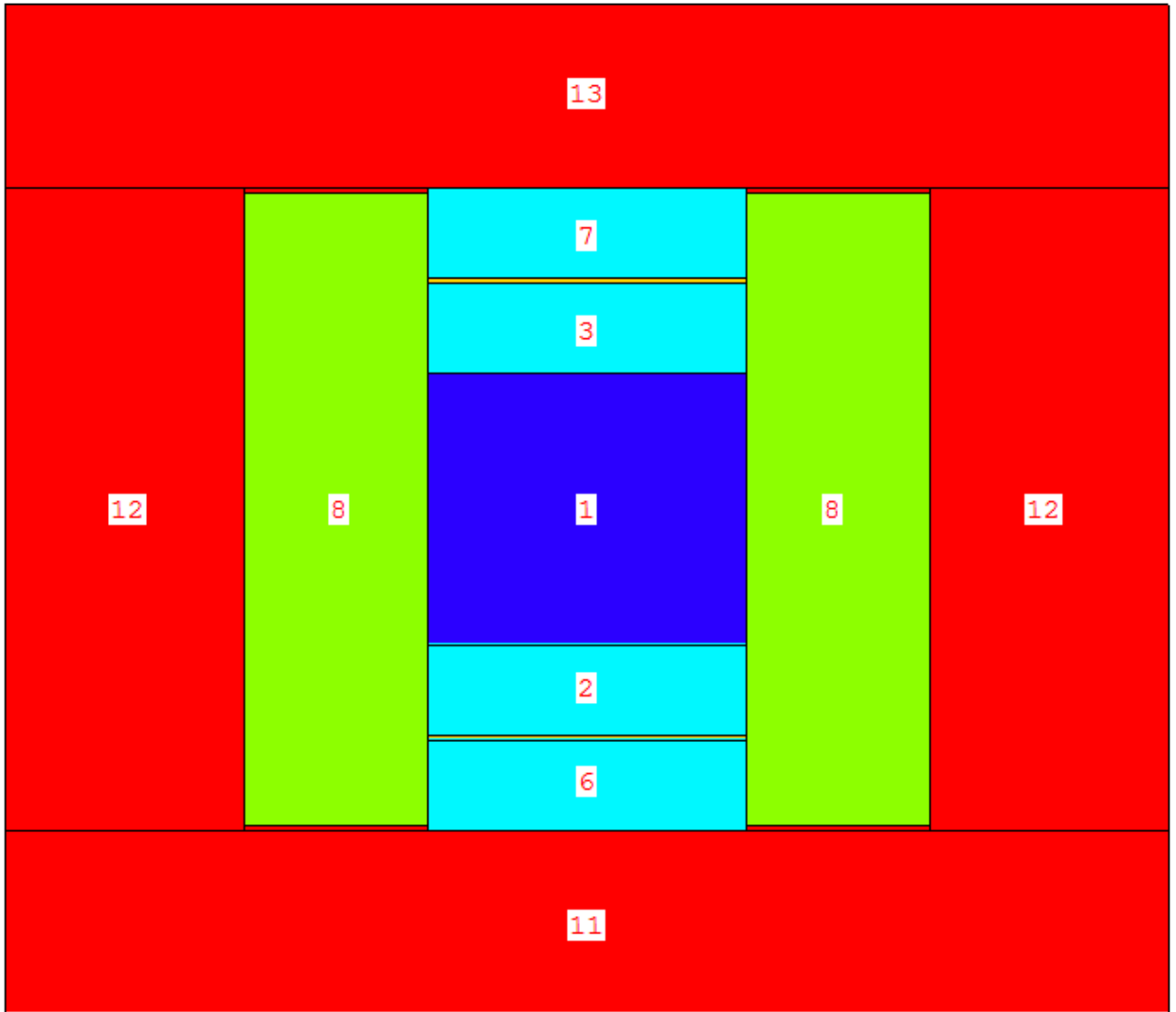


Fig. 52 XZ-view through the center of the IEU-COMP-FAST-004 benchmark configuration. The material definitions for the regions are given below in Table 8.

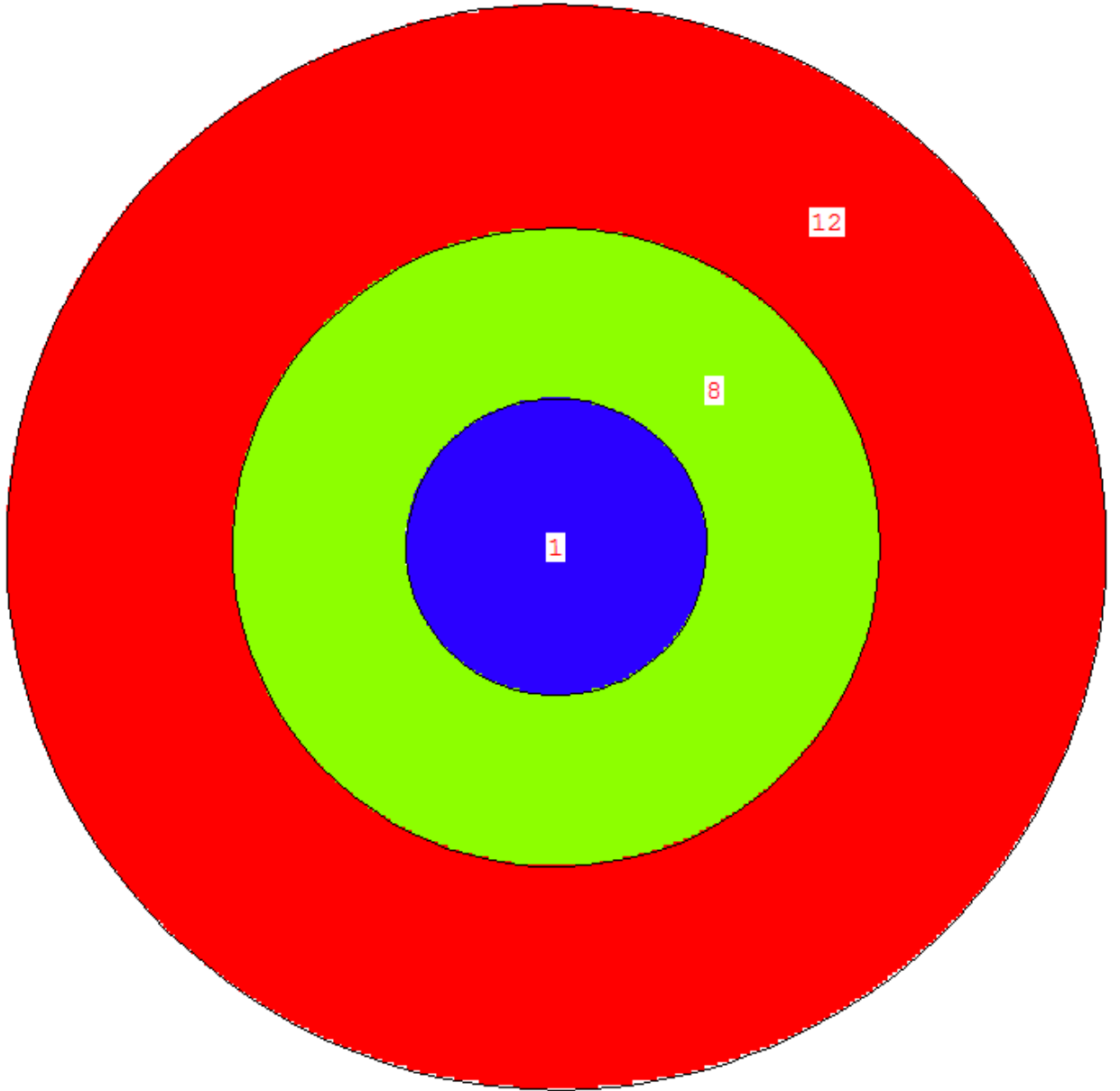


Fig. 53 XY-view through the center of the IEU-COMP-FAST-004 benchmark configuration. The material definitions for the regions are given below in Table 8.

Table 7. Regional dimensions and material names of the IEU-COMP-FAST-004 benchmark.

Region	Material	Color	Outer Rad. (cm)	Height (cm)
1	Core	Blue	26.50215	45.88854
2	Axial Blanket	Aqua	26.50215	15.2382
3	Axial Blanket	Aqua	26.50215	15.2382
4	Drawer Gap	Orange	26.50215	0.70515
5	Drawer Gap	Orange	26.50215	0.70515
6	Axial Blanket	Aqua	26.50215	15.24
7	Axial Blanket	Aqua	26.50215	15.24
8	Radial Blanket	Green	56.99622	106.68
9	Matrix	Red	96.82557	0.78762
10	Matrix	Red	96.82557	0.78762
11	Matrix	Red	96.82557	30.96238
12	Matrix	Red	96.82557	108.25524
13	Matrix	Red	96.82557	30.96238

Table 8. Material definitions of the IEU-COMP-FAST-004 benchmark. Compositions are given in units of atoms/barn-cm.

Nuclide	Core	Axial Blanket	Radial Blanket	Drawer Gap	Matrix
¹ H	9.54448E-06	3.79787E-06	2.51175E-06	0	0
Nat. C	2.67827E-02	1.30847E-05	8.68037E-06	2.70467E-04	0
¹⁹ F	4.87032E-05	1.94349E-05	1.28937E-05	0	0
Nat. Si	7.29440E-05	7.43652E-05	6.07202E-05	1.50384E-04	6.07700E-05
Nat. Cl	1.64505E-05	6.56345E-06	4.35411E-06	0	0
Nat. Cr	1.44259E-03	1.45915E-03	1.11160E-03	3.52543E-03	1.10960E-03
⁵⁵ Mn	7.21394E-05	7.14660E-05	4.39839E-05	2.38485E-04	4.34957E-05
Nat. Fe	5.78763E-03	5.86383E-03	4.53519E-03	1.95621E-02	4.52968E-03
Nat. Ni	6.19051E-04	6.23327E-04	4.55145E-04	1.64142E-03	4.53554E-04
Nat. Cu	0	0	0	3.66070E-07	0
Nat. Mo	0	0	0	6.06674E-08	0
²³⁴ U	4.40100E-05	0	0	0	0
²³⁵ U	4.53763E-03	8.04895E-05	8.12089E-05	0	0
²³⁶ U	2.10981E-05	0	0	0	0
²³⁸ U	1.68116E-02	3.95918E-02	4.00011E-02	0	0
Total	5.626610E-02	4.780729E-02	4.631738E-02	2.53887E-02	6.197096E-03

The experimental k_{eff} value measured for the ZPR-3/12 was found to be 1.0013 \pm 0.0011. However, the modeling will not account for some features of the real experiment, and so it must be adjusted accordingly. In the benchmark modeling, the neglect of room return was estimated to require an adjustment of -0.0061 ± 0.0031 % Δ k. The interface gap was also ignored in the model, so an additional correction of $+0.0450 \pm 0.0116$ % Δ k is needed. Further, any impurities in the HEU fuel were ignored, introducing another $+0.0334 \pm 0.0167$ % Δ k correction. The benchmark applies a correction for the temperature used in the data libraries, leading to an additional -0.0217 ± 0.0021 % Δ k

correction to the measured k_{eff} value. This leads to an adjusted experimental k_{eff} of 1.0018 ± 0.0011 . When converting from the as-built model to the benchmark model, an additional transformation bias of $-0.0040 \pm 0.0004 \Delta k$ was incurred. Therefore, if the libraries are at a temperature of 300 K, an accurate set of cross section data should produce a k_{eff} of 0.9978 ± 0.0015 . If the libraries are at the appropriate temperature of 293.6 K, then the model should produce a k_{eff} of 0.9982 ± 0.0015 .

The MCNP benchmark model was used in conjunction with several sets of continuous-energy ENDF libraries to compute k_{eff} . MCNP6.1 was used to calculate the system k_{eff} using the MCNP continuous-energy ENDF/BVII.1 libraries. The calculation was carried out with the URR probability tables turned off, as well as with them turned on. The ^{238}U URR probability tables were then replaced by the new URR probability tables, and the same two cases were run again. In all cases, k_{eff} was computed using a total of 50 million active histories, using 100 thousand neutron histories per generation and 500 active generations after 100 skip cycles. The results of the calculations are provided in Table 9.

Table 9. k_{eff} results for the IEU-COMP-FAST-004 benchmark using the stock MCNP continuous-energy ENDF/BVII.1 libraries and the ^{238}U modified library.

Library	Probability Tables	k_{eff}
ENDF/BVII.1	No	0.99833 ± 0.00008
ENDF/BVII.1	Yes	0.99995 ± 0.00009
ENDF/BVII.1+Modified ^{238}U	No	0.99833 ± 0.00008
ENDF/BVII.1+Modified ^{238}U	Yes	1.00052 ± 0.00008

As expected, the k_{eff} values calculated without the probability tables agree for both the original and modified library data set. With or without the probability tables, the MCNP ENDF/BVII.1 continuous-energy libraries produce a k_{eff} that is in very good agreement with the benchmark. The modified ^{238}U library slightly overestimates k_{eff} , but falls within two-sigma of the adjusted benchmark value and is much closer to the actual measured value. The k_{eff} estimated using the modified libraries is not as good as the original library set, but is still proof that the method is sound. Furthermore, it would have been effectively impossible to improve on the original library results, since they produce almost the exact benchmark k_{eff} .

CHAPTER 5

CONCLUSIONS AND FUTURE WORK

A new URR methodology consistent with the RRR methodology has been developed for generating normalized cross-section factor probability tables. The RML cross section reconstruction algorithm has been rigorously tested for a variety of isotopes, including ^{16}O , ^{19}F , ^{35}Cl , ^{56}Fe , ^{63}Cu , and ^{65}Cu . The new URR method also produced normalized cross-section factor probability tables for ^{238}U that were found to be in agreement with current standards. The modified ^{238}U probability tables were shown to produce k_{eff} results in excellent agreement with several standard benchmarks, including the IEU-MET-FAST-007, IEU-MET-FAST-003, and IEU-COMP-FAST-004 benchmarks.

The new method has been shown to generate data that is in good agreement with experimental measurement and modeling. While the new method is slow in comparison to codes such as PURM, it provides the most accurate representation of the underlying reaction physics. Furthermore, the new method allows for any reaction to be handled explicitly, removing the channel restrictions imposed by the SLBW resonance formulae.

Although the program run-time is long in comparison to PURM, the method readily lends itself to parallelization, as each history, table, and isotope can be processed independently. In the future, the method can be greatly accelerated by utilizing parallel programming techniques. Even without parallelization, the method produces excellent results in manageable time. On a related note, changing the reference energies of the probability tables could potentially have an impact on the transport calculation, and is well worth further investigation. Lastly, this method should be applied to other isotopes and criticality safety benchmarks to further validate the methodology.

APPENDIX A

¹⁶O ENDF/B-VII.1 RESOLVED FILE2 LRF=7 DATA

8.016000+3	1.585751+1	0	0	1	0	825	2151	1
8.016000+3	1.000000+0	0	0	1	0	825	2151	2
1.000000-5	6.120000+6	1	7	0	1	825	2151	3
0.000000+0	0.000000+0	0	3	9	0	825	2151	4
0.000000+0	0.000000+0	3	0	36	6	825	2151	5
0.000000+0	1.685750+1	0.000000+0	0.000000+0	1.000000+0	0.000000+0	825	2151	6
0.000000+0	0.000000+0	0.000000+0	1.020000+2	0.000000+0	0.000000+0	825	2151	7
1.000000+0	1.585750+1	0.000000+0	0.000000+0	5.000000-1	0.000000+0	825	2151	8
0.000000+0	1.000000+0	0.000000+0	2.000000+0	0.000000+0	1.000000+0	825	2151	9
3.967131321	1.289164+1	2.0	6.0	0.000000+0	-5.000000-1	825	2151	10
-2213760.00	1.0	0.0	800.0	1.000000+0	0.000000+0	825	2151	11
0.5	0.0	0	0	18	3	825	2151	12
1.0	0.0	0.0	0.0			825	2151	13
2.0	0.0	0.5	0.0	3.818860-1	3.818860-1	825	2151	14
3.0	1.0	-0.5	0.0	6.683904-1	6.683904-1	825	2151	15
0.0	0.0	0	5	30	5	825	2151	16
-12055269.4	2.500000-1	1.867704+7				825	2151	17
-4472609.55	2.500000-1	2.833297+6				825	2151	18
2377270.881	2.500000-1	1.619406+5				825	2151	19
4060821.279	2.500000-1	1.114238+5	3.482406+3			825	2151	20
4467364.095	2.500000-1	1.565648+4	2.116526+3			825	2151	21
-0.5	0.0	0	0	18	3	825	2151	22
1.0	0.0	0.0	0.0			825	2151	23
2.0	1.0	0.5	0.0	3.818860-1	3.818860-1	825	2151	24
3.0	0.0	-0.5	0.0	6.683904-1	6.683904-1	825	2151	25
0.0	0.0	0	8	48	8	825	2151	26
1901438.585	2.500000-1	3.350000+4				825	2151	27
3989637.669	2.500000-1	2.827930+5	1.319806+4			825	2151	28
4311698.003	2.500000-1	4.386251+4	-3.756971+2			825	2151	29
5311000.000	2.500000-1	5.000000+2	4.372238+2			825	2151	30
6087440.629	2.500000-1	1.603700+4	1.123783+3			825	2151	31
7294222.518	2.500000-1	2.616100+4	5.386500+3			825	2151	32
7373310.000	2.500000-1	1.888000+3				825	2151	33
19026724.30	2.500000-1	2.575500+7				825	2151	34
-1.5	0.0	0	0	18	3	825	2151	35
1.0	0.0	0.0	0.0			825	2151	36
2.0	1.0	0.5	0.0	3.818860-1	3.818860-1	825	2151	37
3.0	2.0	-0.5	0.0	6.683904-1	6.683904-1	825	2151	38
0.0	0.0	0	8	48	8	825	2151	39
434249.0558	2.700000+0	4.473562+4				825	2151	40
1309379.557	2.500000-1	4.342500+4				825	2151	41
3511914.839	2.500000-1	6.652788+5	1.812584+1			825	2151	42
4302785.470	2.500000-1	5.703854+4	3.973876+3			825	2151	43
4819635.371	2.500000-1	6.355638+4	1.727816+3			825	2151	44
5574468.588	2.500000-1	1.893205+5	2.859376+2			825	2151	45
5993285.780	2.500000-1	1.437878+4	-7.283726+1			825	2151	46
11131716.09	2.500000-1	1.511500+7				825	2151	47
1.5	0.0	0	0	18	3	825	2151	48
1.0	0.0	0.0	0.0			825	2151	49
2.0	2.0	0.5	0.0	3.818860-1	3.818860-1	825	2151	50
3.0	1.0	-0.5	0.0	6.683904-1	6.683904-1	825	2151	51
0.0	0.0	0	7	42	7	825	2151	52
1000218.949	2.500000-1	1.003600+5				825	2151	53
1834093.375	2.500000-1	7.790000+3				825	2151	54
3291011.612	2.500000-1	3.453894+5	1.168524+2			825	2151	55
4180041.069	2.500000-1	9.540039+4	6.477292+3			825	2151	56
5066004.980	2.500000-1	9.950365+4	-2.470613+4			825	2151	57
6578034.747	2.500000-1	9.064100+4	8.793900+4			825	2151	58
17223847.17	2.500000-1	7.723600+5				825	2151	59

2.5	0.0	0	0	18	3	825	2151	60
1.0	0.0	0.0	0.0			825	2151	61
2.0	2.0	0.5	0.0	3.818860-1	3.818860-1	825	2151	62
3.0	3.0	-0.5	0.0	6.683904-1	6.683904-1	825	2151	63
0.0	0.0	0	7	42	7	825	2151	64
2888700.000	2.500000-1	2.200000+2				825	2151	65
3438800.000	2.500000-1	6.000000+2	1.170348+1			825	2151	66
4527358.546	2.500000-1	5.056413+3	5.854492+2			825	2151	67
5369270.000	2.500000-1	2.770764+3	6.287871+2			825	2151	68
6207948.599	2.500000-1	4.974900+3	1.029610+5			825	2151	69
6786116.690	2.500000-1	1.056500+4	2.325400+5			825	2151	70
7198369.565	2.500000-1	7.856900+3	1.969800+4			825	2151	71
-2.5	0.0	0	0	18	3	825	2151	72
1.0	0.0	0.0	0.0			825	2151	73
2.0	3.0	0.5	0.0	3.818860-1	3.818860-1	825	2151	74
3.0	2.0	-0.5	0.0	6.683904-1	6.683904-1	825	2151	75
0.0	0.0	0	6	36	6	825	2151	76
1689100.000	2.500000-1	2.700000+2				825	2151	77
3211756.828	2.500000-1	1.500000+3	5.018373+0			825	2151	78
3441550.000	2.500000-1	1.300000+3	6.476247+0			825	2151	79
4631214.797	2.500000-1	3.101029+3	3.567687+3			825	2151	80
5672622.372	2.500000-1	3.343549+2	1.247573+4			825	2151	81
6672725.668	2.500000-1	1.864800+3	1.905800+4			825	2151	82
-3.5	0.0	0	0	18	3	825	2151	83
1.0	0.0	0.0	0.0			825	2151	84
2.0	3.0	0.5	0.0	3.818860-1	3.818860-1	825	2151	85
3.0	4.0	-0.5	0.0	6.683904-1	6.683904-1	825	2151	86
0.0	0.0	0	7	42	7	825	2151	87
1651379.850	2.500000-1	4.099900+3				825	2151	88
3006900.000	2.500000-1	1.600000+2				825	2151	89
3767000.206	2.500000-1	1.847053+4	1.496208+1			825	2151	90
5123951.742	2.500000-1	2.256482+4	1.653438+3			825	2151	91
6400262.487	2.500000-1	2.653500+4	2.937800+4			825	2151	92
6815174.115	2.500000-1	1.893700+4	2.836100+4			825	2151	93
7168675.223	2.500000-1	1.296900+5	2.238500+5			825	2151	94
3.5	0.0	0	0	18	3	825	2151	95
1.0	0.0	0.0	0.0			825	2151	96
2.0	4.0	0.5	0.0	3.818860-1	3.818860-1	825	2151	97
3.0	3.0	-0.5	0.0	6.683904-1	6.683904-1	825	2151	98
0.0	0.0	0	3	18	3	825	2151	99
4594830.593	2.500000-1	1.430607+3	2.655982+2			825	2151	100
5918633.085	2.500000-1	2.049301+4	2.635296+3			825	2151	101
6332235.524	2.500000-1	3.403200+3	1.814800+5			825	2151	102
4.5	0.0	0	0	18	3	825	2151	103
1.0	0.0	0.0	0.0			825	2151	104
2.0	4.0	0.5	0.0	3.818860-1	3.818860-1	825	2151	105
3.0	5.0	-0.5	0.0	6.683904-1	6.683904-1	825	2151	106
0.0	0.0	0	1	6	1	825	2151	107
6076189.054	2.500000-1	3.125800+3	2.640086+3			825	2151	108
0.0	0.0	0	0	0	0	825	2 0	109
0.000000+0	0.000000+0	0	0	0	0	825	0 0	0

APPENDIX B

¹⁹F ENDF/B-VII.1 RESOLVED FILE2 LRF=7 DATA

9.019000+3	1.883519+1	0	0	1	0	925	2151	1
9.019000+3	1.000000+0	0	0	1	0	925	2151	2
1.000000-5	1.000000+6	1	7	0	1	925	2151	3
0.000000+0	0.000000+0	0	3	9	0	925	2151	4
0.000000+0	0.000000+0	4	0	48	8	925	2151	5
0.000000+0	1.967320+1	0.000000+0	0.000000+0	1.000000+0	0.000000+0	925	2151	6
0.000000+0	0.000000+0	0.000000+0	1.020000+2	0.000000+0	0.000000+0	925	2151	7
1.000000+0	1.867320+1	0.000000+0	0.000000+0	5.000000-1	5.000000-1	925	2151	8
0.000000+0	1.000000+0	0.000000+0	2.000000+0	0.000000+0	0.000000+0	925	2151	9
1.000000+0	1.867320+1	0.000000+0	0.000000+0	5.000000-1	-5.000000-1	925	2151	10
-104308.024	1.000000+0	0.000000+0	5.100000+1	0.000000+0	0.000000+0	925	2151	11
1.000000+0	1.867320+1	0.000000+0	0.000000+0	5.000000-1	2.500000+0	925	2151	12
-187122.107	1.000000+0	0.000000+0	5.200000+1	0.000000+0	0.000000+0	925	2151	13
0.0	-1.0	0	0	24	4	925	2151	14
1.0	0.0	0.0	0.0			925	2151	15
2.0	1.0	1.0	0.0	5.360000-1	5.360000-1	925	2151	16
3.0	0.0	0.0	0.0	5.360000-1	5.360000-1	925	2151	17
4.0	3.0	3.0	0.0	5.360000-1	5.360000-1	925	2151	18
0.0	0.0	0	0	6	1	925	2151	19
						925	2151	20
0.0	1.0	0	0	24	4	925	2151	21
1.0	0.0	0.0	0.0			925	2151	22
2.0	0.0	0.0	0.0	5.360000-1	5.360000-1	925	2151	23
3.0	1.0	-1.0	0.0	5.360000-1	5.360000-1	925	2151	24
4.0	2.0	2.0	0.0	5.360000-1	5.360000-1	925	2151	25
0.0	0.0	0	1	6	1	925	2151	26
-338314.102	3.434419+0	1.139378+5				925	2151	27
-1.0	0.0	0	0	48	8	925	2151	28
1.0	0.0	0.0	0.0			925	2151	29
2.0	1.0	0.0	0.0	5.360000-1	5.360000-1	925	2151	30
2.0	1.0	1.0	0.0	5.360000-1	5.360000-1	925	2151	31
3.0	0.0	-1.0	0.0	5.360000-1	5.360000-1	925	2151	32
3.0	2.0	-1.0	0.0	5.360000-1	5.360000-1	925	2151	33
4.0	1.0	2.0	0.0	5.360000-1	5.360000-1	925	2151	34
4.0	3.0	2.0	0.0	5.360000-1	5.360000-1	925	2151	35
4.0	3.0	3.0	0.0	5.360000-1	5.360000-1	925	2151	36
0.0	0.0	0	5	60	10	925	2151	37
48931.02889	8.740337-1	1.716010+3	1.135764-1			925	2151	38
						925	2151	39
97944.56930	2.745850+0	1.392614+4	1.631873-1			925	2151	40
						925	2151	41
142255.9168	1.222463-1	9.110728-1	2.472564+0	2.040036+2	2.016355+2	925	2151	42
						925	2151	43
257029.4263	2.508899-1	2.777787-1	5.378464-1	1.032188+3	1.006169+0	925	2151	44
3.230381+5	5.633774-1	1.022091+0				925	2151	45
499900.2874	1.499168+1	3.516910+3	2.165961+3	6.909181-1	7.199141-1	925	2151	46
-1.055654+1	-1.863695+4	3.976764+1				925	2151	47
1.0	0.0	0	0	42	7	925	2151	48
1.0	0.0	0.0	0.0			925	2151	49
2.0	0.0	1.0	0.0	5.360000-1	5.360000-1	925	2151	50
2.0	2.0	1.0	0.0	5.360000-1	5.360000-1	925	2151	51
3.0	1.0	0.0	0.0	5.360000-1	5.360000-1	925	2151	52
3.0	1.0	-1.0	0.0	5.360000-1	5.360000-1	925	2151	53
4.0	2.0	2.0	0.0	5.360000-1	5.360000-1	925	2151	54
4.0	2.0	3.0	0.0	5.360000-1	5.360000-1	925	2151	55
0.0	0.0	0	4	48	8	925	2151	56
268109.3783	2.798728+0	1.021239+4	5.952071-1	2.178182+3	9.911879-1	925	2151	57
5.534664-3	6.653301-1					925	2151	58
308537.0571	3.288641-1	8.750079+0	1.269503+2	4.942975-1	6.206843+0	925	2151	59
2.134796+0	1.051100+0					925	2151	60
924708.9783	2.674594+0	8.767287-1	4.929213+3	1.147845+4	5.878870+0	925	2151	61
1.217647+4	2.466714+0					925	2151	62
1086723.031	5.000339-1	1.574332+5	9.592090+0	4.287647+0	1.315505+0	925	2151	63
4.608453+1	1.311353+0					925	2151	64

-2.0	0.0	0	0	54	9	925	2151	65
1.0	0.0	0.0	0.0			925	2151	66
2.0	1.0	1.0	0.0	5.360000-1	5.360000-1	925	2151	67
2.0	3.0	1.0	0.0	5.360000-1	5.360000-1	925	2151	68
3.0	2.0	0.0	0.0	5.360000-1	5.360000-1	925	2151	69
3.0	2.0	-1.0	0.0	5.360000-1	5.360000-1	925	2151	70
4.0	1.0	2.0	0.0	5.360000-1	5.360000-1	925	2151	71
4.0	1.0	3.0	0.0	5.360000-1	5.360000-1	925	2151	72
4.0	3.0	2.0	0.0	5.360000-1	5.360000-1	925	2151	73
4.0	3.0	3.0	0.0	5.360000-1	5.360000-1	925	2151	74
0.0	0.0	0	5	60	10	925	2151	75
27013.36468	1.180838+0	3.578689+2	1.318737-1			925	2151	76
						925	2151	77
261219.8416	1.929891-2	3.487118+4	2.616701+1	4.917424+4	1.171118+0	925	2151	78
-1.332360+3	1.470115-2	4.887534+0	-3.200373+2			925	2151	79
282455.3714	2.882460-2	4.916675+2	1.669338+0	6.956900+1	1.084358+0	925	2151	80
1.333155+3	1.005689+0	9.752835-1	1.408644+0			925	2151	81
406237.9402	2.207291+1	1.008361+4	1.056383+5	-1.257640+5	1.088666+2	925	2151	82
6.785298+4	2.395779+2	1.137851+1	-1.155040+5			925	2151	83
500000.8476	2.194213-1	1.312012+3	4.381843+2	1.641697+4	-1.355926+1	925	2151	84
1.487973+2	1.197182+1	1.079637+1	-4.841286-1			925	2151	85
2.0	0.0	0	0	48	8	925	2151	86
1.0	0.0	0.0	0.0			925	2151	87
2.0	2.0	0.0	0.0	5.360000-1	5.360000-1	925	2151	88
2.0	2.0	1.0	0.0	5.360000-1	5.360000-1	925	2151	89
3.0	1.0	-1.0	0.0	5.360000-1	5.360000-1	925	2151	90
3.0	3.0	-1.0	0.0	5.360000-1	5.360000-1	925	2151	91
4.0	0.0	2.0	0.0	5.360000-1	5.360000-1	925	2151	92
4.0	2.0	2.0	0.0	5.360000-1	5.360000-1	925	2151	93
4.0	2.0	3.0	0.0	5.360000-1	5.360000-1	925	2151	94
0.0	0.0	0	8	96	16	925	2151	95
120390.7616	2.715753+0	2.334148-1	1.147243-1	9.338380+0	9.179429+0	925	2151	96
						925	2151	97
421833.2568	1.122651+0	6.421688+3	9.612643+1	-2.214596+0	4.285061+0	925	2151	98
-1.624505+3	-4.263168-1	6.390789+1				925	2151	99
598371.3232	6.763298+0	6.557088+3	1.580413+1	1.306849+3	1.167360+0	925	2151	100
-5.011364+1	1.576587+3	4.140967+2				925	2151	101
655088.8482	2.900718+0	4.670726-1	6.724291+0	4.648717+2	2.983391+1	925	2151	102
1.178865+2	1.871398+1	3.939161+0				925	2151	103
752171.3717	2.366799+1	9.786653+3	3.247674+1	1.758118+3	9.958003-1	925	2151	104
1.824308+4	2.910312+0	3.768341+2				925	2151	105
792797.2467	2.598882+0	2.076687+4	2.974091+1	3.621110+4	2.962892+1	925	2151	106
-1.349886+0	3.902804+0	5.339213+1				925	2151	107
846287.5857	7.274603-1	1.816969-2	3.388886+1	5.993785+3	2.428413+1	925	2151	108
1.612453+4	1.532142+1	9.729308+0				925	2151	109
856548.3236	5.196694-1	2.409666+3	5.108495+3	3.200869+3	9.444181+0	925	2151	110
1.639930+3	4.273990-1	1.008817+0				925	2151	111
-3.0	0.0	0	0	48	8	925	2151	112
1.0	0.0	0.0	0.0			925	2151	113
2.0	3.0	0.0	0.0	5.360000-1	5.360000-1	925	2151	114
2.0	3.0	1.0	0.0	5.360000-1	5.360000-1	925	2151	115
3.0	2.0	-1.0	0.0	5.360000-1	5.360000-1	925	2151	116
4.0	1.0	2.0	0.0	5.360000-1	5.360000-1	925	2151	117
4.0	1.0	3.0	0.0	5.360000-1	5.360000-1	925	2151	118
4.0	3.0	2.0	0.0	5.360000-1	5.360000-1	925	2151	119
4.0	3.0	3.0	0.0	5.360000-1	5.360000-1	925	2151	120
0.0	0.0	0	6	72	12	925	2151	121
43572.28944	1.013099+0	2.535128-2	3.110732-2			925	2151	122
						925	2151	123
385358.9216	5.818610+0	1.147663+3	7.000050+0	9.721652+1	2.700573+3	925	2151	124
1.029956+0	1.014654+0	1.011431+0				925	2151	125
623498.3906	5.483625+0	1.879520+2	5.141180+2	2.573738+4	7.363058+0	925	2151	126
6.738781+1	1.010791+1	1.119461+2				925	2151	127
663159.3684	2.688265+0	1.615437+0	4.608794+0	3.185929+3	3.117127+1	925	2151	128
2.249077+5	3.005035+1	3.013227+1				925	2151	129
1113162.179	4.827504-1	1.060428+0	8.718579+2	8.142907+4	1.203956+0	925	2151	130
-1.805244+4	1.453709+0	2.319971+1				925	2151	131
1383534.169	5.000000-1	2.481578+3	1.664637+0	-2.386769+1	3.216871+1	925	2151	132
2.256689+5	1.213025+0	1.324141+0				925	2151	133
3.0	0.0	0	0	42	7	925	2151	134
1.0	0.0	0.0	0.0			925	2151	135

2.0	2.0	1.0	0.0	5.360000-1	5.360000-1	925	2151	136	
3.0	3.0	0.0	0.0	5.360000-1	5.360000-1	925	2151	137	
3.0	3.0	-1.0	0.0	5.360000-1	5.360000-1	925	2151	138	
4.0	0.0	3.0	0.0	5.360000-1	5.360000-1	925	2151	139	
4.0	2.0	2.0	0.0	5.360000-1	5.360000-1	925	2151	140	
4.0	2.0	3.0	0.0	5.360000-1	5.360000-1	925	2151	141	
0.0	0.0	0	2		24	4	925	2151	142
173599.3155	5.096430+0	2.142181-1	9.260881-2	5.206590-2			925	2151	143
							925	2151	144
945180.5782	7.792306-1	1.130323+4	2.452522+0	1.820394+3	3.152168+1		925	2151	145
2.491812+4	2.291704+0						925	2151	146
-4.0	0.0	0	0	30		5	925	2151	147
1.0	0.0	0.0	0.0				925	2151	148
2.0	3.0	1.0	0.0	5.360000-1	5.360000-1	925	2151	149	
4.0	1.0	3.0	0.0	5.360000-1	5.360000-1	925	2151	150	
4.0	3.0	2.0	0.0	5.360000-1	5.360000-1	925	2151	151	
4.0	3.0	3.0	0.0	5.360000-1	5.360000-1	925	2151	152	
0.0	0.0	0	0	6		1	925	2151	153

APPENDIX C

³⁵Cl ENDF/B-VII.1 RESOLVED FILE2 LRF=7 DATA

1.703500+4	3.466850+1	0	0	1	01725	2151	1
1.703500+4	1.000000+0	0	0	1	01725	2151	2
1.000000-5	1.200000+6	1	7	0	01725	2151	3
0.000000+0	0.000000+0	0	3	8	01725	2151	4
0.000000+0	0.000000+0	3	0	36	61725	2151	5
0.000000+0	3.566850+1	0.000000+0	0.000000+0	1.000000+0	0.000000+01725	2151	6
0.000000+0	0.000000+0	-1.000000+0	1.020000+2	0.000000+0	0.000000+01725	2151	7
1.000000+0	3.466850+1	0.000000+0	0.000000+0	5.000000-1	1.500000+01725	2151	8
0.000000+0	1.000000+0	-1.000000+0	2.000000+0	0.000000+0	0.000000+01725	2151	9
9.986240-1	3.466850+1	1.000000+0	1.600000+1	5.000000-1	1.500000+01725	2151	10
6.152200+5	1.000000+0	-1.000000+0	6.000000+2	0.000000+0	0.000000+01725	2151	11
1.000000+0	0.000000+0	0	0	18	31725	2151	12
1.000000+0	0.000000+0	0.000000+0	0.000000+0	0.000000+0	0.000000+01725	2151	13
2.000000+0	0.000000+0	1.000000+0	0.000000+0	3.667980-1	4.822220-11725	2151	14
3.000000+0	0.000000+0	1.000000+0	0.000000+0	3.667980-1	4.822220-11725	2151	15
0.000000+0	0.000000+0	0	23	138	231725	2151	16
5.493200+4	3.672600-1	4.644240+1	0.000000+0	0.000000+0	0.000000+01725	2151	17
6.823616+4	3.933600-1	2.179040+2	1.000000-5	0.000000+0	0.000000+01725	2151	18
1.150980+5	7.390000-1	4.307780+0	0.000000+0	0.000000+0	0.000000+01725	2151	19
1.825230+5	7.451500-1	1.759740+3	4.000000-1	0.000000+0	0.000000+01725	2151	20
2.397427+5	6.871600-1	2.685470+2	0.000000+0	0.000000+0	0.000000+01725	2151	21
3.351287+5	3.583800-1	5.525660+3	0.000000+0	0.000000+0	0.000000+01725	2151	22
3.991469+5	7.409700-1	1.093810+3	0.000000+0	0.000000+0	0.000000+01725	2151	23
4.156650+5	3.286800-1	1.146260+3	0.000000+0	0.000000+0	0.000000+01725	2151	24
4.506303+5	3.929900-1	4.613320+2	0.000000+0	0.000000+0	0.000000+01725	2151	25
4.997896+5	6.704600-1	2.312410+3	0.000000+0	0.000000+0	0.000000+01725	2151	26
5.422214+5	6.060000-1	5.220340+2	0.000000+0	0.000000+0	0.000000+01725	2151	27
6.542074+5	6.060000-1	5.186030+2	0.000000+0	0.000000+0	0.000000+01725	2151	28
6.652896+5	6.060000-1	1.406720+2	0.000000+0	0.000000+0	0.000000+01725	2151	29
6.723573+5	6.060000-1	5.754080+2	0.000000+0	0.000000+0	0.000000+01725	2151	30
6.780000+5	6.060000-1	1.331580+2	0.000000+0	0.000000+0	0.000000+01725	2151	31
6.949358+5	6.060000-1	1.824950+3	0.000000+0	0.000000+0	0.000000+01725	2151	32
7.251773+5	6.060000-1	1.672450+2	0.000000+0	0.000000+0	0.000000+01725	2151	33
7.546912+5	6.060000-1	2.690680+3	0.000000+0	0.000000+0	0.000000+01725	2151	34
7.814646+5	6.060000-1	1.294130+3	0.000000+0	0.000000+0	0.000000+01725	2151	35
8.315787+5	8.600000-1	4.453040+2	0.000000+0	0.000000+0	0.000000+01725	2151	36
8.829776+5	6.060000-1	9.780610+2	0.000000+0	0.000000+0	0.000000+01725	2151	37
1.109188+6	6.060000-1	2.742350+3	0.000000+0	0.000000+0	0.000000+01725	2151	38
1.205687+6	6.060000-1	6.425840+2	0.000000+0	0.000000+0	0.000000+01725	2151	39
2.000000+0	0.000000+0	0	0	18	31725	2151	40
1.000000+0	0.000000+0	0.000000+0	0.000000+0	0.000000+0	0.000000+01725	2151	41
2.000000+0	0.000000+0	2.000000+0	0.000000+0	3.667980-1	4.822220-11725	2151	42
3.000000+0	0.000000+0	2.000000+0	0.000000+0	3.667980-1	4.822220-11725	2151	43
0.000000+0	0.000000+0	0	32	192	321725	2151	44
-1.806500+2	5.301500-1	1.327700+1	5.992300-3	0.000000+0	0.000000+01725	2151	45
1.480195+4	3.456800-1	3.259950+1	2.800020-2	0.000000+0	0.000000+01725	2151	46
2.661579+4	3.041500-1	1.154980+2	0.000000+0	0.000000+0	0.000000+01725	2151	47
7.549467+4	8.059200-1	7.991540-2	1.000000-5	0.000000+0	0.000000+01725	2151	48
1.304435+5	7.593500-1	7.665700-1	0.000000+0	0.000000+0	0.000000+01725	2151	49
2.149232+5	3.485100-1	6.528390+2	0.000000+0	0.000000+0	0.000000+01725	2151	50
2.425998+5	9.018300-1	3.440090+2	0.000000+0	0.000000+0	0.000000+01725	2151	51
2.846570+5	4.994200-1	1.194020+3	0.000000+0	0.000000+0	0.000000+01725	2151	52
3.137503+5	4.763300-1	1.475680+3	0.000000+0	0.000000+0	0.000000+01725	2151	53
3.310710+5	3.982400-1	3.276200+1	0.000000+0	0.000000+0	0.000000+01725	2151	54
3.389756+5	2.383300+0	8.777960+2	0.000000+0	0.000000+0	0.000000+01725	2151	55
3.802625+5	4.630100-1	1.178590+3	0.000000+0	0.000000+0	0.000000+01725	2151	56
3.864177+5	4.180700-1	1.240150+3	0.000000+0	0.000000+0	0.000000+01725	2151	57
4.593615+5	6.156500-1	3.859970+1	0.000000+0	0.000000+0	0.000000+01725	2151	58
4.886274+5	4.081400-1	7.806800+2	0.000000+0	0.000000+0	0.000000+01725	2151	59
5.143982+5	6.060000-1	5.284320+3	4.000000-1	0.000000+0	0.000000+01725	2151	60
5.279391+5	6.060000-1	2.812390+3	0.000000+0	0.000000+0	0.000000+01725	2151	61
5.590263+5	6.060000-1	1.813310+3	0.000000+0	0.000000+0	0.000000+01725	2151	62
5.908121+5	6.060000-1	3.235630+3	0.000000+0	0.000000+0	0.000000+01725	2151	63
6.216780+5	6.060000-1	6.758690+3	0.000000+0	0.000000+0	0.000000+01725	2151	64

6.310363+5	6.060000-1	1.636760+3	0.000000+0	0.000000+0	0.000000+01725	2151	65
6.408054+5	6.060000-1	8.597480+2	0.000000+0	0.000000+0	0.000000+01725	2151	66
6.578143+5	6.060000-1	2.069420+2	0.000000+0	0.000000+0	0.000000+01725	2151	67
6.810575+5	6.060000-1	6.654900+2	0.000000+0	0.000000+0	0.000000+01725	2151	68
6.902708+5	6.060000-1	4.632110+2	0.000000+0	0.000000+0	0.000000+01725	2151	69
7.799749+5	6.060000-1	5.311180+3	0.000000+0	0.000000+0	0.000000+01725	2151	70
8.249523+5	6.060000-1	2.763840+3	0.000000+0	0.000000+0	0.000000+01725	2151	71
8.609610+5	6.060000-1	7.202410+3	0.000000+0	0.000000+0	0.000000+01725	2151	72
1.053393+6	6.060000-1	2.038130+3	0.000000+0	0.000000+0	0.000000+01725	2151	73
1.137885+6	6.060000-1	1.835530+3	0.000000+0	0.000000+0	0.000000+01725	2151	74
1.257680+6	6.060000-1	1.749830+3	0.000000+0	0.000000+0	0.000000+01725	2151	75
7.563145+6	3.839800-1	6.219050+5	1.000000+3	0.000000+0	0.000000+01725	2151	76
0.000000+0	-1.000000+0	0	0	18	31725	2151	77
1.000000+0	1.000000+0	0.000000+0	0.000000+0	0.000000+0	0.000000+01725	2151	78
2.000000+0	1.000000+0	1.000000+0	0.000000+0	4.888750-1	4.822220-11725	2151	79
3.000000+0	1.000000+0	1.000000+0	0.000000+0	4.888750-1	4.822220-11725	2151	80
0.000000+0	0.000000+0	0	9	54	91725	2151	81
2.239640+4	1.724800+0	9.663670-1	0.000000+0	0.000000+0	0.000000+01725	2151	82
9.660415+4	1.565000+0	2.761380+0	0.000000+0	0.000000+0	0.000000+01725	2151	83
2.300740+5	3.240100-1	8.118180+2	0.000000+0	0.000000+0	0.000000+01725	2151	84
2.432153+5	7.032000-1	2.174300+2	0.000000+0	0.000000+0	0.000000+01725	2151	85
2.454785+5	8.319700-1	6.556420+0	0.000000+0	0.000000+0	0.000000+01725	2151	86
3.413389+5	6.549700-1	5.720320+3	0.000000+0	0.000000+0	0.000000+01725	2151	87
4.812809+5	7.821300-1	1.774270+3	0.000000+0	0.000000+0	0.000000+01725	2151	88
5.048567+5	8.600000-1	6.790940+2	0.000000+0	0.000000+0	0.000000+01725	2151	89
5.478545+5	8.600000-1	7.640130+2	0.000000+0	0.000000+0	0.000000+01725	2151	90
-1.000000+0	0.000000+0	0	0	18	31725	2151	91
1.000000+0	1.000000+0	0.000000+0	0.000000+0	0.000000+0	0.000000+01725	2151	92
2.000000+0	1.000000+0	1.000000+0	0.000000+0	4.888750-1	4.822220-11725	2151	93
3.000000+0	1.000000+0	1.000000+0	0.000000+0	4.888750-1	4.822220-11725	2151	94
0.000000+0	0.000000+0	0	38	228	381725	2151	95
4.250762+3	4.720000-1	6.280000-1	2.300000-1	0.000000+0	0.000000+01725	2151	96
5.491020+3	9.702100-1	3.863540-3	0.000000+0	0.000000+0	0.000000+01725	2151	97
3.776792+4	1.912000-1	4.407970-1	0.000000+0	0.000000+0	0.000000+01725	2151	98
4.416635+4	1.042900+0	3.054660+1	0.000000+0	0.000000+0	0.000000+01725	2151	99
6.277945+4	6.209000-1	1.345600+2	0.000000+0	0.000000+0	0.000000+01725	2151	100
1.035154+5	3.880500-1	3.819530+2	1.972980+0	0.000000+0	0.000000+01725	2151	101
1.351161+5	3.410900-1	1.875460+2	0.000000+0	0.000000+0	0.000000+01725	2151	102
1.625608+5	6.471800-1	5.634890+0	0.000000+0	0.000000+0	0.000000+01725	2151	103
1.654823+5	1.050100+0	2.072840+2	0.000000+0	0.000000+0	0.000000+01725	2151	104
2.199922+5	4.001800-1	3.847750+0	0.000000+0	0.000000+0	0.000000+01725	2151	105
2.241121+5	4.033900-1	7.567220+2	0.000000+0	0.000000+0	0.000000+01725	2151	106
2.288860+5	5.941900-1	1.768540+0	0.000000+0	0.000000+0	0.000000+01725	2151	107
2.615514+5	8.458200-1	1.063750+3	0.000000+0	0.000000+0	0.000000+01725	2151	108
2.791149+5	3.767200-1	1.254490+3	0.000000+0	0.000000+0	0.000000+01725	2151	109
2.845043+5	9.053700-1	4.161730+0	0.000000+0	0.000000+0	0.000000+01725	2151	110
3.060336+5	5.628500-1	7.718360+0	0.000000+0	0.000000+0	0.000000+01725	2151	111
3.074111+5	6.403400-1	1.172260+3	0.000000+0	0.000000+0	0.000000+01725	2151	112
3.406957+5	5.654300-1	3.875200+3	0.000000+0	0.000000+0	0.000000+01725	2151	113
3.819655+5	8.183600+0	1.602770+0	0.000000+0	0.000000+0	0.000000+01725	2151	114
3.878895+5	9.112300-1	3.238570+3	0.000000+0	0.000000+0	0.000000+01725	2151	115
4.044696+5	1.492300+0	1.010090+3	0.000000+0	0.000000+0	0.000000+01725	2151	116
4.526283+5	8.600500-1	3.430810+3	4.000000-1	0.000000+0	0.000000+01725	2151	117
4.653384+5	3.666800-1	6.938600+2	0.000000+0	0.000000+0	0.000000+01725	2151	118
5.526254+5	8.600000-1	2.791240+2	0.000000+0	0.000000+0	0.000000+01725	2151	119
5.592470+5	8.600000-1	5.857230+2	4.000000-1	0.000000+0	0.000000+01725	2151	120
5.913358+5	8.600000-1	1.674080+2	0.000000+0	0.000000+0	0.000000+01725	2151	121
6.008407+5	8.600000-1	1.208510+3	0.000000+0	0.000000+0	0.000000+01725	2151	122
6.295837+5	8.600000-1	6.225330+2	0.000000+0	0.000000+0	0.000000+01725	2151	123
6.593525+5	8.600000-1	1.356080+2	0.000000+0	0.000000+0	0.000000+01725	2151	124
7.183788+5	8.600000-1	9.740400+2	0.000000+0	0.000000+0	0.000000+01725	2151	125
7.328902+5	8.600000-1	1.955950+3	0.000000+0	0.000000+0	0.000000+01725	2151	126
8.103378+5	8.600000-1	5.088680+2	0.000000+0	0.000000+0	0.000000+01725	2151	127
8.715664+5	8.600000-1	1.987240+3	4.000000-1	0.000000+0	0.000000+01725	2151	128
9.439464+5	8.600000-1	5.556340+2	0.000000+0	0.000000+0	0.000000+01725	2151	129
9.845132+5	8.600000-1	1.801810+3	0.000000+0	0.000000+0	0.000000+01725	2151	130
1.138720+6	8.600000-1	9.544250+2	0.000000+0	0.000000+0	0.000000+01725	2151	131
1.353551+6	8.600000-1	3.879680+4	0.000000+0	0.000000+0	0.000000+01725	2151	132
1.435502+6	8.600000-1	5.365630+3	0.000000+0	0.000000+0	0.000000+01725	2151	133
-2.000000+0	0.000000+0	0	0	18	31725	2151	134
1.000000+0	1.000000+0	0.000000+0	0.000000+0	0.000000+0	0.000000+01725	2151	135

2.000000+0	1.000000+0	1.000000+0	0.000000+0	4.888750-1	4.822220-11725	2151	136
3.000000+0	1.000000+0	1.000000+0	0.000000+0	4.888750-1	4.822220-11725	2151	137
0.000000+0	0.000000+0	0.000000+0	0	67	402	671725	2151 138
-3.369334+5	5.340100-1	3.820180+4	0.000000+0	0.000000+0	0.000000+01725	2151	139
2.734636+4	4.579210-1	6.027800+0	1.472210-1	0.000000+0	0.000000+01725	2151	140
5.297412+4	5.624100-1	8.159470-1	0.000000+0	0.000000+0	0.000000+01725	2151	141
5.781159+4	5.380650-1	1.073890+2	9.980470-1	0.000000+0	0.000000+01725	2151	142
9.042023+4	7.164960-1	2.178860+1	2.740270-1	0.000000+0	0.000000+01725	2151	143
9.052563+4	1.275920-1	4.235150+0	0.000000+0	0.000000+0	0.000000+01725	2151	144
1.134033+5	3.369900-1	1.422880+2	0.000000+0	0.000000+0	0.000000+01725	2151	145
1.408311+5	5.458500-1	9.871460+1	0.000000+0	0.000000+0	0.000000+01725	2151	146
1.498295+5	7.555300-1	1.132080+2	0.000000+0	0.000000+0	0.000000+01725	2151	147
1.926794+5	2.287600-1	3.381170+1	0.000000+0	0.000000+0	0.000000+01725	2151	148
2.010949+5	2.905500-1	3.650400+1	0.000000+0	0.000000+0	0.000000+01725	2151	149
2.066160+5	5.943300-1	5.594230-1	0.000000+0	0.000000+0	0.000000+01725	2151	150
2.145480+5	2.323800-1	4.238200+1	0.000000+0	0.000000+0	0.000000+01725	2151	151
2.153514+5	7.735500-1	4.558520+0	0.000000+0	0.000000+0	0.000000+01725	2151	152
2.170986+5	6.185100-1	5.772230+2	0.000000+0	0.000000+0	0.000000+01725	2151	153
2.213851+5	1.592700+0	4.073280+0	0.000000+0	0.000000+0	0.000000+01725	2151	154
2.458488+5	7.646700-1	5.612490+0	0.000000+0	0.000000+0	0.000000+01725	2151	155
2.501986+5	4.046000-1	4.345790+2	0.000000+0	0.000000+0	0.000000+01725	2151	156
2.856091+5	8.420300-1	1.568700+3	0.000000+0	0.000000+0	0.000000+01725	2151	157
2.900777+5	1.615200+0	1.520800+2	0.000000+0	0.000000+0	0.000000+01725	2151	158
3.014487+5	4.017200-1	8.855620+0	0.000000+0	0.000000+0	0.000000+01725	2151	159
3.038357+5	1.697600+0	6.957360+2	0.000000+0	0.000000+0	0.000000+01725	2151	160
3.455490+5	3.479100-1	6.319440+1	0.000000+0	0.000000+0	0.000000+01725	2151	161
3.543783+5	2.329000-1	8.058180+0	0.000000+0	0.000000+0	0.000000+01725	2151	162
3.844697+5	5.785800+0	1.985550+0	0.000000+0	0.000000+0	0.000000+01725	2151	163
4.078202+5	5.513100-1	2.040430+3	0.000000+0	0.000000+0	0.000000+01725	2151	164
4.386472+5	6.448700-1	1.273690+3	0.000000+0	0.000000+0	0.000000+01725	2151	165
4.444759+5	2.050000-1	1.810450+2	0.000000+0	0.000000+0	0.000000+01725	2151	166
4.513762+5	1.759900+0	5.759080+0	0.000000+0	0.000000+0	0.000000+01725	2151	167
4.578911+5	1.147400+0	7.322610+0	0.000000+0	0.000000+0	0.000000+01725	2151	168
4.655024+5	5.580100-1	4.040480+3	0.000000+0	0.000000+0	0.000000+01725	2151	169
4.691015+5	9.520300-1	3.761160+0	0.000000+0	0.000000+0	0.000000+01725	2151	170
4.771962+5	5.403700-1	1.658970+2	0.000000+0	0.000000+0	0.000000+01725	2151	171
4.854618+5	1.273200+0	4.799550+2	0.000000+0	0.000000+0	0.000000+01725	2151	172
5.437824+5	8.600000-1	6.917280+2	0.000000+0	0.000000+0	0.000000+01725	2151	173
5.645835+5	8.600000-1	5.359800+2	0.000000+0	0.000000+0	0.000000+01725	2151	174
5.738796+5	8.600000-1	1.469740+3	0.000000+0	0.000000+0	0.000000+01725	2151	175
6.330964+5	8.600000-1	1.445360+2	4.000000-1	0.000000+0	0.000000+01725	2151	176
6.427422+5	8.600000-1	9.499240+2	0.000000+0	0.000000+0	0.000000+01725	2151	177
7.125272+5	8.600000-1	3.300900+3	4.000000-1	0.000000+0	0.000000+01725	2151	178
7.295798+5	8.600000-1	6.465640+2	0.000000+0	0.000000+0	0.000000+01725	2151	179
7.398106+5	8.600000-1	3.042130+3	0.000000+0	0.000000+0	0.000000+01725	2151	180
7.702915+5	8.600000-1	3.185460+3	0.000000+0	0.000000+0	0.000000+01725	2151	181
7.985633+5	8.600000-1	2.910980+3	4.000000-1	0.000000+0	0.000000+01725	2151	182
8.273814+5	6.060000-1	4.360650+2	0.000000+0	0.000000+0	0.000000+01725	2151	183
8.322588+5	8.600000-1	1.382530+3	0.000000+0	0.000000+0	0.000000+01725	2151	184
8.484064+5	8.600000-1	2.391310+3	0.000000+0	0.000000+0	0.000000+01725	2151	185
8.524894+5	8.600000-1	1.726720+3	0.000000+0	0.000000+0	0.000000+01725	2151	186
8.950719+5	8.600000-1	1.505930+3	0.000000+0	0.000000+0	0.000000+01725	2151	187
9.156492+5	8.600000-1	1.033970+3	0.000000+0	0.000000+0	0.000000+01725	2151	188
9.331357+5	8.600000-1	9.386810+2	0.000000+0	0.000000+0	0.000000+01725	2151	189
9.533511+5	8.600000-1	1.000950+3	4.000000-1	0.000000+0	0.000000+01725	2151	190
9.915402+5	8.600000-1	4.348100+3	0.000000+0	0.000000+0	0.000000+01725	2151	191
1.006461+6	8.600000-1	3.591290+3	0.000000+0	0.000000+0	0.000000+01725	2151	192
1.028543+6	8.600000-1	2.388860+3	0.000000+0	0.000000+0	0.000000+01725	2151	193
1.055512+6	8.600000-1	3.888630+3	0.000000+0	0.000000+0	0.000000+01725	2151	194
1.074009+6	8.600000-1	1.039250+3	0.000000+0	0.000000+0	0.000000+01725	2151	195
1.080187+6	8.600000-1	7.511970+2	0.000000+0	0.000000+0	0.000000+01725	2151	196
1.115662+6	8.600000-1	3.444140+3	0.000000+0	0.000000+0	0.000000+01725	2151	197
1.131997+6	8.600000-1	1.523380+3	0.000000+0	0.000000+0	0.000000+01725	2151	198
1.165343+6	8.600000-1	7.309520+3	0.000000+0	0.000000+0	0.000000+01725	2151	199
1.198501+6	8.600000-1	3.243460+3	0.000000+0	0.000000+0	0.000000+01725	2151	200
1.218130+6	8.600000-1	3.246660+3	0.000000+0	0.000000+0	0.000000+01725	2151	201
1.243534+6	8.600000-1	3.096960+3	0.000000+0	0.000000+0	0.000000+01725	2151	202
1.311787+6	8.600000-1	7.946430+2	0.000000+0	0.000000+0	0.000000+01725	2151	203
1.354056+6	8.600000-1	1.103350+4	0.000000+0	0.000000+0	0.000000+01725	2151	204
1.434336+6	8.600000-1	5.422940+3	0.000000+0	0.000000+0	0.000000+01725	2151	205
-1.000000+0	0.000000+0	0	0	18	31725	2151	206

1.000000+0	1.000000+0	0.000000+0	0.000000+0	0.000000+0	0.000000+0	0.000000+01725	2151	207
2.000000+0	1.000000+0	2.000000+0	0.000000+0	4.888750-1	4.822220-11725	2151	2151	208
3.000000+0	1.000000+0	2.000000+0	0.000000+0	4.888750-1	4.822220-11725	2151	2151	209
0.000000+0	0.000000+0	0	18	108	181725	2151	2151	210
1.339884+5	2.314200+0	6.600970+2	4.000000-1	0.000000+0	0.000000+01725	2151	2151	211
2.251416+5	1.346200+0	5.685270+2	4.000000-1	0.000000+0	0.000000+01725	2151	2151	212
3.728997+5	2.107900+0	1.796360+3	4.000000-1	0.000000+0	0.000000+01725	2151	2151	213
4.019221+5	3.329500-1	1.212200+3	0.000000+0	0.000000+0	0.000000+01725	2151	2151	214
4.221047+5	2.868200+0	8.577140+2	0.000000+0	0.000000+0	0.000000+01725	2151	2151	215
4.836869+5	1.907300+0	2.735270+3	4.000000-1	0.000000+0	0.000000+01725	2151	2151	216
5.811770+5	8.600000-1	2.087720+2	0.000000+0	0.000000+0	0.000000+01725	2151	2151	217
6.142552+5	8.600000-1	1.153480+3	0.000000+0	0.000000+0	0.000000+01725	2151	2151	218
7.219908+5	8.600000-1	8.268190+2	0.000000+0	0.000000+0	0.000000+01725	2151	2151	219
7.484834+5	8.600000-1	1.023870+3	0.000000+0	0.000000+0	0.000000+01725	2151	2151	220
7.654137+5	8.600000-1	1.519860+3	0.000000+0	0.000000+0	0.000000+01725	2151	2151	221
7.927810+5	8.600000-1	1.040840+3	0.000000+0	0.000000+0	0.000000+01725	2151	2151	222
8.451494+5	8.600000-1	4.176760+3	0.000000+0	0.000000+0	0.000000+01725	2151	2151	223
9.366575+5	8.600000-1	6.061270+2	0.000000+0	0.000000+0	0.000000+01725	2151	2151	224
9.747505+5	8.600000-1	3.259090+3	0.000000+0	0.000000+0	0.000000+01725	2151	2151	225
1.091954+6	8.600000-1	1.974980+3	0.000000+0	0.000000+0	0.000000+01725	2151	2151	226
1.177028+6	8.600000-1	1.488160+3	0.000000+0	0.000000+0	0.000000+01725	2151	2151	227
1.225254+6	8.600000-1	1.807190+3	0.000000+0	0.000000+0	0.000000+01725	2151	2151	228
-2.000000+0	0.000000+0	0	0	18	31725	2151	2151	229
1.000000+0	1.000000+0	0.000000+0	0.000000+0	0.000000+0	0.000000+01725	2151	2151	230
2.000000+0	1.000000+0	2.000000+0	0.000000+0	4.888750-1	4.822220-11725	2151	2151	231
3.000000+0	1.000000+0	2.000000+0	0.000000+0	4.888750-1	4.822220-11725	2151	2151	232
0.000000+0	0.000000+0	0	28	168	281725	2151	2151	233
3.978154+2	6.650000-1	5.050000-2	3.220000-1	0.000000+0	0.000000+01725	2151	2151	234
1.136064+5	2.947700-1	3.972030+2	0.000000+0	0.000000+0	0.000000+01725	2151	2151	235
1.430242+5	4.921800-1	3.147430+2	0.000000+0	0.000000+0	0.000000+01725	2151	2151	236
2.059671+5	4.506700-1	5.887780-1	0.000000+0	0.000000+0	0.000000+01725	2151	2151	237
2.837547+5	6.466700-1	4.237100+2	0.000000+0	0.000000+0	0.000000+01725	2151	2151	238
2.870089+5	5.536890-1	2.126030+1	0.000000+0	0.000000+0	0.000000+01725	2151	2151	239
2.949461+5	7.387600-1	4.747470+2	4.000000-1	0.000000+0	0.000000+01725	2151	2151	240
5.903574+5	8.600000-1	7.550480+2	4.000000-1	0.000000+0	0.000000+01725	2151	2151	241
6.181025+5	8.600000-1	1.075440+3	0.000000+0	0.000000+0	0.000000+01725	2151	2151	242
7.036239+5	8.600000-1	9.311240+2	0.000000+0	0.000000+0	0.000000+01725	2151	2151	243
7.350094+5	8.600000-1	3.777530+2	0.000000+0	0.000000+0	0.000000+01725	2151	2151	244
8.013281+5	8.600000-1	6.807230+2	0.000000+0	0.000000+0	0.000000+01725	2151	2151	245
8.358532+5	8.600000-1	1.181190+3	0.000000+0	0.000000+0	0.000000+01725	2151	2151	246
8.769947+5	8.600000-1	5.757280+2	0.000000+0	0.000000+0	0.000000+01725	2151	2151	247
9.225158+5	8.600000-1	1.571600+3	0.000000+0	0.000000+0	0.000000+01725	2151	2151	248
9.461013+5	8.600000-1	4.806310+2	0.000000+0	0.000000+0	0.000000+01725	2151	2151	249
9.810389+5	8.600000-1	4.229000+3	0.000000+0	0.000000+0	0.000000+01725	2151	2151	250
9.998479+5	8.600000-1	3.022270+3	0.000000+0	0.000000+0	0.000000+01725	2151	2151	251
1.016475+6	8.600000-1	4.019670+3	0.000000+0	0.000000+0	0.000000+01725	2151	2151	252
1.050581+6	8.600000-1	1.304140+3	0.000000+0	0.000000+0	0.000000+01725	2151	2151	253
1.088712+6	8.600000-1	5.239370+3	0.000000+0	0.000000+0	0.000000+01725	2151	2151	254
1.116025+6	8.600000-1	4.363740+4	0.000000+0	0.000000+0	0.000000+01725	2151	2151	255
1.172051+6	8.600000-1	1.494510+3	0.000000+0	0.000000+0	0.000000+01725	2151	2151	256
1.283751+6	8.600000-1	5.041400+3	0.000000+0	0.000000+0	0.000000+01725	2151	2151	257
1.337132+6	8.600000-1	4.850280+3	0.000000+0	0.000000+0	0.000000+01725	2151	2151	258
1.366148+6	8.600000-1	8.350230+3	0.000000+0	0.000000+0	0.000000+01725	2151	2151	259
1.403885+6	8.600000-1	8.067070+3	0.000000+0	0.000000+0	0.000000+01725	2151	2151	260
1.441365+6	8.600000-1	1.608740+3	0.000000+0	0.000000+0	0.000000+01725	2151	2151	261
-3.000000+0	0.000000+0	0	0	18	31725	2151	2151	262
1.000000+0	1.000000+0	0.000000+0	0.000000+0	0.000000+0	0.000000+01725	2151	2151	263
2.000000+0	1.000000+0	2.000000+0	0.000000+0	4.888750-1	4.822220-11725	2151	2151	264
3.000000+0	1.000000+0	2.000000+0	0.000000+0	4.888750-1	4.822220-11725	2151	2151	265
0.000000+0	0.000000+0	0	57	342	571725	2151	2151	266
1.635612+4	3.865000-1	5.981800+0	1.640190-1	0.000000+0	0.000000+01725	2151	2151	267
1.713387+4	8.022800-1	1.409590+1	3.199990-2	0.000000+0	0.000000+01725	2151	2151	268
4.027028+4	5.774900-1	1.773460-1	0.000000+0	0.000000+0	0.000000+01725	2151	2151	269
5.160803+4	4.471700-2	2.417150+0	9.599660-2	0.000000+0	0.000000+01725	2151	2151	270
9.520675+4	4.531600-1	1.549000-1	0.000000+0	0.000000+0	0.000000+01725	2151	2151	271
9.944099+4	2.322700-1	2.393210+0	0.000000+0	0.000000+0	0.000000+01725	2151	2151	272
1.120451+5	3.240700-1	2.642330-1	0.000000+0	0.000000+0	0.000000+01725	2151	2151	273
1.400910+5	3.664800-1	3.778030+0	0.000000+0	0.000000+0	0.000000+01725	2151	2151	274
1.416415+5	3.131300-1	3.954240+0	0.000000+0	0.000000+0	0.000000+01725	2151	2151	275
1.529224+5	2.989300-1	3.820560-1	0.000000+0	0.000000+0	0.000000+01725	2151	2151	276
1.835405+5	3.333300-1	4.615080+2	0.000000+0	0.000000+0	0.000000+01725	2151	2151	277

1.852814+5	4.665000-1	4.482330+0	0.000000+0	0.000000+0	0.000000+01725	2151	278
1.881523+5	4.975300-1	4.222480+2	0.000000+0	0.000000+0	0.000000+01725	2151	279
1.901806+5	2.935300-1	1.024950+2	0.000000+0	0.000000+0	0.000000+01725	2151	280
1.929420+5	7.559100-1	1.635970+1	0.000000+0	0.000000+0	0.000000+01725	2151	281
1.991683+5	2.550000-1	2.775550+0	0.000000+0	0.000000+0	0.000000+01725	2151	282
2.933823+5	1.802700+0	5.941830+0	0.000000+0	0.000000+0	0.000000+01725	2151	283
3.367631+5	4.162100-1	2.890370+2	0.000000+0	0.000000+0	0.000000+01725	2151	284
4.753035+5	8.300600-1	2.791800+3	0.000000+0	0.000000+0	0.000000+01725	2151	285
5.097591+5	8.600000-1	3.870270+2	0.000000+0	0.000000+0	0.000000+01725	2151	286
5.298958+5	8.600000-1	1.353670+3	0.000000+0	0.000000+0	0.000000+01725	2151	287
5.352483+5	8.600000-1	4.481020+2	0.000000+0	0.000000+0	0.000000+01725	2151	288
6.080558+5	8.600000-1	7.747700+2	0.000000+0	0.000000+0	0.000000+01725	2151	289
6.657961+5	8.600000-1	2.099450+2	0.000000+0	0.000000+0	0.000000+01725	2151	290
6.739830+5	6.060000-1	4.896460+1	0.000000+0	0.000000+0	0.000000+01725	2151	291
6.816687+5	8.600000-1	6.028770+1	0.000000+0	0.000000+0	0.000000+01725	2151	292
6.850220+5	8.600000-1	1.172880+2	0.000000+0	0.000000+0	0.000000+01725	2151	293
7.010023+5	8.600000-1	1.251920+3	0.000000+0	0.000000+0	0.000000+01725	2151	294
7.574622+5	8.600000-1	3.780250+3	0.000000+0	0.000000+0	0.000000+01725	2151	295
7.611067+5	8.600000-1	2.238910+3	0.000000+0	0.000000+0	0.000000+01725	2151	296
7.749692+5	8.600000-1	3.689300+2	0.000000+0	0.000000+0	0.000000+01725	2151	297
8.068823+5	8.600000-1	6.298260+2	0.000000+0	0.000000+0	0.000000+01725	2151	298
8.389452+5	8.600000-1	3.394540+3	0.000000+0	0.000000+0	0.000000+01725	2151	299
8.626053+5	8.600000-1	6.945570+2	0.000000+0	0.000000+0	0.000000+01725	2151	300
8.865767+5	8.600000-1	3.197900+3	0.000000+0	0.000000+0	0.000000+01725	2151	301
9.058611+5	8.600000-1	4.411560+2	4.000000-1	0.000000+0	0.000000+01725	2151	302
9.109009+5	8.600000-1	3.339470+3	0.000000+0	0.000000+0	0.000000+01725	2151	303
9.504659+5	8.600000-1	6.451080+2	0.000000+0	0.000000+0	0.000000+01725	2151	304
1.010401+6	8.600000-1	7.910460+3	0.000000+0	0.000000+0	0.000000+01725	2151	305
1.033683+6	8.600000-1	3.549570+3	0.000000+0	0.000000+0	0.000000+01725	2151	306
1.062148+6	8.600000-1	4.207760+2	0.000000+0	0.000000+0	0.000000+01725	2151	307
1.071198+6	8.600000-1	1.944480+3	0.000000+0	0.000000+0	0.000000+01725	2151	308
1.085425+6	8.600000-1	1.339760+2	0.000000+0	0.000000+0	0.000000+01725	2151	309
1.103724+6	8.600000-1	1.609290+3	0.000000+0	0.000000+0	0.000000+01725	2151	310
1.120932+6	8.600000-1	3.890220+2	0.000000+0	0.000000+0	0.000000+01725	2151	311
1.126914+6	8.600000-1	6.155220+2	0.000000+0	0.000000+0	0.000000+01725	2151	312
1.144865+6	8.600000-1	1.586600+3	0.000000+0	0.000000+0	0.000000+01725	2151	313
1.155330+6	8.600000-1	1.577740+3	0.000000+0	0.000000+0	0.000000+01725	2151	314
1.189685+6	8.600000-1	7.290220+3	0.000000+0	0.000000+0	0.000000+01725	2151	315
1.209020+6	8.600000-1	3.485080+3	0.000000+0	0.000000+0	0.000000+01725	2151	316
1.237194+6	8.600000-1	5.888380+3	0.000000+0	0.000000+0	0.000000+01725	2151	317
1.268642+6	8.600000-1	2.391480+3	0.000000+0	0.000000+0	0.000000+01725	2151	318
1.277668+6	8.600000-1	2.984480+3	0.000000+0	0.000000+0	0.000000+01725	2151	319
1.315129+6	8.600000-1	1.210580+4	0.000000+0	0.000000+0	0.000000+01725	2151	320
1.390745+6	8.600000-1	5.502450+3	0.000000+0	0.000000+0	0.000000+01725	2151	321
1.425393+6	8.600000-1	1.381970+4	0.000000+0	0.000000+0	0.000000+01725	2151	322
1.485128+6	8.600000-1	1.054090+4	0.000000+0	0.000000+0	0.000000+01725	2151	323

APPENDIX D

²³⁸U ENDF/B-VII.1 UNRESOLVED FILE2 LRF=1 DATA

2.000000+4	1.490288+5		2		2		0		09237	2151	3350
0.000000+0	9.433790-1		1		0		3		09237	2151	3351
2.360058+2	0.000000+0		0		0		1		09237	2151	3352
5.000000-1	0.000000+0		5		0		114		189237	2151	3353
0.000000+0	0.000000+0	2.000000+0	1.000000+0	0.000000+0	0.000000+0	0.000000+0	0.000000+0	0.000000+0	09237	2151	3354
2.000000+4	2.199760+1	0.000000+0	2.063460-3	2.281190-2	0.000000+0	0.000000+0	0.000000+0	0.000000+0	09237	2151	3355
2.300000+4	2.185120+1	0.000000+0	2.043260-3	2.284390-2	0.000000+0	0.000000+0	0.000000+0	0.000000+0	09237	2151	3356
2.600000+4	2.170590+1	0.000000+0	2.023690-3	2.287600-2	0.000000+0	0.000000+0	0.000000+0	0.000000+0	09237	2151	3357
3.000000+4	2.151390+1	0.000000+0	1.998440-3	2.291910-2	0.000000+0	0.000000+0	0.000000+0	0.000000+0	09237	2151	3358
3.500000+4	2.127610+1	0.000000+0	1.967970-3	2.297280-2	0.000000+0	0.000000+0	0.000000+0	0.000000+0	09237	2151	3359
4.000000+4	2.104110+1	0.000000+0	1.938570-3	2.302660-2	0.000000+0	0.000000+0	0.000000+0	0.000000+0	09237	2151	3360
4.500000+4	2.080860+1	0.000000+0	1.910100-3	2.308050-2	0.000000+0	0.000000+0	0.000000+0	0.000000+0	09237	2151	3361
4.509020+4	2.080440+1	0.000000+0	1.909600-3	2.308140-2	0.000000+0	0.000000+0	0.000000+0	0.000000+0	09237	2151	3362
5.000000+4	2.057890+1	1.097450-5	1.882470-3	2.313450-2	0.000000+0	0.000000+0	0.000000+0	0.000000+0	09237	2151	3363
5.500000+4	2.035200+1	6.242520-5	1.855610-3	2.318890-2	0.000000+0	0.000000+0	0.000000+0	0.000000+0	09237	2151	3364
6.000000+4	2.012740+1	1.703450-4	1.829400-3	2.324300-2	0.000000+0	0.000000+0	0.000000+0	0.000000+0	09237	2151	3365
7.000000+4	1.968630+1	5.935770-4	1.778900-3	2.335250-2	0.000000+0	0.000000+0	0.000000+0	0.000000+0	09237	2151	3366
8.000000+4	1.925540+1	1.332900-3	1.730620-3	2.346240-2	0.000000+0	0.000000+0	0.000000+0	0.000000+0	09237	2151	3367
9.000000+4	1.883420+1	2.416260-3	1.684330-3	2.357300-2	0.000000+0	0.000000+0	0.000000+0	0.000000+0	09237	2151	3368
1.000000+5	1.842260+1	3.857070-3	1.639840-3	2.368410-2	0.000000+0	0.000000+0	0.000000+0	0.000000+0	09237	2151	3369
1.200000+5	1.762720+1	7.818620-3	1.555690-3	2.390780-2	0.000000+0	0.000000+0	0.000000+0	0.000000+0	09237	2151	3370
1.400000+5	1.686740+1	1.317280-2	1.477270-3	2.424070-2	0.000000+0	0.000000+0	0.000000+0	0.000000+0	09237	2151	3371
1.490288+5	1.653580+1	1.601860-2	1.443570-3	2.434410-2	0.000000+0	0.000000+0	0.000000+0	0.000000+0	09237	2151	3372
2.360058+2	0.000000+0		1		0		2		09237	2151	3373
5.000000-1	0.000000+0		5		0		114		189237	2151	3374
0.000000+0	0.000000+0	1.000000+0	1.000000+0	0.000000+0	0.000000+0	0.000000+0	0.000000+0	0.000000+0	09237	2151	3375
2.000000+4	2.199760+1	0.000000+0	4.503430-3	2.291280-2	0.000000+0	0.000000+0	0.000000+0	0.000000+0	09237	2151	3376
2.300000+4	2.185120+1	0.000000+0	4.482640-3	2.294500-2	0.000000+0	0.000000+0	0.000000+0	0.000000+0	09237	2151	3377
2.600000+4	2.170590+1	0.000000+0	4.461360-3	2.297720-2	0.000000+0	0.000000+0	0.000000+0	0.000000+0	09237	2151	3378
3.000000+4	2.151390+1	0.000000+0	4.432310-3	2.302050-2	0.000000+0	0.000000+0	0.000000+0	0.000000+0	09237	2151	3379
3.500000+4	2.127610+1	0.000000+0	4.394890-3	2.307440-2	0.000000+0	0.000000+0	0.000000+0	0.000000+0	09237	2151	3380
4.000000+4	2.104110+1	0.000000+0	4.356510-3	2.312850-2	0.000000+0	0.000000+0	0.000000+0	0.000000+0	09237	2151	3381
4.500000+4	2.080860+1	0.000000+0	4.317220-3	2.318260-2	0.000000+0	0.000000+0	0.000000+0	0.000000+0	09237	2151	3382
4.509020+4	2.080440+1	0.000000+0	4.316510-3	2.318350-2	0.000000+0	0.000000+0	0.000000+0	0.000000+0	09237	2151	3383
5.000000+4	2.057890+1	4.778600-3	4.277230-3	2.323690-2	0.000000+0	0.000000+0	0.000000+0	0.000000+0	09237	2151	3384
5.500000+4	2.035200+1	1.339310-2	4.236630-3	2.329150-2	0.000000+0	0.000000+0	0.000000+0	0.000000+0	09237	2151	3385
6.000000+4	2.012740+1	2.415080-2	4.195410-3	2.334580-2	0.000000+0	0.000000+0	0.000000+0	0.000000+0	09237	2151	3386
7.000000+4	1.968630+1	4.976480-2	4.111800-3	2.345590-2	0.000000+0	0.000000+0	0.000000+0	0.000000+0	09237	2151	3387
8.000000+4	1.925540+1	7.874450-2	4.026940-3	2.356620-2	0.000000+0	0.000000+0	0.000000+0	0.000000+0	09237	2151	3388
9.000000+4	1.883420+1	1.095510-1	3.941300-3	2.367730-2	0.000000+0	0.000000+0	0.000000+0	0.000000+0	09237	2151	3389
1.000000+5	1.842260+1	1.411940-1	3.855300-3	2.378890-2	0.000000+0	0.000000+0	0.000000+0	0.000000+0	09237	2151	3390
1.200000+5	1.762720+1	2.044380-1	3.683500-3	2.401360-2	0.000000+0	0.000000+0	0.000000+0	0.000000+0	09237	2151	3391
1.400000+5	1.686740+1	2.649780-1	3.513680-3	2.424070-2	0.000000+0	0.000000+0	0.000000+0	0.000000+0	09237	2151	3392
1.490288+5	1.653580+1	2.908950-1	3.438120-3	2.434410-2	0.000000+0	0.000000+0	0.000000+0	0.000000+0	09237	2151	3393
1.500000+0	0.000000+0		5		0		114		189237	2151	3394
0.000000+0	0.000000+0	2.000000+0	1.000000+0	0.000000+0	0.000000+0	0.000000+0	0.000000+0	0.000000+0	09237	2151	3395
2.000000+4	1.142540+1	0.000000+0	2.339050-3	2.291280-2	0.000000+0	0.000000+0	0.000000+0	0.000000+0	09237	2151	3396
2.300000+4	1.134920+1	0.000000+0	2.328220-3	2.294500-2	0.000000+0	0.000000+0	0.000000+0	0.000000+0	09237	2151	3397
2.600000+4	1.127350+1	0.000000+0	2.317130-3	2.297720-2	0.000000+0	0.000000+0	0.000000+0	0.000000+0	09237	2151	3398
3.000000+4	1.117360+1	0.000000+0	2.302000-3	2.302050-2	0.000000+0	0.000000+0	0.000000+0	0.000000+0	09237	2151	3399
3.500000+4	1.104980+1	0.000000+0	2.282510-3	2.307440-2	0.000000+0	0.000000+0	0.000000+0	0.000000+0	09237	2151	3400
4.000000+4	1.092750+1	0.000000+0	2.262530-3	2.312850-2	0.000000+0	0.000000+0	0.000000+0	0.000000+0	09237	2151	3401
4.500000+4	1.080660+1	0.000000+0	2.242080-3	2.318260-2	0.000000+0	0.000000+0	0.000000+0	0.000000+0	09237	2151	3402
4.509020+4	1.080440+1	0.000000+0	2.241700-3	2.318350-2	0.000000+0	0.000000+0	0.000000+0	0.000000+0	09237	2151	3403
5.000000+4	1.068710+1	4.963260-3	2.221260-3	2.323690-2	0.000000+0	0.000000+0	0.000000+0	0.000000+0	09237	2151	3404
5.500000+4	1.056900+1	1.391030-2	2.200120-3	2.329150-2	0.000000+0	0.000000+0	0.000000+0	0.000000+0	09237	2151	3405
6.000000+4	1.045210+1	2.508280-2	2.178670-3	2.334580-2	0.000000+0	0.000000+0	0.000000+0	0.000000+0	09237	2151	3406
7.000000+4	1.022260+1	5.168320-2	2.135160-3	2.345590-2	0.000000+0	0.000000+0	0.000000+0	0.000000+0	09237	2151	3407
8.000000+4	9.998370+0	8.177630-2	2.090990-3	2.356620-2	0.000000+0	0.000000+0	0.000000+0	0.000000+0	09237	2151	3408
9.000000+4	9.779220+0	1.137640-1	2.046430-3	2.367730-2	0.000000+0	0.000000+0	0.000000+0	0.000000+0	09237	2151	3409
1.000000+5	9.565090+0	1.466170-1	2.001690-3	2.378890-2	0.000000+0	0.000000+0	0.000000+0	0.000000+0	09237	2151	3410
1.200000+5	9.151290+0	2.122710-1	1.912320-3	2.401360-2	0.000000+0	0.000000+0	0.000000+0	0.000000+0	09237	2151	3411
1.400000+5	8.756100+0	2.751070-1	1.824000-3	2.424070-2	0.000000+0	0.000000+0	0.000000+0	0.000000+0	09237	2151	3412
1.490288+5	8.583590+0	3.020030-1	1.784700-3	2.434410-2	0.000000+0	0.000000+0	0.000000+0	0.000000+0	09237	2151	3413

2.360058+2	0.000000+0	2	0	2	09237	2151	3414
1.500000+0	0.000000+0	5	0	114	189237	2151	3415
0.000000+0	0.000000+0	1.000000+0	1.000000+0	0.000000+0	0.000000+09237	2151	3416
2.000000+4	1.142540+1	0.000000+0	1.413040-3	2.281190-2	0.000000+09237	2151	3417
2.300000+4	1.134920+1	0.000000+0	1.403090-3	2.284390-2	0.000000+09237	2151	3418
2.600000+4	1.127350+1	0.000000+0	1.393210-3	2.287600-2	0.000000+09237	2151	3419
3.000000+4	1.117360+1	0.000000+0	1.380190-3	2.291910-2	0.000000+09237	2151	3420
3.500000+4	1.104980+1	0.000000+0	1.364060-3	2.297280-2	0.000000+09237	2151	3421
4.000000+4	1.092750+1	0.000000+0	1.348160-3	2.302660-2	0.000000+09237	2151	3422
4.500000+4	1.080660+1	0.000000+0	1.332460-3	2.308050-2	0.000000+09237	2151	3423
4.509020+4	1.080440+1	0.000000+0	1.332170-3	2.308140-2	0.000000+09237	2151	3424
5.000000+4	1.068710+1	7.183670-2	1.316960-3	2.313450-2	0.000000+09237	2151	3425
5.500000+4	1.056900+1	1.000490-1	1.301680-3	2.318890-2	0.000000+09237	2151	3426
6.000000+4	1.045210+1	1.205790-1	1.286570-3	2.324300-2	0.000000+09237	2151	3427
7.000000+4	1.022260+1	1.509840-1	1.256970-3	2.335250-2	0.000000+09237	2151	3428
8.000000+4	9.998370+0	1.736310-1	1.228140-3	2.346240-2	0.000000+09237	2151	3429
9.000000+4	9.779220+0	1.916700-1	1.200050-3	2.357300-2	0.000000+09237	2151	3430
1.000000+5	9.565090+0	2.065780-1	1.172680-3	2.368410-2	0.000000+09237	2151	3431
1.200000+5	9.151290+0	2.300510-1	1.120040-3	2.390780-2	0.000000+09237	2151	3432
1.400000+5	8.756100+0	2.478480-1	1.070090-3	2.424070-2	0.000000+09237	2151	3433
1.490288+5	8.583590+0	2.545650-1	1.048390-3	2.434410-2	0.000000+09237	2151	3434
2.500000+0	0.000000+0	5	0	114	189237	2151	3435
0.000000+0	0.000000+0	1.000000+0	1.000000+0	0.000000+0	0.000000+09237	2151	3436
2.000000+4	8.115570+0	0.000000+0	1.003700-3	2.281190-2	0.000000+09237	2151	3437
2.300000+4	8.061270+0	0.000000+0	9.966050-4	2.284390-2	0.000000+09237	2151	3438
2.600000+4	8.007370+0	0.000000+0	9.895700-4	2.287600-2	0.000000+09237	2151	3439
3.000000+4	7.936160+0	0.000000+0	9.802870-4	2.291910-2	0.000000+09237	2151	3440
3.500000+4	7.847940+0	0.000000+0	9.687990-4	2.297280-2	0.000000+09237	2151	3441
4.000000+4	7.760790+0	0.000000+0	9.574700-4	2.302660-2	0.000000+09237	2151	3442
4.500000+4	7.674560+0	0.000000+0	9.462760-4	2.308050-2	0.000000+09237	2151	3443
4.509020+4	7.673020+0	0.000000+0	9.460770-4	2.308140-2	0.000000+09237	2151	3444
5.000000+4	7.589410+0	5.101480-2	9.352400-4	2.313450-2	0.000000+09237	2151	3445
5.500000+4	7.505290+0	7.104690-2	9.243510-4	2.318890-2	0.000000+09237	2151	3446
6.000000+4	7.421970+0	8.562230-2	9.135850-4	2.324300-2	0.000000+09237	2151	3447
7.000000+4	7.258480+0	1.072040-1	8.925030-4	2.335250-2	0.000000+09237	2151	3448
8.000000+4	7.098720+0	1.232760-1	8.719630-4	2.346240-2	0.000000+09237	2151	3449
9.000000+4	6.942610+0	1.360730-1	8.519550-4	2.357300-2	0.000000+09237	2151	3450
1.000000+5	6.790090+0	1.466460-1	8.324640-4	2.368410-2	0.000000+09237	2151	3451
1.200000+5	6.495380+0	1.632850-1	7.949810-4	2.390780-2	0.000000+09237	2151	3452
1.400000+5	6.213960+0	1.758910-1	7.594130-4	2.424070-2	0.000000+09237	2151	3453
1.490288+5	6.091120+0	1.806460-1	7.439600-4	2.434410-2	0.000000+09237	2151	3454
0.000000+0	0.000000+0	0	0	0	09237	2	099999

APPENDIX E

^{238}U PROBABILITY TABLES AT 293.6 K

The normalized probability tables listed here were generated using the new URR methodology outlined in this dissertation. The normalized ^{238}U probability tables were generated at each energy of reference reported in the ENDF/B-VII.1 File-2 using 30,000 histories each. The average deviation in each bin is reported for completeness, but only the reported standard deviation for the total cross-section factor should be considered. There is no standard deviation reported on the bin probability, due to the equiprobable construction. Below the inelastic threshold of 45.0902 keV, the inelastic cross-section factor is reported as unity, with no standard deviation. This choice has no effect on the transport calculations, since the factors will be scaling a zero-valued inelastic cross section.

20 keV

Bin	P(bin)	f_{tot}	σ_{tot}	f_{cap}	σ_{cap}	f_{el}	σ_{el}	f_{inel}	σ_{inel}
1	0.05	0.46581	0.09028	0.3787	0.42985	0.46955	0.09561	1	0
2	0.05	0.60889	0.02031	0.36185	0.43649	0.6195	0.02882	1	0
3	0.05	0.66067	0.01133	0.3767	0.48709	0.67287	0.02384	1	0
4	0.05	0.69386	0.00789	0.37767	0.45043	0.70744	0.0213	1	0
5	0.05	0.72006	0.00712	0.38412	0.44524	0.73449	0.02041	1	0
6	0.05	0.74389	0.00658	0.43725	0.50497	0.75706	0.02269	1	0
7	0.05	0.7658	0.00632	0.48381	0.51962	0.77791	0.02302	1	0
8	0.05	0.78877	0.00669	0.55503	0.58578	0.79881	0.02591	1	0
9	0.05	0.81238	0.00723	0.60315	0.57626	0.82137	0.02526	1	0
10	0.05	0.83854	0.00806	0.70963	0.63982	0.84407	0.02812	1	0
11	0.05	0.86912	0.00925	0.82693	0.7399	0.87093	0.03277	1	0
12	0.05	0.90301	0.01059	1.00867	0.8078	0.89847	0.03594	1	0
13	0.05	0.94438	0.01321	1.14666	0.87326	0.93569	0.0391	1	0
14	0.05	0.99429	0.01635	1.31526	0.95296	0.9805	0.04366	1	0
15	0.05	1.05721	0.02055	1.49818	1.01228	1.03827	0.04677	1	0
16	0.05	1.13736	0.02642	1.64921	1.10643	1.11538	0.0543	1	0
17	0.05	1.24507	0.03691	1.82857	1.18464	1.22001	0.06184	1	0
18	0.05	1.40758	0.05964	1.98887	1.19674	1.38261	0.08077	1	0
19	0.05	1.69683	0.11685	2.1044	1.28743	1.67932	0.13358	1	0
20	0.05	2.64647	0.71203	1.96535	1.19089	2.67573	0.74389	1	0

23 keV

Bin	P(bin)	f_{tot}	σ_{tot}	f_{cap}	σ_{cap}	f_{el}	σ_{el}	f_{inel}	σ_{inel}
1	0.05	0.45028	0.08347	0.43846	0.39977	0.45084	0.08811	1	0
2	0.05	0.5866	0.02153	0.45719	0.42565	0.59269	0.03046	1	0
3	0.05	0.64541	0.01351	0.46547	0.44489	0.65387	0.02519	1	0
4	0.05	0.6852	0.01003	0.47802	0.46572	0.69494	0.02437	1	0
5	0.05	0.71593	0.00778	0.47	0.45334	0.7275	0.02271	1	0
6	0.05	0.74144	0.00723	0.53017	0.49234	0.75137	0.02385	1	0
7	0.05	0.76612	0.00708	0.53725	0.5086	0.77688	0.02517	1	0
8	0.05	0.7901	0.00678	0.60326	0.53462	0.79889	0.02567	1	0
9	0.05	0.81488	0.00735	0.67902	0.54088	0.82126	0.02602	1	0
10	0.05	0.84134	0.00808	0.79368	0.58792	0.84358	0.02855	1	0
11	0.05	0.87218	0.00981	0.88567	0.61504	0.87154	0.02972	1	0
12	0.05	0.90863	0.01167	1.00196	0.68268	0.90424	0.03386	1	0
13	0.05	0.95253	0.01386	1.18703	0.73989	0.9415	0.0363	1	0
14	0.05	1.00446	0.01704	1.31986	0.77513	0.98963	0.04027	1	0
15	0.05	1.0677	0.02054	1.45554	0.83858	1.04947	0.0448	1	0
16	0.05	1.14893	0.02615	1.57589	0.87139	1.12885	0.04855	1	0
17	0.05	1.26145	0.03845	1.7206	0.95047	1.23985	0.05921	1	0
18	0.05	1.42798	0.05961	1.81387	0.98962	1.40984	0.07745	1	0
19	0.05	1.72803	0.12588	1.8276	1.01792	1.72335	0.13935	1	0
20	0.05	2.59081	0.59834	1.75947	0.97066	2.62991	0.6291	1	0

26 keV

Bin	P(bin)	f_{tot}	σ_{tot}	f_{cap}	σ_{cap}	f_{el}	σ_{el}	f_{inel}	σ_{inel}
1	0.05	0.4647	0.08271	0.44386	0.37954	0.46568	0.08783	1	0
2	0.05	0.60042	0.02176	0.4864	0.43251	0.60575	0.03065	1	0
3	0.05	0.65924	0.0128	0.45906	0.41794	0.66858	0.02361	1	0
4	0.05	0.69666	0.00932	0.49797	0.45342	0.70594	0.0234	1	0
5	0.05	0.72623	0.00788	0.50521	0.44606	0.73655	0.02268	1	0
6	0.05	0.75245	0.00739	0.54551	0.48501	0.76211	0.02368	1	0
7	0.05	0.77761	0.0072	0.58579	0.50033	0.78657	0.02433	1	0
8	0.05	0.80204	0.00729	0.64059	0.51066	0.80958	0.02476	1	0
9	0.05	0.82876	0.00803	0.74324	0.55547	0.83275	0.02692	1	0
10	0.05	0.85733	0.00871	0.81654	0.57283	0.85923	0.02783	1	0
11	0.05	0.8901	0.0099	0.91287	0.60894	0.88904	0.02978	1	0
12	0.05	0.92619	0.0115	1.06576	0.69067	0.91967	0.03376	1	0
13	0.05	0.96984	0.01419	1.13326	0.7242	0.96221	0.03685	1	0
14	0.05	1.0215	0.01571	1.28728	0.77331	1.00909	0.03899	1	0
15	0.05	1.08356	0.02037	1.41644	0.82175	1.06802	0.04387	1	0
16	0.05	1.16434	0.02556	1.54031	0.8736	1.14679	0.04852	1	0
17	0.05	1.26521	0.03441	1.67226	0.88186	1.2462	0.05392	1	0
18	0.05	1.41182	0.05357	1.76669	0.97626	1.39525	0.07058	1	0
19	0.05	1.67519	0.10479	1.81407	1.03745	1.6687	0.12011	1	0
20	0.05	2.42681	0.51988	1.66688	0.94207	2.4623	0.54716	1	0

30 keV

Bin	P(bin)	f_{tot}	σ_{tot}	f_{cap}	σ_{cap}	f_{el}	σ_{el}	f_{inel}	σ_{inel}
1	0.05	0.47588	0.0849	0.49096	0.41148	0.47521	0.08879	1	0
2	0.05	0.61365	0.02127	0.51036	0.42152	0.61821	0.02859	1	0
3	0.05	0.67382	0.01335	0.51003	0.40618	0.68105	0.02271	1	0
4	0.05	0.71289	0.00988	0.50874	0.40717	0.7219	0.02079	1	0
5	0.05	0.74327	0.00794	0.55077	0.46478	0.75176	0.02219	1	0
6	0.05	0.76986	0.0075	0.59305	0.49179	0.77767	0.02286	1	0
7	0.05	0.79565	0.00714	0.62044	0.47119	0.80339	0.0221	1	0
8	0.05	0.8204	0.00734	0.68843	0.49431	0.82623	0.02324	1	0
9	0.05	0.84692	0.00797	0.79021	0.54499	0.84943	0.02476	1	0
10	0.05	0.87452	0.0085	0.84868	0.57221	0.87566	0.02647	1	0
11	0.05	0.90606	0.00978	0.95135	0.59998	0.90406	0.02822	1	0
12	0.05	0.94265	0.01175	1.05952	0.62377	0.9375	0.02933	1	0
13	0.05	0.98572	0.01311	1.1986	0.67725	0.97633	0.03217	1	0
14	0.05	1.03523	0.01523	1.27415	0.70452	1.02469	0.03345	1	0
15	0.05	1.09398	0.01849	1.39196	0.75398	1.08082	0.03714	1	0
16	0.05	1.16591	0.02343	1.46836	0.7971	1.15256	0.04285	1	0
17	0.05	1.25967	0.03211	1.53979	0.81798	1.24731	0.04893	1	0
18	0.05	1.394	0.0476	1.63986	0.8573	1.38315	0.0626	1	0
19	0.05	1.61958	0.0897	1.68057	0.92178	1.61689	0.1011	1	0
20	0.05	2.27033	0.46963	1.68416	0.92793	2.2962	0.49301	1	0

35 keV

Bin	P(bin)	f_{tot}	σ_{tot}	f_{cap}	σ_{cap}	f_{el}	σ_{el}	f_{inel}	σ_{inel}
1	0.05	0.50442	0.08459	0.52376	0.40063	0.50362	0.08797	1	0
2	0.05	0.63831	0.02005	0.52642	0.42044	0.6429	0.02695	1	0
3	0.05	0.69345	0.01278	0.56322	0.45324	0.6988	0.02303	1	0
4	0.05	0.73268	0.00997	0.55293	0.43705	0.74006	0.02041	1	0
5	0.05	0.76402	0.00815	0.59712	0.46139	0.77087	0.02058	1	0
6	0.05	0.78987	0.00713	0.62936	0.45829	0.79645	0.02006	1	0
7	0.05	0.8144	0.00704	0.68981	0.48743	0.81951	0.02097	1	0
8	0.05	0.83862	0.0073	0.74778	0.50093	0.84235	0.02185	1	0
9	0.05	0.86484	0.00791	0.8228	0.50955	0.86657	0.02237	1	0
10	0.05	0.89256	0.00826	0.86641	0.53601	0.89363	0.02336	1	0
11	0.05	0.92345	0.00972	0.98499	0.5701	0.92093	0.02524	1	0
12	0.05	0.95889	0.01089	1.05719	0.59286	0.95486	0.02615	1	0
13	0.05	0.99826	0.01184	1.14294	0.62422	0.99233	0.02728	1	0
14	0.05	1.04234	0.01391	1.24244	0.66784	1.03413	0.03009	1	0
15	0.05	1.09664	0.01771	1.34497	0.67974	1.08645	0.03221	1	0
16	0.05	1.16267	0.02167	1.43616	0.74232	1.15145	0.03794	1	0
17	0.05	1.24917	0.0281	1.50284	0.74022	1.23876	0.04147	1	0
18	0.05	1.36839	0.04273	1.56744	0.78097	1.36022	0.05321	1	0
19	0.05	1.56392	0.07523	1.58032	0.7924	1.56324	0.0853	1	0
20	0.05	2.10312	0.35684	1.62111	0.83464	2.12289	0.37302	1	0

40 keV

Bin	P(bin)	f_{tot}	σ_{tot}	f_{cap}	σ_{cap}	f_{el}	σ_{el}	f_{inel}	σ_{inel}
1	0.05	0.52045	0.08063	0.57608	0.41971	0.51833	0.08357	1	0
2	0.05	0.6484	0.02044	0.58334	0.42363	0.65088	0.02711	1	0
3	0.05	0.70372	0.01278	0.59883	0.43969	0.70772	0.02176	1	0
4	0.05	0.74224	0.00942	0.59785	0.41893	0.74775	0.01888	1	0
5	0.05	0.77206	0.00783	0.63941	0.43623	0.77712	0.01837	1	0
6	0.05	0.79876	0.00739	0.66743	0.46333	0.80377	0.01888	1	0
7	0.05	0.82392	0.00721	0.71524	0.46155	0.82807	0.0191	1	0
8	0.05	0.84874	0.00732	0.77831	0.47527	0.85142	0.01947	1	0
9	0.05	0.87547	0.0079	0.87226	0.53313	0.87559	0.0216	1	0
10	0.05	0.90385	0.00849	0.92377	0.52247	0.90309	0.02158	1	0
11	0.05	0.93486	0.00921	1.00941	0.54044	0.93201	0.02253	1	0
12	0.05	0.96844	0.01032	1.07436	0.56288	0.9644	0.02392	1	0
13	0.05	1.00711	0.01158	1.14794	0.57286	1.00174	0.0245	1	0
14	0.05	1.0499	0.01382	1.21495	0.60829	1.0436	0.02716	1	0
15	0.05	1.10227	0.01628	1.27746	0.61249	1.09559	0.0279	1	0
16	0.05	1.1634	0.01916	1.3372	0.64795	1.15677	0.03186	1	0
17	0.05	1.24234	0.0272	1.42029	0.68584	1.23555	0.03802	1	0
18	0.05	1.35135	0.03776	1.47614	0.66226	1.34659	0.04609	1	0
19	0.05	1.53227	0.06884	1.50651	0.68662	1.53326	0.0759	1	0
20	0.05	2.01046	0.32784	1.58322	0.75237	2.02676	0.34038	1	0

45 keV

Bin	P(bin)	f_{tot}	σ_{tot}	f_{cap}	σ_{cap}	f_{el}	σ_{el}	f_{inel}	σ_{inel}
1	0.05	0.53935	0.08227	0.64788	0.46423	0.53534	0.08228	1	0
2	0.05	0.66657	0.02533	0.66186	0.46931	0.66675	0.02057	1	0
3	0.05	0.71929	0.02095	0.65815	0.48101	0.72155	0.01189	1	0
4	0.05	0.75445	0.01893	0.67816	0.46619	0.75728	0.00915	1	0
5	0.05	0.78494	0.0203	0.73313	0.52217	0.78686	0.0077	1	0
6	0.05	0.81027	0.019	0.73462	0.49082	0.81307	0.00711	1	0
7	0.05	0.83568	0.01944	0.7796	0.50577	0.83775	0.0071	1	0
8	0.05	0.86197	0.01972	0.83585	0.51263	0.86293	0.0074	1	0
9	0.05	0.88695	0.02026	0.85206	0.52611	0.88824	0.0074	1	0
10	0.05	0.91574	0.0216	0.93743	0.55985	0.91494	0.00783	1	0
11	0.05	0.94597	0.02247	1.01029	0.57054	0.94359	0.00884	1	0
12	0.05	0.97775	0.02206	1.05773	0.55078	0.9748	0.00939	1	0
13	0.05	1.01296	0.02314	1.09712	0.56964	1.00985	0.01107	1	0
14	0.05	1.05553	0.02478	1.16809	0.58269	1.05137	0.01299	1	0
15	0.05	1.10624	0.02782	1.2417	0.61178	1.10123	0.01589	1	0
16	0.05	1.16586	0.0292	1.26811	0.624	1.16208	0.01917	1	0
17	0.05	1.2403	0.03384	1.31747	0.62786	1.23745	0.02476	1	0
18	0.05	1.3406	0.04306	1.40579	0.67738	1.33819	0.0348	1	0
19	0.05	1.49167	0.06416	1.41762	0.65653	1.49441	0.06152	1	0
20	0.05	1.88789	0.28106	1.49732	0.70141	1.90233	0.28929	1	0

45.0902 keV

Bin	P(bin)	f_{tot}	σ_{tot}	f_{cap}	σ_{cap}	f_{el}	σ_{el}	f_{inel}	σ_{inel}
1	0.05	0.53842	0.08025	0.55567	0.38726	0.53778	0.08321	1.00431	0.0855
2	0.05	0.66426	0.01992	0.60325	0.43189	0.6665	0.02584	1.00255	0.08399
3	0.05	0.71724	0.01214	0.60328	0.41363	0.72143	0.01943	0.99597	0.08665
4	0.05	0.75474	0.00967	0.61585	0.41085	0.75985	0.01794	1.00088	0.08535
5	0.05	0.7842	0.00779	0.67051	0.4609	0.78837	0.01879	1.00199	0.08558
6	0.05	0.81105	0.0078	0.70399	0.45416	0.81498	0.01827	0.99874	0.08571
7	0.05	0.83625	0.00693	0.75532	0.4643	0.83922	0.0181	1.00222	0.08356
8	0.05	0.86099	0.00744	0.84793	0.48869	0.86147	0.01926	1.00202	0.0855
9	0.05	0.88786	0.00801	0.8815	0.49224	0.88809	0.01934	0.99953	0.08453
10	0.05	0.91567	0.00811	0.94075	0.50231	0.91475	0.02011	1.00155	0.08507
11	0.05	0.94567	0.00922	1.02205	0.52407	0.94286	0.02131	0.99944	0.08643
12	0.05	0.97981	0.0102	1.08879	0.56473	0.9758	0.02338	1.00035	0.08526
13	0.05	1.01643	0.01153	1.15818	0.57606	1.01122	0.02387	1.00131	0.08526
14	0.05	1.05817	0.01249	1.21018	0.57546	1.05258	0.02459	0.99438	0.08549
15	0.05	1.1062	0.01559	1.27289	0.60458	1.10008	0.02738	0.99674	0.08543
16	0.05	1.16427	0.01799	1.30356	0.62689	1.15915	0.02938	1.00059	0.0841
17	0.05	1.23627	0.02435	1.37621	0.60914	1.23112	0.03334	1.00105	0.08657
18	0.05	1.33604	0.03446	1.40442	0.64174	1.33353	0.04166	1.0024	0.08392
19	0.05	1.48847	0.058	1.46141	0.65023	1.48946	0.06399	0.99666	0.08519
20	0.05	1.89801	0.28969	1.52424	0.68896	1.91175	0.29971	0.99731	0.08143

50 keV

Bin	P(bin)	f_{tot}	σ_{tot}	f_{cap}	σ_{cap}	f_{el}	σ_{el}	f_{inel}	σ_{inel}
1	0.05	0.55092	0.0754	0.57288	0.38158	0.54896	0.07943	0.65388	0.45658
2	0.05	0.6746	0.01898	0.5962	0.37338	0.67675	0.02543	0.69743	0.49141
3	0.05	0.72678	0.01242	0.60778	0.4024	0.73091	0.02134	0.69284	0.50952
4	0.05	0.76402	0.00925	0.63801	0.40503	0.76834	0.01966	0.73239	0.53832
5	0.05	0.79413	0.00828	0.66824	0.40451	0.79861	0.01869	0.74902	0.49954
6	0.05	0.82159	0.00777	0.72454	0.44672	0.82475	0.01988	0.8106	0.54917
7	0.05	0.84697	0.00714	0.76724	0.42459	0.84946	0.0192	0.84629	0.57944
8	0.05	0.87188	0.00711	0.82927	0.4542	0.87357	0.01967	0.84255	0.55475
9	0.05	0.89641	0.00741	0.91714	0.47713	0.89545	0.02103	0.92204	0.61204
10	0.05	0.92333	0.00819	0.96753	0.48638	0.92101	0.02162	0.99881	0.66438
11	0.05	0.95249	0.00882	0.99905	0.4717	0.95028	0.02206	1.01338	0.63584
12	0.05	0.98434	0.00941	1.1032	0.50576	0.97906	0.02367	1.11163	0.7166
13	0.05	1.01851	0.01064	1.11323	0.50921	1.01499	0.02382	1.06419	0.68643
14	0.05	1.05943	0.01206	1.18825	0.52693	1.05414	0.02558	1.16272	0.74678
15	0.05	1.10526	0.01417	1.2352	0.52136	1.10037	0.02668	1.17261	0.75572
16	0.05	1.15803	0.01713	1.30639	0.55743	1.15275	0.02935	1.21156	0.75696
17	0.05	1.22629	0.02264	1.36758	0.57871	1.22122	0.03409	1.28034	0.81935
18	0.05	1.3214	0.03306	1.41062	0.59079	1.31878	0.04205	1.30879	0.82276
19	0.05	1.46639	0.05498	1.4736	0.60508	1.46788	0.06268	1.32853	0.8652
20	0.05	1.83722	0.25244	1.51407	0.61162	1.85272	0.26213	1.40041	0.86469

55 keV

Bin	P(bin)	f_{tot}	σ_{tot}	f_{cap}	σ_{cap}	f_{el}	σ_{el}	f_{inel}	σ_{inel}
1	0.05	0.56403	0.07569	0.59831	0.35055	0.56158	0.08073	0.63011	0.43361
2	0.05	0.68713	0.01888	0.61494	0.37795	0.69031	0.02666	0.633	0.4667
3	0.05	0.7388	0.01214	0.63156	0.36541	0.7434	0.0223	0.66437	0.46394
4	0.05	0.77497	0.00875	0.66923	0.42202	0.77985	0.02138	0.68653	0.48391
5	0.05	0.80371	0.00794	0.68953	0.39195	0.80818	0.02082	0.74311	0.51546
6	0.05	0.82942	0.0072	0.73627	0.41378	0.83304	0.02108	0.78101	0.52056
7	0.05	0.85365	0.0069	0.78125	0.42464	0.85602	0.02204	0.83507	0.54534
8	0.05	0.87851	0.00737	0.84767	0.42772	0.8797	0.02198	0.86289	0.55662
9	0.05	0.90367	0.00734	0.89522	0.42943	0.90353	0.02254	0.9193	0.58553
10	0.05	0.93023	0.00779	0.94406	0.43553	0.92947	0.02227	0.94687	0.59197
11	0.05	0.95776	0.00839	1.00901	0.45075	0.95508	0.02382	1.01407	0.62816
12	0.05	0.98914	0.00936	1.04805	0.4374	0.9859	0.0252	1.06087	0.68107
13	0.05	1.02359	0.01021	1.12755	0.47184	1.01836	0.02587	1.12925	0.68118
14	0.05	1.06165	0.01205	1.18227	0.48595	1.05592	0.02789	1.16929	0.73128
15	0.05	1.10533	0.0137	1.20192	0.49537	1.10093	0.0289	1.18347	0.71286
16	0.05	1.1582	0.0165	1.30377	0.50119	1.1524	0.03108	1.24009	0.76609
17	0.05	1.22308	0.02112	1.31598	0.52189	1.21946	0.03599	1.27187	0.8103
18	0.05	1.30767	0.02894	1.38738	0.50406	1.30492	0.04132	1.33434	0.84677
19	0.05	1.43429	0.04885	1.45902	0.56072	1.43414	0.05928	1.4122	0.88585
20	0.05	1.77517	0.23169	1.55702	0.60093	1.7878	0.24276	1.48229	0.93159

60 keV

Bin	P(bin)	f_{tot}	σ_{tot}	f_{cap}	σ_{cap}	f_{el}	σ_{el}	f_{inel}	σ_{inel}
1	0.05	0.57686	0.07153	0.60163	0.32933	0.57499	0.07658	0.61495	0.44415
2	0.05	0.69623	0.01982	0.62487	0.36468	0.70061	0.02865	0.61592	0.43663
3	0.05	0.7475	0.01141	0.64424	0.3703	0.75304	0.02423	0.65543	0.44707
4	0.05	0.78313	0.00915	0.67307	0.37929	0.78998	0.02297	0.65678	0.45791
5	0.05	0.81207	0.00804	0.72305	0.39777	0.8173	0.02378	0.71916	0.49616
6	0.05	0.83801	0.00711	0.74232	0.39062	0.84315	0.02322	0.75254	0.4943
7	0.05	0.8623	0.00711	0.81362	0.39609	0.86524	0.02405	0.80885	0.51347
8	0.05	0.88693	0.00707	0.86936	0.40898	0.88905	0.02332	0.83593	0.49134
9	0.05	0.91133	0.00735	0.89787	0.41313	0.91168	0.02474	0.91069	0.54178
10	0.05	0.9368	0.00752	0.96748	0.40656	0.93469	0.02543	0.97792	0.57882
11	0.05	0.96345	0.00792	1.01176	0.4296	0.96085	0.027	1.00659	0.60672
12	0.05	0.99234	0.00877	1.05949	0.43563	0.98793	0.02896	1.07627	0.65899
13	0.05	1.0242	0.00978	1.10957	0.41895	1.01955	0.02863	1.10245	0.65386
14	0.05	1.061	0.01145	1.15936	0.463	1.05572	0.03125	1.14879	0.69088
15	0.05	1.10356	0.0136	1.21471	0.47174	1.09744	0.03204	1.20725	0.68379
16	0.05	1.15284	0.01565	1.27377	0.47588	1.14637	0.0351	1.25983	0.76308
17	0.05	1.21323	0.01928	1.30834	0.47499	1.20791	0.03783	1.30449	0.78249
18	0.05	1.29574	0.02845	1.35726	0.49135	1.29167	0.04625	1.37362	0.82511
19	0.05	1.41882	0.04557	1.41689	0.51368	1.41826	0.0586	1.43728	0.87946
20	0.05	1.72366	0.21148	1.53134	0.54802	1.73455	0.22373	1.53527	0.93603

70 keV

Bin	P(bin)	f_{tot}	σ_{tot}	f_{cap}	σ_{cap}	f_{el}	σ_{el}	f_{inel}	σ_{inel}
1	0.05	0.60427	0.07041	0.64391	0.32602	0.60386	0.0773	0.59621	0.37015
2	0.05	0.71523	0.01738	0.68307	0.36678	0.72117	0.03137	0.61214	0.38456
3	0.05	0.76391	0.01145	0.69279	0.37157	0.7722	0.02871	0.6306	0.41427
4	0.05	0.79795	0.00824	0.7148	0.37603	0.80625	0.02654	0.66927	0.41896
5	0.05	0.82499	0.00752	0.74621	0.37216	0.83295	0.02746	0.70113	0.43483
6	0.05	0.84921	0.00664	0.78423	0.36095	0.8549	0.02709	0.76444	0.44378
7	0.05	0.87237	0.00688	0.82186	0.3735	0.87777	0.02757	0.78723	0.44702
8	0.05	0.8959	0.00679	0.87644	0.37763	0.89936	0.02824	0.83613	0.47409
9	0.05	0.91944	0.00714	0.90817	0.38683	0.92101	0.02893	0.89324	0.48203
10	0.05	0.9444	0.00742	0.95753	0.39219	0.94333	0.0305	0.96005	0.51133
11	0.05	0.97069	0.00809	0.99265	0.39391	0.96927	0.031	0.98942	0.5269
12	0.05	0.99849	0.00803	1.0366	0.3759	0.99398	0.03198	1.07115	0.55183
13	0.05	1.02791	0.00893	1.09233	0.41194	1.02361	0.03483	1.08588	0.59568
14	0.05	1.06029	0.01001	1.11623	0.38575	1.05472	0.03525	1.14655	0.60795
15	0.05	1.09986	0.01232	1.17002	0.41019	1.09453	0.0377	1.17558	0.63083
16	0.05	1.14583	0.01474	1.24173	0.40795	1.13751	0.04067	1.26974	0.66632
17	0.05	1.20107	0.01787	1.2647	0.42302	1.19404	0.04298	1.31283	0.70048
18	0.05	1.27349	0.0236	1.33382	0.43242	1.26572	0.04765	1.40113	0.76544
19	0.05	1.38197	0.0415	1.40224	0.46362	1.37708	0.06217	1.46925	0.79944
20	0.05	1.65273	0.1868	1.52069	0.47031	1.65674	0.20199	1.62802	0.88501

80 keV

Bin	P(bin)	f_{tot}	σ_{tot}	f_{cap}	σ_{cap}	f_{el}	σ_{el}	f_{inel}	σ_{inel}
1	0.05	0.61619	0.06675	0.66234	0.32806	0.61757	0.07521	0.58183	0.3674
2	0.05	0.72803	0.01668	0.69044	0.35362	0.73606	0.03238	0.61367	0.37671
3	0.05	0.77413	0.011	0.69023	0.35341	0.78574	0.03056	0.61701	0.3829
4	0.05	0.80738	0.00825	0.73475	0.37649	0.8167	0.03001	0.68274	0.39262
5	0.05	0.83353	0.00708	0.77002	0.38514	0.84245	0.03088	0.71261	0.41473
6	0.05	0.85789	0.00688	0.78877	0.36528	0.86621	0.02992	0.74778	0.40783
7	0.05	0.88105	0.00669	0.82759	0.3736	0.88836	0.03077	0.7823	0.42326
8	0.05	0.90395	0.00652	0.89384	0.39693	0.90815	0.03172	0.84142	0.44246
9	0.05	0.92609	0.00626	0.91448	0.38695	0.92911	0.03249	0.88224	0.46387
10	0.05	0.94899	0.00674	0.9501	0.38274	0.95032	0.03446	0.92795	0.48781
11	0.05	0.97324	0.00714	0.99692	0.39187	0.97374	0.03359	0.95882	0.47935
12	0.05	0.99956	0.00774	1.03823	0.39514	0.99601	0.03771	1.044	0.53655
13	0.05	1.02863	0.00883	1.09118	0.40458	1.02347	0.03832	1.09135	0.54543
14	0.05	1.06046	0.00978	1.13544	0.42776	1.05334	0.03967	1.15009	0.57235
15	0.05	1.09682	0.01143	1.16808	0.4229	1.08896	0.04366	1.19914	0.61258
16	0.05	1.14064	0.01377	1.22418	0.46096	1.13266	0.04426	1.24122	0.61412
17	0.05	1.19253	0.0163	1.26287	0.42938	1.18173	0.04862	1.34092	0.67529
18	0.05	1.2594	0.02272	1.30863	0.43626	1.24917	0.05257	1.4048	0.70026
19	0.05	1.35835	0.03641	1.36915	0.44856	1.34871	0.0645	1.50541	0.7747
20	0.05	1.61313	0.17276	1.48277	0.48334	1.61153	0.18745	1.67469	0.855

90 keV

Bin	P(bin)	f_{tot}	σ_{tot}	f_{cap}	σ_{cap}	f_{el}	σ_{el}	f_{inel}	σ_{inel}
1	0.05	0.63706	0.06491	0.67515	0.35804	0.64158	0.07453	0.56819	0.34261
2	0.05	0.74089	0.01708	0.71449	0.41257	0.75127	0.03518	0.60769	0.36274
3	0.05	0.78621	0.01046	0.73284	0.36163	0.79749	0.03072	0.64694	0.36313
4	0.05	0.81749	0.00807	0.75257	0.35368	0.83106	0.02987	0.64998	0.35322
5	0.05	0.84341	0.00711	0.78112	0.36419	0.85625	0.03113	0.68513	0.37476
6	0.05	0.86729	0.0065	0.82664	0.36038	0.87609	0.03308	0.75837	0.40048
7	0.05	0.88896	0.00635	0.85658	0.35836	0.8959	0.03398	0.80317	0.41419
8	0.05	0.9107	0.00643	0.8834	0.35803	0.91674	0.03324	0.8359	0.41273
9	0.05	0.93306	0.00636	0.92255	0.36319	0.93795	0.0339	0.86985	0.41994
10	0.05	0.95568	0.00654	0.954	0.3645	0.95601	0.03695	0.95171	0.46235
11	0.05	0.9791	0.00697	0.99981	0.38865	0.97948	0.03753	0.96946	0.46962
12	0.05	1.00417	0.00724	1.03474	0.35913	1.00024	0.03878	1.05007	0.48934
13	0.05	1.03036	0.00786	1.07559	0.38577	1.02558	0.03937	1.08447	0.49968
14	0.05	1.0599	0.00922	1.11038	0.39264	1.05315	0.04075	1.13915	0.51483
15	0.05	1.09287	0.01027	1.12919	0.36661	1.08415	0.04322	1.20171	0.54356
16	0.05	1.13162	0.01251	1.20313	0.40996	1.1215	0.04722	1.25148	0.5848
17	0.05	1.18154	0.01625	1.23217	0.41747	1.16877	0.05124	1.34146	0.62313
18	0.05	1.245	0.02153	1.2953	0.46629	1.23254	0.05568	1.40082	0.66743
19	0.05	1.33811	0.03262	1.35449	0.44862	1.32608	0.06243	1.49567	0.68709
20	0.05	1.55657	0.15068	1.46586	0.42157	1.54819	0.16998	1.68876	0.79393

100 keV

Bin	P(bin)	f_{tot}	σ_{tot}	f_{cap}	σ_{cap}	f_{el}	σ_{el}	f_{inel}	σ_{inel}
1	0.05	0.65297	0.0598	0.6936	0.37592	0.65869	0.07019	0.57671	0.34401
2	0.05	0.74996	0.01585	0.72221	0.34707	0.76252	0.03486	0.60349	0.33768
3	0.05	0.79335	0.01048	0.73443	0.34101	0.80686	0.03348	0.64092	0.36256
4	0.05	0.82415	0.00783	0.75743	0.35268	0.83862	0.03135	0.66146	0.34384
5	0.05	0.84999	0.00695	0.79972	0.37078	0.86269	0.03324	0.70569	0.36666
6	0.05	0.87298	0.00633	0.80919	0.35475	0.88456	0.03423	0.74459	0.37978
7	0.05	0.89458	0.00621	0.86311	0.36033	0.90335	0.03449	0.79429	0.38755
8	0.05	0.91562	0.00587	0.8985	0.37755	0.92321	0.03516	0.82711	0.39221
9	0.05	0.93671	0.00634	0.93778	0.36603	0.94085	0.03589	0.8866	0.41069
10	0.05	0.95893	0.00655	0.97417	0.3648	0.95881	0.03792	0.95772	0.43342
11	0.05	0.9813	0.0062	0.98069	0.35407	0.98079	0.03949	0.98754	0.44927
12	0.05	1.00413	0.00709	1.02249	0.35997	1.0018	0.03953	1.02894	0.45212
13	0.05	1.02923	0.00774	1.05462	0.36771	1.02423	0.04222	1.085	0.48391
14	0.05	1.05773	0.00848	1.11481	0.37956	1.04848	0.04449	1.15925	0.51857
15	0.05	1.0899	0.01022	1.14618	0.42299	1.08138	0.04462	1.18264	0.50743
16	0.05	1.1288	0.01188	1.18533	0.39491	1.11838	0.04759	1.24447	0.54042
17	0.05	1.17365	0.01408	1.22103	0.3997	1.16114	0.0506	1.31605	0.57457
18	0.05	1.23153	0.01955	1.28343	0.43867	1.21467	0.05737	1.42575	0.62728
19	0.05	1.31907	0.03374	1.34746	0.41248	1.30528	0.06508	1.48038	0.64397
20	0.05	1.53541	0.14444	1.45382	0.45205	1.52369	0.16277	1.6914	0.75641

120 keV

Bin	P(bin)	f_{tot}	σ_{tot}	f_{cap}	σ_{cap}	f_{el}	σ_{el}	f_{inel}	σ_{inel}
1	0.05	0.6797	0.05974	0.72957	0.32624	0.68957	0.07159	0.56966	0.29822
2	0.05	0.77242	0.01414	0.75293	0.32745	0.78701	0.03496	0.62239	0.31607
3	0.05	0.81216	0.00942	0.78758	0.43721	0.82652	0.03432	0.66521	0.3234
4	0.05	0.84007	0.0072	0.7919	0.35986	0.8563	0.0348	0.67671	0.33289
5	0.05	0.86371	0.00641	0.82006	0.33914	0.87627	0.03539	0.73822	0.34625
6	0.05	0.88534	0.00586	0.84673	0.3411	0.89819	0.03439	0.75602	0.33792
7	0.05	0.9052	0.00542	0.86956	0.34564	0.91462	0.03595	0.81147	0.36016
8	0.05	0.92458	0.00574	0.89925	0.34631	0.93268	0.03743	0.84327	0.37409
9	0.05	0.94453	0.00573	0.94213	0.35845	0.94876	0.0397	0.90062	0.39734
10	0.05	0.96476	0.00594	0.96476	0.35489	0.96665	0.03926	0.94499	0.39482
11	0.05	0.98528	0.00593	1.00452	0.36904	0.98502	0.03977	0.98537	0.40238
12	0.05	1.00659	0.00634	1.04122	0.36724	1.00189	0.04204	1.05115	0.42413
13	0.05	1.03012	0.00733	1.04235	0.35376	1.02728	0.04328	1.05824	0.43665
14	0.05	1.05606	0.0077	1.08908	0.35402	1.04962	0.04345	1.11894	0.43825
15	0.05	1.08526	0.00916	1.10353	0.35774	1.07504	0.04917	1.18972	0.49119
16	0.05	1.11886	0.01016	1.15708	0.38722	1.10636	0.04983	1.24449	0.49771
17	0.05	1.15784	0.01255	1.2026	0.41656	1.143	0.05262	1.30704	0.52297
18	0.05	1.21064	0.01727	1.23429	0.56827	1.19479	0.05746	1.37325	0.56952
19	0.05	1.28787	0.02775	1.30161	0.42249	1.26819	0.06386	1.49199	0.59858
20	0.05	1.46902	0.12262	1.41923	0.4436	1.45225	0.14101	1.65126	0.6534

140 keV

Bin	P(bin)	f_{tot}	σ_{tot}	f_{cap}	σ_{cap}	f_{el}	σ_{el}	f_{inel}	σ_{inel}
1	0.05	0.70395	0.05486	0.76082	0.44022	0.71421	0.06826	0.59943	0.29013
2	0.05	0.78671	0.01279	0.78968	0.4798	0.80296	0.03752	0.63078	0.30825
3	0.05	0.82306	0.00882	0.79589	0.37986	0.8403	0.03587	0.66112	0.31101
4	0.05	0.85023	0.00723	0.80639	0.40878	0.86593	0.03719	0.70486	0.3291
5	0.05	0.8728	0.0059	0.84432	0.39538	0.88507	0.03689	0.75859	0.33401
6	0.05	0.89286	0.0056	0.84547	0.33448	0.90598	0.03672	0.77254	0.33208
7	0.05	0.91224	0.00553	0.87571	0.33833	0.92179	0.03747	0.82492	0.3432
8	0.05	0.93074	0.00534	0.89603	0.34017	0.93985	0.03679	0.84742	0.33737
9	0.05	0.94976	0.00554	0.93235	0.34354	0.95455	0.04005	0.90587	0.36613
10	0.05	0.96887	0.00552	0.95819	0.36384	0.97224	0.0398	0.9378	0.36528
11	0.05	0.98816	0.00564	0.99488	0.34651	0.9873	0.04198	0.99556	0.3864
12	0.05	1.00757	0.00576	1.02212	0.40975	1.00448	0.04201	1.03552	0.39029
13	0.05	1.02946	0.00657	1.04093	0.39741	1.02591	0.04362	1.06219	0.40478
14	0.05	1.05255	0.00723	1.06713	0.39185	1.04464	0.04505	1.12657	0.41725
15	0.05	1.07884	0.00815	1.09966	0.43223	1.06866	0.04741	1.17396	0.43272
16	0.05	1.10942	0.00959	1.13997	0.38459	1.09892	0.0495	1.20651	0.45622
17	0.05	1.14646	0.01209	1.18692	0.41731	1.13081	0.05211	1.29169	0.48043
18	0.05	1.19467	0.01652	1.22442	0.40726	1.1781	0.05497	1.34988	0.49761
19	0.05	1.26559	0.02547	1.29228	0.49463	1.24344	0.06263	1.47464	0.53712
20	0.05	1.43607	0.11418	1.42684	0.83492	1.41486	0.13651	1.64015	0.61868

149.0288 keV

Bin	P(bin)	f_{tot}	σ_{tot}	f_{cap}	σ_{cap}	f_{el}	σ_{el}	f_{inel}	σ_{inel}
1	0.05	0.71231	0.05576	0.80047	0.51125	0.72166	0.06919	0.61537	0.30125
2	0.05	0.79432	0.01209	0.77725	0.35588	0.8115	0.03629	0.63471	0.29906
3	0.05	0.82869	0.00803	0.77866	0.336	0.84733	0.03628	0.65865	0.31524
4	0.05	0.85424	0.00659	0.79666	0.3496	0.87126	0.03445	0.70023	0.3032
5	0.05	0.87566	0.00588	0.81869	0.35212	0.89187	0.03387	0.72911	0.30255
6	0.05	0.89526	0.00545	0.83726	0.32199	0.90977	0.03552	0.76487	0.32106
7	0.05	0.91432	0.00538	0.89595	0.50708	0.92489	0.0371	0.81688	0.33247
8	0.05	0.93289	0.00514	0.90241	0.33481	0.93909	0.03807	0.87774	0.3402
9	0.05	0.95081	0.00532	0.94467	0.36975	0.95462	0.03897	0.91565	0.35152
10	0.05	0.96929	0.0054	0.96029	0.3617	0.97201	0.03912	0.94465	0.35281
11	0.05	0.98809	0.00561	0.99082	0.45127	0.98762	0.0401	0.99225	0.3658
12	0.05	1.00784	0.00603	1.00983	0.35528	1.00296	0.04338	1.05345	0.39285
13	0.05	1.02933	0.00643	1.04511	0.41198	1.0252	0.04329	1.06657	0.38986
14	0.05	1.0519	0.00701	1.08624	0.41355	1.0433	0.04575	1.12914	0.4127
15	0.05	1.07718	0.00758	1.09492	0.38984	1.06689	0.04665	1.17213	0.42357
16	0.05	1.10642	0.00945	1.12171	0.3698	1.09318	0.04967	1.22928	0.45043
17	0.05	1.143	0.01172	1.18303	0.46142	1.12875	0.05013	1.27288	0.45176
18	0.05	1.18888	0.01527	1.21881	0.59397	1.17271	0.05585	1.33775	0.49056
19	0.05	1.25676	0.02552	1.29099	0.56827	1.23531	0.06373	1.45476	0.53498
20	0.05	1.4228	0.11216	1.44625	0.98706	1.40008	0.13471	1.63393	0.60232

REFERENCES

- [1] DUNN, M.E. and GREENE, N.M., AMPX-2000: “A Cross-Section Processing System for Generating Nuclear Data for Criticality Safety Applications,” *Trans. Am. Nucl. Soc.* (2002).
- [2] LEAL, L. C. and HWANG, R., “A Finite Difference Method for Treating the Doppler Broadening of Neutron Cross Sections,” in *American Nuclear Society*, (Los Angeles, CA), Nov. 1987.
- [3] LANE, A. M. Lane and THOMAS, R. G., “R-Matrix Theory of Nuclear Reactions,” *Rev. Mod. Phys.* **30**, 257 (1958).
- [4] LARSON, N. M., “Updated Users’ Guide for SAMMY: Multilevel R-Matrix Fits to Neutron Data Using Bayes’ Equations,” ORNL/TM-9179/R8, Oak Ridge National Laboratory, Oak Ridge, TN, USA (2008).
- [5] Fröhner, F. H., “Applied Neutron Resonance Theory,” reprinted from “Nuclear Theory for Applications,” p. 59 ff., International Centre for Theoretical Physics, Trieste (1980). Available as KFK 2669 (1978).
- [6] FODERARO, A., *The Elements of Neutron Interaction Theory*, MIT Press, 1971.
- [7] CACUCI, D. G. *Handbook of Nuclear Engineering*. New York London: Springer, 2010. Print.
- [8] BLATT, J. M. and BIEDENHARN, L. C., “The Angular Distribution of Scattering and Reaction Cross Sections,” *Rev. Mod. Phys.* **24**, 258 (1952).
- [9] DUDERSTADT, J. J., and HAMILTON, L. J., *Nuclear Reactor Analysis*. New York: Wiley, 1976. Print.
- [10] LARSON, N. M., MOXON, M. C., LEAL, L. C., and DERRIEN, H., “Doppler Broadening Revisited,” ORNL/TM-13525, Oak Ridge National Laboratory, 1998.
- [11] MANDL, F. *Statistical Physics*. Chichester West Sussex New York: Wiley, 1988. Print.

- [12] LAMB, W. E., "Capture of Neutrons by Atoms in a Crystal," *Phys. Rev.* **55** (1939) 190.
- [13] DUNN, M. E. and LEAL, L. C., "Calculating Probability Tables for the Unresolved-Resonance Region Using Monte Carlo Methods," Proceedings of the International Conference on the New Frontiers of Nuclear Technology: Reactor Physics, Safety and High Performance Computing (PHYSOR 2002), Seoul, Korea, October 7-10, 2002.
- [14] LEVITT, L. B., "The Probability Table Method for Treating Unresolved Neutron Resonances in Monte Carlo Calculations," *Nucl. Sci. Eng.*, **49**, pp. 450-457 (1972).
- [15] TRKOY, A., HERMAN, M., and BROWN, D., "ENDF-6 Formats Manual," tech. rep., Report BNL-90365-2009 Rev. 2, Brookhaven National Laboratory, Upton, New York, 2011.
- [16] DYSON, F. J. and MEHTA, M. L., "Statistical Theory of the Energy Levels of Complex Systems," *J. Math. Phys.* **4**, 701 (May 1963).
- [17] HUTCHINS, B. A. et al., "ENDRUN-II, A Computer Code to Generate a Generalized Multigroup Data File from ENDF/B," GEAP-13704 (ENDF-145), General Electric Company, Sunnyvale, California (1971).
- [18] MACFARLANE, R.E. and MUIR, D.W., "NJOY99.0 - Code System for Producing Pointwise and Multigroup Neutron and Photon Cross Sections from ENDF/B Data," PSR-480/NJOY99.00, Los Alamos National Laboratory, Los Alamos (2000).
- [19] CULLEN, D. E., WEISBIN, C. R., WRIGHT, R. Q., and WHITE, J. E., "Comparison of Doppler Broadening Methods," *SP42*, 392-397, Oct. 1975.
- [20] BOULAND, O., BABUT, R., and LARSON, N. M., "SAMQUA - A Program for Generating All Possible Combinations of Quantum Numbers Leading to the Same Compound Nucleus State in the Framework of the R-Matrix Code SAMMY," JEF-DOC 929 OECD/NEA Publications (2003) and ENDF-363 (October 2003).
- [21] DUNN, M. E. and GREENE, N. M. "POLIDENT: A Module for Generating Continuous-Energy Cross Sections from ENDF Resonance Data," ORNL/TM-2000-035, Oak Ridge National Laboratory, 2000.

- [22] HART, S. W. D., “Automated Doppler Broadening of Cross Sections for Neutron Transport Applications. “ PhD diss., University of Tennessee, 2014.
http://trace.tennessee.edu/utk_graddiss/3136
- [23] BETHE, H. A. and PLACZEK, G., “Resonance Effects in Nuclear Processes,” *Phys. Rev.* **51**, 450 (1937).
- [24] SUTTON, T. M. and BROWN, F. B., “Implementation of the Probability Table Method in a Continuous-Energy Monte Carlo Code System,” International Conference on the Physics of Nuclear Science and Technology, vol. 2, p. 891, Long Island, New York, October 5-8, 1998.
- [25] LEAL, L. C., Oak Ridge National Laboratory, private communication, 2013.
- [26] LEAL, L. C., Oak Ridge National Laboratory, private communication, 2014.
- [27] DUNFORD, C. L. and BURROWS, T. W., “Online Nuclear Data Service,” Report **IAEA-NDS-150** (NNDC Informal Report NNDC/ONL-95/10), Rev. 95/10 (1995), International Atomic Energy Agency, Vienna, Austria.
- [28] “INTERNATIONAL HANDBOOK OF EVALUATED CRITICALITY SAFETY BENCHMARK EXPERIMENTS,” NEA/NSC/DOC(95)03/I-VIII, OECD-NEA, September, 2004.
- [29] NOURI, A., NAGEL, P., BRIGGS, J. B., AND IVANOVA, T., “DICE: Database for the International Criticality Safety Benchmark Evaluation Program Handbook,” *Nucl. Sci. Eng.*, **145**, 11 (2003).
- [30] *SCALE: A Modular Code System for Performing Standardized Computer Analyses for Licensing Evaluations*, ORNL/TM-2005/39, Version 6, Vols. I–III, January 2009. Available from Radiation Safety Information Computational Center at Oak Ridge National Laboratory as CCC-750.
- [31] REARDEN, B. T., MUELLER, D. E., BOWMAN, S. M., BUSCH, R. D., and EMERSON, S. J., *TSUNAMI Primer: A Primer for Sensitivity/Uncertainty Calculations with SCALE*, ORNL/TM-2009/027, Oak Ridge National Laboratory, Oak Ridge, Tenn., January 2009.

VITA

ANDREW M. HOLCOMB

Andrew Michael Holcomb was born in 1990 to Kelli and William Holcomb. He grew up in Hillsborough County, Florida with his three younger sisters, Sara, Hannah, and Abigail.

Holcomb attended Middleton High School from 2004 until 2008, moving on to his beloved University of Florida to study nuclear engineering. During his time at the university, he greatly enjoyed attending many sporting events, especially with his fellow nuclear compatriots. He graduated a year early from the University of Florida with a B.S. in nuclear and radiological engineering, and moved on to the Georgia Institute of Technology to pursue his Ph.D. He earned his Master of Science in Nuclear Engineering in 2013, and moved to Knoxville, TN to continue his research at Oak Ridge National Laboratory

When he is not working on his research, Holcomb greatly enjoys hiking, playing video games, and lifting. He currently lives in Knoxville, Tennessee, where he hopes to continue to live and work for many years to come.